Acoustic and optical phonon scattering of the yellow 1S excitons in Cu_2O

A high resolution spectroscopy study

Dissertation

presented to the Faculty of Physics of the
Technische Universität Dortmund, Germany,
in partial fulfillment of the requirements
for the degree of

Doktor rer. nat.

technische universität
dortmund

presented by

Christian Sandfort

Dortmund, May 2010

Accepted by the Faculty of Physics of the
Technische Universität Dortmund, Germany.

Day of the oral exam: 11th June 2010

Examination board:

Prof. Dr. Manfred Bayer
Prof. Dr. Heinrich Stolz
Prof. Dr. Berhard Spaan
Dr. Bärbel Siegmann

Contents

1 Introduction

In 1925 A. Einstein predicted the manifestation of the wave nature of matter on a macroscopic scale [1], i.e. the macroscopic occupation of the ground state of a system, well know as Bose-Einstein condensation (BEC). The experimental realization, however, took about 70 years until the first condensates in dilute atomic vapors were realized [2, 3] in the the mid-'90s. Since then strong efforts were undertaken to demonstrate the phase transition to a condensate also in solid state systems and finally in recent years a few reports on Bose-Einstein condensation for several condensed matter quasi-particle excitations have been published, e.g. spin waves (magnons) in magnetic semiconductors [4], indirect excitons in coupled quantum wells [5] and mixed excitations of photon and exciton (polaritons) in semiconductor microcavities [6, 7].

In particular the latter system attracts a lot of attention since it promises the optical control of the condensate. Though very interesting results have been demonstrated, condensate-like phenomena in these systems are most likely driven externally and far from equilibrium [8] due to rather short carrier lifetimes of only a few ps. Moreover, highly sophisticated nanofabrication is required for these microcavities and the interparticle interaction is very strong compared to the weak interactions in atomic gases.

This work continues the study of the prototype systems of quasi-particle BEC, whose condensation has already been predicted in 1962 [9], excitons in a bulk semiconductor. Though excitons are made up of an electron and hole, both fermions bound by Coulomb interaction, they behave as bosons for moderate densities. For high densities, however, interparticle interaction leads to a loss of the bosonic character and the formation of a fully ionized electron-hole plasma [10].

The first excitons were discovered in cuprous oxide (Cu_2O) [11, 12, 13] and still, the lowest exciton transitions in Cu_2O most likely fulfill the requirements for a quasi-equilibrium excitonic BEC. These excitons are extremely stable complexes due to their large binding energy of 150 meV. This allows high particle densities without dissociation and formation of an electron-hole

plasma.

The lowest excitons of the so-called yellow series consist of the threefold orthoexciton, which is only quadrupole allowed, and the paraexciton, which is optically forbidden. The orthoexciton is split off from the paraexciton by 12 meV to higher energy due to isotropic electron-hole exchange and by high resolution spectroscopy it was shown that the orthoexciton is split up into three components by anisotropic electron-hole exchange [14, 15].

In most experiments concerning BEC in Cu_2O either non-resonant or resonant excitation of the orthoexcitons were studied [16, 17, 18]. The orthoexcitons decay on a ns-timescale to paraexcitons [19]. Due to the energy shift of 12 meV, this excitation scheme leads to hot paraexcitons, which have to cool down by exciton-exciton and/or acoustic phonon interaction to exhibit at high densities BEC with a macroscopic population at $k = 0$.

In contrast, direct excitation of the paraexciton by absorption at $k = k_0$ (photon wave number) yields ultra-cold excitons. Paraexciton absorption spectra can be measured by high resolution experiments in a magnetic field as was first shown in Ref. [20]. By high resolution spectroscopy in high quality samples at 10 T and 1.2 K an absorption coefficient of about 80 cm^{-1} with an extremely small linewidth of 80 neV for a bulk semiconductor was demonstrated. Due to the high resolution of the absorption measurements it was possible to measure directly a blue-shift and an increase of linewidth that point to an onset of repulsive interaction [21], a necessary prerequisite for a phase transition of the exciton gas to a condensate.

The studies presented in this work concentrate on a deeper understanding of the 1S excitons in Cu_2O, in particular on acoustic and optical phonon scattering processes within the 1S exciton sublevels. The thesis is divided in 7 chapters.

The following Chapter 2 introduces fundamental material and optical properties and supplies the reader with sufficient knowledge of the relevant interactions that is necessary to understand the experiments. The third chapter presents the optical setup and the advantages of high resolution spectroscopy. The following Chapters 4 to 6 deal with the experiments and their interpretation.

In Chapter 4 resonant optical phonon scattering to the 1S excitons is investigated. This is motivated by the fact that the spectral dependence of the phonon assisted luminescence can be interpreted as a replica of the exciton population. It is expected that a macroscopic occupation of the ground state at $k = 0$ would show up precisely in this luminescence.

In Chapter 5 the long lasting question about the exciton mass is solved by means of two-phonon excitation spectroscopy. Since for a weakly interacting Bose gas of excitons, the critical density n_c depends only on the product of

exciton mass M and critical temperature T_c, the exciton mass is the decisive parameter to calculate a BEC phase diagram. Furthermore two-phonon spectroscopy is also applied to the orthoexciton sublevels in order to investigate the k^2-dependent exchange parameters.

Chapter 6 focuses on stimulated Brillouin scattering by resonant excitation. Scattering processes are analyzed and the possibility to excite and stimulate orthoexcitons with arbitrary wave vector is demonstrated.

Finally, in Chapter 7 a summary of this study, implications and possible future projects are presented.

2 Basic considerations

In this chapter a short introduction of the material system Cu_2O is presented. It starts with a description of the crystal structure, followed by a discussion of acoustic and optical phonon modes, the band structure and the exciton series. Finally, the yellow 1S exciton series is examined in more detail with respect to various interactions.

2.1 Material properties

2.1.1 Crystal structure

Cuprous oxide (Cu_2O), which among mineralogist is also known as cuprite or as copper-I-oxide, is a translucent dark red to conchineal red semiconductor crystal. Naturally it is found, e.g. in Arizona or in Namibia. Cu_2O can also be grown artificially via the oxidation of copper [22], but much better quality is found in natural samples.

Cu_2O is a cubic crystal that crystallizes in the unusual cuprite structure and cleaves on (111) and more rarely on (001). The unit cell consists of four copper and two oxygen atoms with a lattice constant of $a_0 = 4.27$ Å [23]. The copper atoms form a fcc-lattice shifted by 1/4 of the body-diagonal of the bcc-lattice formed by the oxygen atoms as shown in Figure 2.1. Thus Cu_2O condenses in a simple cubic structure with a center of inversion around each copper atom and is described by the octahedral pointgroup O_h.

2.1.2 Acoustic and optical phonons in Cu_2O

Cu_2O has six atoms per unit cell and thus $3 \times 6 = 18$ phonon modes are found, three acoustic and 15 optical phonons. The sound velocities of the three acoustic phonons can be calculated with the help of classical elasticity theory assuming the wavelength λ to be long enough to ignore dispersion ($\lambda \gg a_0$). In the following the medium is modeled as continuous but anisotropic.

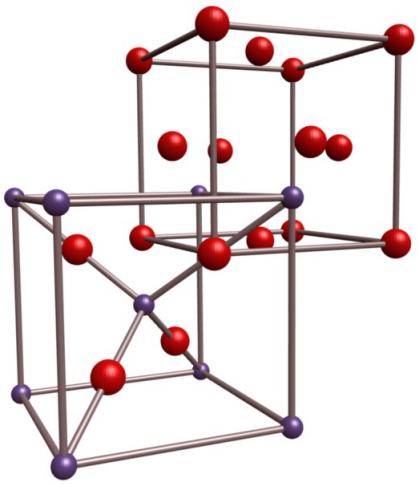

Figure 2.1: Crystal structure of Cu_2O. The small blue spheres represent oxygen atoms forming a bcc-lattice while the larger red spheres represent copper atoms forming an fcc-lattice.

The strain ε in a solid is defined in terms of spatial derivatives of the lattice atom displacement $\mathbf{u}(\mathbf{x})$ at position $\mathbf{x} = (x_1, x_2, x_3)$, and hence the change in the local displacement is given by

$$\delta u_l = \frac{\partial u_l}{\partial x_m} \delta x_m = \varepsilon_{lm} \delta x_m. \tag{2.1}$$

In a generalized statement of Hooke's Law the stress tensor σ is related to the strain tensor ε by a fourth rank elasticity tensor

$$\sigma_{ij} = c_{ijlm} \varepsilon_{lm}.$$

Not all elastic constants are independent and for cubic crystal symmetry, like Cu_2O, only three independent parameters define the nonzero elements of the elasticity tensor (Voigt contraction):

$$c_{iiii} = C_{11},\ c_{iijj} = C_{12},\ c_{ijij} = C_{44}.$$

The equation of motion for a small volume element of a crystal of mass density ρ is the wave equation

$$\rho \frac{\partial^2 u_i}{\partial t^2} = \frac{\partial \sigma_{ij}}{\partial x_j} = c_{ijlm} \frac{\partial^2 u_l}{\partial x_j \partial x_m}.$$

The plain wave solution $\mathbf{u} = u_0 \mathbf{p} e^{(\mathbf{q}\cdot\mathbf{x} - \omega t)}$ with the amplitude u_0, the polarization vector $\mathbf{p}$, the wave vector $\mathbf{q}$, and the angular frequency ω of the

acoustic wave leads to an eigenvalue equation

$$(c_{ijlm}q_jq_m - \rho\omega^2\delta_{il})p_l = 0. \tag{2.2}$$

By introducing the phase velocity $v = \omega/|\mathbf{q}|$ and the Christoffel tensor $D_{ij} = (1/\rho)c_{ijlm}n_jn_m$ with the wave normal $\mathbf{n} = \mathbf{q}/|\mathbf{q}|$ the eigenvalue equation 2.2 becomes

$$(D_{ij} - v^2\delta_{il})p_l = 0. \tag{2.3}$$

The phase velocity can be obtained by solving the characteristic equation of 2.3.

$$\det(D_{ij} - v^2\delta_{il}) = 0. \tag{2.4}$$

This cubic equation yields three solutions v_α, one corresponding to the longitudal sound velocities (v_{LA}) and two corresponding to the slow and the fast transversal sound velocities v_{STA}/v_{FTA}, which can be identified via the respective polarization vector obtained by solving equation 2.3 with the roots v_α from equation 2.4. One should note that not in all crystallographic directions the phonon polarization is purely longitudinal or purely transversal. For convenience, however, the phonons are labeled as LA, STA and FTA throughout this thesis.

In order to calculate the sound velocities in Cu_2O at low temperatures the room temperature measurements ($v_{LA} = 4.56 \cdot 10^3$ ms^{-1} from Ref. [24]) were used taking into account the temperature dependence of the elastic constants [25]. Additionally, small corrections arise due to the results of the Brillouin scattering experiments presented in Chapter 6. The solution of equation 2.4 for Cu_2O is shown in Figure 2.2 with $\rho = 6.09$ g/cm^3 [26] and the calculated low temperature elastic constants[1] $C_{11} = 123.5$ GPa, $C_{12} = 107.0$ GPa and $C_{44} = 12.9$ GPa. The blue solid line represents the LA sound velocity v_{LA}, the red dotted line the FTA v_{FTA} and the green dashed line the STA sound velocity v_{STA} for different crystallographic directions. Along [100] the LA sound velocity has its lowest value and rises till its maximum along [111]. In [110] direction STA and FTA phonons are degenerate, thus having the same sound velocity. Towards [110] the degeneracy for STA and FTA phonons is lifted. Finally, in [111] direction the TA phonons are degenerate again.

The 15 zone-center optical phonons have the following symmetry classification:

$$^1\Gamma_2^- \oplus {}^2\Gamma_3^- \oplus 2 \times {}^3\Gamma_4^- \oplus {}^3\Gamma_5^- \oplus {}^3\Gamma_5^+.$$

The $^1\Gamma_2^-$ and the double degenerate $^2\Gamma_3^-$ and the triply degenerate phonons are $^3\Gamma_5^-$ silent modes (in dipole approximation), the two sets of triply degen-

[1] The elastic constants for Cu_2O determined by room temperature neutron scattering can be found in Ref. [27].

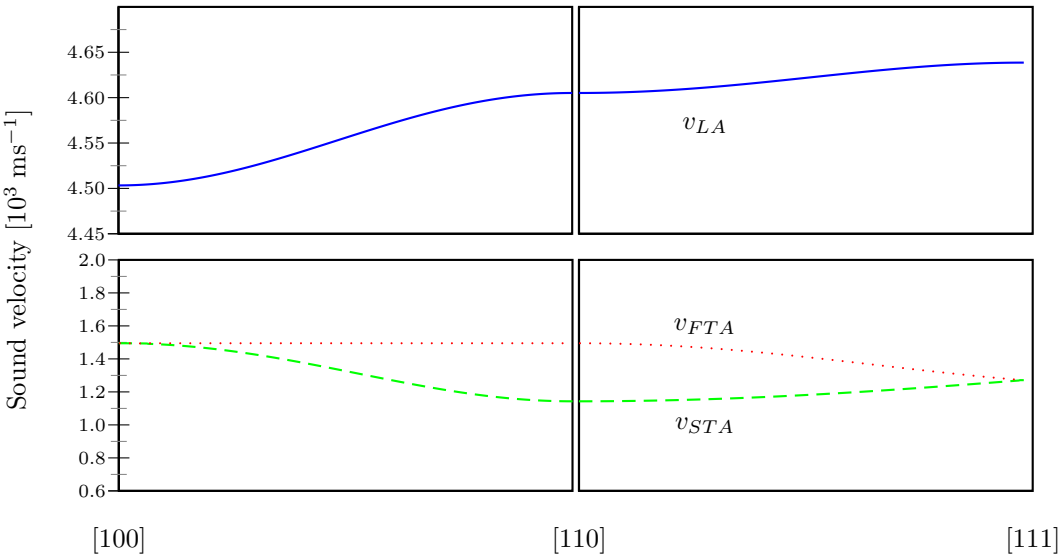

Figure 2.2: Sound velocities in Cu_2O as calculated by equation 2.4 in different crystallographic directions. The blue solid line represents the LA sound velocity v_{LA}, the red dotted line the FTA v_{FTA} and the green dashed line the STA sound velocity v_{STA}.

erate ${}^3\Gamma_4^-$ phonons are infrared active modes while the ${}^3\Gamma_5^+$ is a Raman-active mode.

2.1.3 Energy bands and exciton series

The conduction band of the direct band-gap semiconductor Cu_2O is formed by copper 4s-orbitals and separated by the gap energy $E_g = 2.173$ eV [28] from the upper valence band that is formed by copper 3d-orbitals [29]. Taking into account the electron spin, the lowest conduction band has ${}^2\Gamma_6^+$ symmetry while the highest valence bands are split into a ${}^2\Gamma_7^+$ and a ≈ 0.13 μeV lower ${}^4\Gamma_8^+$ band (spin-orbit interaction, Figure 2.3). The yellow 1S exciton series, studied in this thesis, is formed by a hole of the ${}^2\Gamma_7^+$ valence and an electron of the ${}^2\Gamma_6^+$ conduction band and named after the color of the light absorbed or emitted by its optical transition. The next higher one is the green series (${}^4\Gamma_8^+ \rightarrow {}^2\Gamma_6^+$, $E_{g,green} = 2.304$ [30]) followed by the blue (${}^2\Gamma_7^+ \rightarrow {}^4\Gamma_8^-$, $E_{g,blue} = 2.624$ [31] and the indigo (${}^4\Gamma_8^+ \rightarrow {}^4\Gamma_8^-$, $E_{g,indigo} = 2.755$ [31]) series. The symmetry represention of the excitons is given by the direct product of the representation of the conduction band Γ_C, the valence band Γ_V and the envelope function of the exciton Γ_{env}

$$\Gamma_{ex} = \Gamma_{env} \otimes \Gamma_V \otimes \Gamma_C. \qquad (2.5)$$

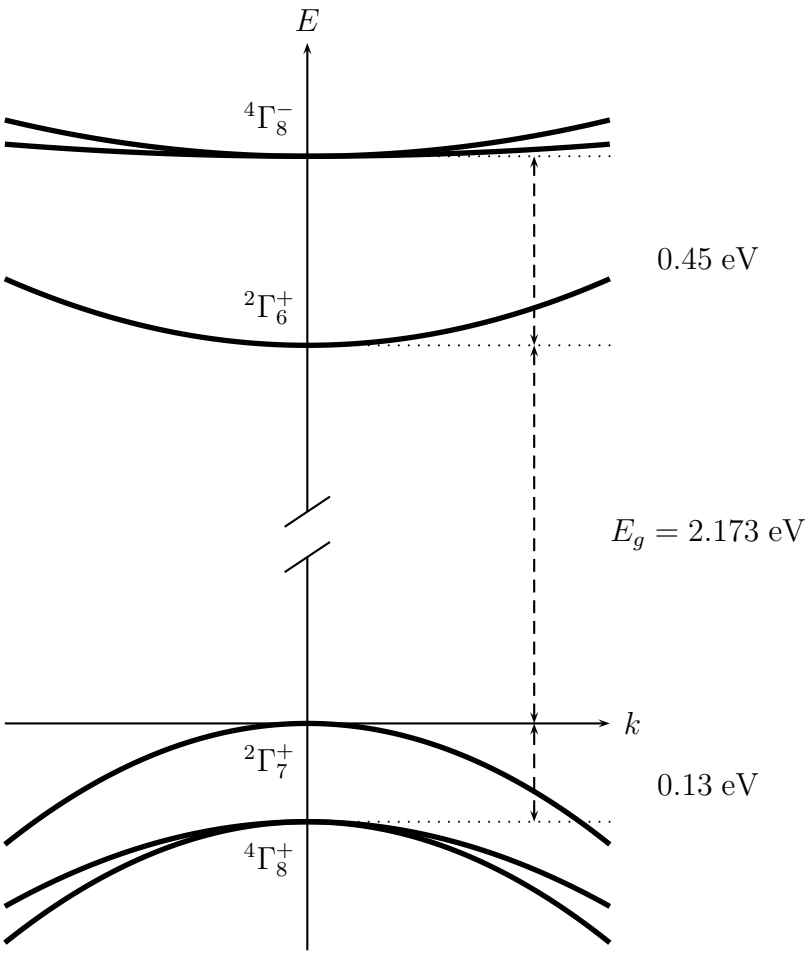

Figure 2.3: Band structure of Cu_2O near the Γ point.

The coupling of excitons to light can be understood by expanding the matrix element $\langle\beta|H_{Ex-R}|\alpha\rangle$ of the exciton-radiation coupling Hamiltonian H_{Ex-R}

$$\langle\beta|H_{Ex-R}|\alpha\rangle = A_0\langle\beta|\mathbf{e}\cdot\mathbf{p}|\alpha\rangle + iA_0\langle\beta|(\mathbf{k}\cdot\mathbf{r})\ (\mathbf{e}\cdot\mathbf{p})|\alpha\rangle + \ldots \qquad (2.6)$$

where A_0 is a constant amplitude, $\mathbf{k}$ the wave vector, $\mathbf{e}$ the polarization vector and $\mathbf{r}$ and $\mathbf{p}$ position and momentum of the exciton. The first term corresponds to a dipole transition and has $^3\Gamma_4^-$ symmetry. The following higher order term can be written in a symmetric form

$$(\mathbf{k}\cdot\mathbf{r})\ (\mathbf{e}\cdot\mathbf{p}) = \frac{1}{2}\mathbf{k}(\mathbf{k}\cdot\mathbf{p}+\mathbf{p}\cdot\mathbf{r})\mathbf{e} + \frac{1}{2}(\mathbf{k}\times\mathbf{e})\cdot(\mathbf{r}\times\mathbf{p}) \qquad (2.7)$$

that is the sum of the electric quadrupole with $^3\Gamma_5^+$ and $^2\Gamma_3^+$ symmetry plus the magnetic dipole moment of $^3\Gamma_4^+$ symmetry. Near the resonance of the

yellow 1S exciton, the appropriate term linear in $\mathbf{k}$ is a quadrupole transition of ${}^3\Gamma_5^+$ symmetry [32, 33].

Due to parity conservation, the first energetically lowest excitons that couple to light in dipole approximation are the yellow P-excitons via their ${}^3\Gamma_4^-$ component. It has been shown that these yellow excitons display a perfect hydrogenic series

$$E_n = E_g - R_{ex}/n^2, \qquad (n \geq 2), \tag{2.8}$$

where $R_{ex} = 97.43$ meV is the excitonic Rydberg constant, and n the principal quantum number [34, 35].

2.2 1S excitons of the yellow series

In case of the yellow 1S excitons the hydrogenic model is no longer applicable. This is caused by the fact that the exciton Bohr radius for the 1S excitons is extremely small $a_B = 0.8$ nm [36] and comparable to the lattice constant[2]. Hence, the excitons can not be described as weakly bound Mott-Wannier excitons anymore and approach the case of Frenkel excitons. Corrections arise due to the non-parabolicity of the bands since the extend of the exciton wave function is in the order of $1/a_B$. Furthermore, the localized 1S excitons are screened by the dielectric function at higher momenta and the effective Coulomb interaction is stronger than for higher excited exciton states. The above corrections are known as "central-cell corrections" [37] and lead to an increased binding energy of 150 meV [38] of the yellow 1S exciton, which is substantially larger than R_{ex}.

As the 1S excitons are formed from a double degenerate ${}^2\Gamma_6^+$ and a double degenerate ${}^2\Gamma_7^+$ band they decompose into a ${}^1\Gamma_2^+$ and a triply degenerate ${}^3\Gamma_5^+$ representations (compare equation 2.5 with $\Gamma_{env} = {}^1\Gamma_1^+$).

$${}^1\Gamma_1^+ \otimes {}^2\Gamma_6^+ \otimes {}^2\Gamma_7^+ = {}^1\Gamma_2^+ \oplus {}^3\Gamma_5^+.$$

The triply degenerate ${}^3\Gamma_5^+$ orthoexciton states have a total angular momentum of $J = 1$ and include pure spin singlet states, while the single ${}^1\Gamma_2^+$ paraexciton has total angular momentum $J = 0$ and consists only of pure spin triplet states. Short range electron-hole exchange interaction only effects pure spin singlet states and splits off the orthoexciton states from the paraexciton by $\epsilon = 12.12$ meV [39]. The paraexciton is optically forbidden, for an electric transition to all orders since $J = 0$, but the photon spin is 1.

[2] Since the exciton Bohr radius scales with the square of the principal quantum number, the effect is mostly important for $n = 1$.

Dipole excitation of the orthoexciton is also forbidden since it has even parity ($\langle {}^3\Gamma_5^+ | {}^3\Gamma_4^- | {}^1\Gamma_1^+ \rangle = 0$). However, in quadrupole approximation it becomes allowed ($\langle {}^3\Gamma_5^+ | {}^3\Gamma_5^- | {}^1\Gamma_1 \rangle \neq 0$).

In contrast to the dipole operator, the quadrupole operator depends on the wave vector $\mathbf{k}$ relative to the lattice and the light polarization vector $\mathbf{e}$. The amplitude of the quadrupole transition $\mathbf{A}_\mathrm{Q}$ in the basis of the Cartesian representation of the three orthoexciton states Γ_{5yz}^+, Γ_{5zx}^+ and Γ_{5xy}^+ can be calculated with the symmetric vector product of $\mathbf{k}$ and $\mathbf{e}$:

$$\mathbf{A}_\mathrm{Q} = \frac{1}{|\mathbf{k}|} \begin{pmatrix} e_y k_z + e_z k_y \\ e_z k_x + e_x k_z \\ e_x k_y + e_y k_x \end{pmatrix}. \tag{2.9}$$

Hence the relative oscillator strength of a given orthoexciton state $\mathbf{\Psi}_\mathrm{O}^{(i)}(\mathbf{B}, \mathbf{k})$ with $i = 1, 2, 3$ is given by

$$f_r^{(i)}(\mathbf{B}, \mathbf{k}) = \mathbf{A}_\mathrm{Q} \cdot \mathbf{\Psi}_\mathrm{O}^{(i)}(\mathbf{B}, \mathbf{k}) \tag{2.10}$$

where $\mathbf{\Psi}_\mathrm{O}^{(i)}$ can depend on a magnetic field $\mathbf{B}$ and $\mathbf{k}$ as it is shown below. The absolute oscillator strength of the orthoexciton is rather small $f_O = 3.7 \cdot 10^{-9}$ [40] compared, for example, to the dipole transition of the 2P exciton ($f_P = 3 \times 10^{-6}$) [28].

2.2.1 Exciton-photon interaction

Though the exciton-photon coupling is only weak, the orthoexciton dispersion exhibits a characteristic polariton structure with an upper and a lower polariton branch that represents mixed modes of photon and exciton [41]. The polariton character of the orthoexciton is directly seen by quantum beat spectroscopy [41, 42]. This was shown for the paraexciton as well [43, 44].

The repulsion of the exciton and the photon state at the intersection (k_0, E_0) of the exciton dispersion

$$E_x(k) = E_x(0) + \frac{\hbar^2 k^2}{2M_x}, \tag{2.11}$$

where $M_x = m_x m_0$ is the exciton mass (m_0 is the bare electron mass), and photon dispersion

$$E_\gamma(k) = \frac{\hbar c k}{\sqrt{\varepsilon_b}} \tag{2.12}$$

with the speed of light c and the background dielectric constant $\varepsilon_b = 8.76$ leads to the polariton dispersion

$$\frac{E_\gamma(k)}{E^2} = 1 + \frac{\Omega_R^2(\mathbf{k}, \mathbf{e})}{E_x(k)^2 - E^2}. \tag{2.13}$$

The Rabi energy is given by

$$\Omega_R(\mathbf{k},\mathbf{e}) = \sqrt{f(\mathbf{k},\mathbf{e})}E_\gamma(k). \tag{2.14}$$

Solving equation 2.13 for E yields two solutions, the upper polariton branch E_{UP} and the lower polariton branch E_{LP} as shown in Figure 2.4 around the orthoexciton resonance (k_0, E_0). The upper polariton branch

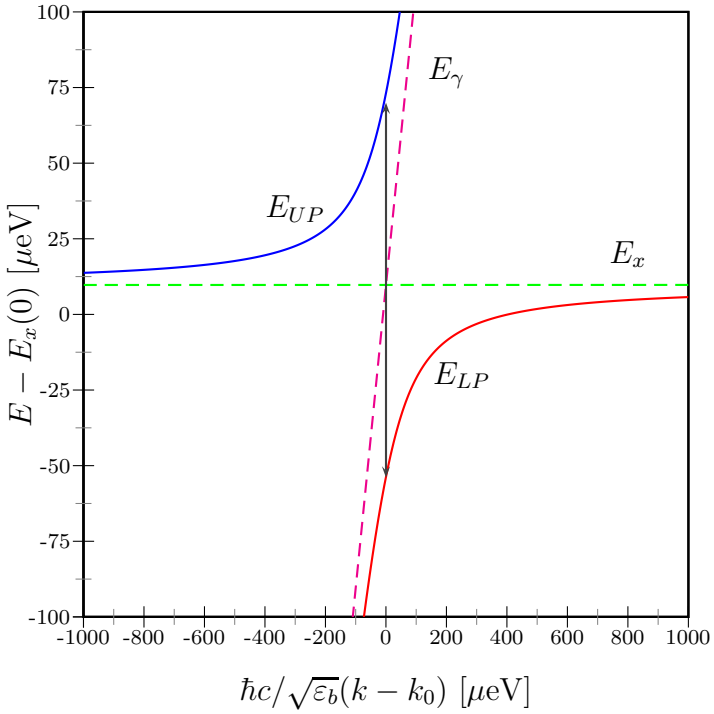

Figure 2.4: Orthoexciton polariton dispersion around the resonance (k_0, E_0): upper blue curve, upper polariton branch E_{UP}; lower red curve, lower polariton branch E_{LP}, magenta dashed line, uncoupled light dispersion; green dashed line, uncoupled exciton dispersion; arrow marks Rabi energy $\Omega_R = 124$ μeV at the orthoexciton resonance (k_0, E_0).

E_{UP} starts at $E = E_x(0)$ for $k \to 0$. For $E \to \infty$ the upper polariton branch E_{UP} approaches asymptotically the light line E_γ. In contrast, the lower polariton branch approaches asymptotically E_γ for $E \to -E_x(0)$ and follows the exciton dispersion E_{ex} for $k \to \infty$. Since the polariton is a superposition of photon and exciton, it can be decomposed into a photon and an exciton contribution depending on k and E. The photon contribution increases and the exciton contribution decreases while the states approach the light line ($E_{LP} \to -E_x(0)$ and $E_{UP} - > \infty$) until they are completely photon like. On

the other hand, the photon contribution decreases while the exciton contribution increases ($k \to 0$ and $k \to \infty$) until they are completely excitonic. At the resonance k_0 both polariton states on the upper and lower polariton branch are 50% photon and 50% exciton like. The energetic splitting of the two states reaches its minimum at the resonance wave vector k_0 and corresponds to the Rabi energy $\Omega_R = E_{UP}(k_0) - E_{LP}(k_0)$ (black arrow), which scales with the square root of the oscillator strength f (equation 2.14). The extremely small Rabi energy of $\Omega_R = 124$ μeV leads to a weak radiative broadening of the 1S excitons and in high quality samples with low impurity concentrations a very narrow absorption can be expected. (compare section 2.2.4).

2.2.2 Exciton-acoustic phonon interaction

The lattice distortion by acoustic phonons introduces potential energy changes that can cause interconversion between ortho- and paraexcitons as well as transitions between orthoexciton sublevels. The strain induced by the acoustic phonon can be expressed in terms of irreducible representations of the octahedral group and classified into uniform compression ($^1\Gamma_1^+$), pure rotation ($^3\Gamma_4^+$), and shear strain ($^2\Gamma_3^+$ and $^3\Gamma_5^+$).

These symmetries can be identified in the decomposition of equation 2.1 into a symmetric and an antisymmetric part:

$$\delta u_l = \frac{1}{2}\left(\frac{\partial u_l}{\partial x_m} + \frac{\partial u_m}{\partial x_l}\right)\delta x_m - \frac{1}{2}\left(\frac{\partial u_m}{\partial x_l} - \frac{\partial u_l}{\partial x_m}\right)\delta x_m$$

$$\Rightarrow \delta u_l = \epsilon_{lm}\delta x_m - w_{lm}\delta x_m. \qquad (2.15)$$

The symmetric part ϵ_{lm} of equation 2.15, is associated with deformation of the crystal by compression and shear strain. In Cu_2O uniform compression causes an increase of the band gap while shear strain removes the degeneracy of the top of the valence band states. With the hydrostatic and shear deformation

potentials Ξ_0, Ξ_{xx}, Ξ_{xy} the strain Hamiltonions has the form [45]

$$H_1 = \Xi_0 \begin{pmatrix} \epsilon_{xx}+\epsilon_{yy}+\epsilon_{zz} & 0 & 0 \\ 0 & \epsilon_{xx}+\epsilon_{yy}+\epsilon_{zz} & 0 \\ 0 & 0 & \epsilon_{xx}+\epsilon_{yy}+\epsilon_{zz} \end{pmatrix}, \quad (2.16)$$

$$H_3 = \Xi_{zz} \begin{pmatrix} 2\epsilon_{xx}-\epsilon_{yy}-\epsilon_{zz} & 0 & 0 \\ 0 & 2\epsilon_{yy}-\epsilon_{yy}-\epsilon_{zz} & 0 \\ 0 & 0 & 2\epsilon_{zz}+\epsilon_{xx}+\epsilon_{yy} \end{pmatrix}, \quad (2.17)$$

$$H_5 = \Xi_{xy} \begin{pmatrix} 0 & \sqrt{3}\epsilon_{xy} & \sqrt{3}\epsilon_{xz} \\ \sqrt{3}\epsilon_{yx} & 0 & \sqrt{3}\epsilon_{yz} \\ \sqrt{3}\epsilon_{zx} & \sqrt{3}\epsilon_{zy} & 0 \end{pmatrix}, \quad (2.18)$$

in the basis of the Cartesian representation of the three orthoexciton states Γ^+_{5yz}, Γ^+_{5zx} and Γ^+_{5xy}. The paraexciton is only affected by the hydrostatic strain H_1 since it is composed in equal parts of yz, xz and xy holes. The experimentally measured deformation potentials are given by $\Xi_0 = -1.68$ eV, $\Xi_{zz} = -0.29$ eV and $\Xi_{xy} = 0.18$ eV [46, 47, 48].

The antisymmetric part w_{lm} of equation 2.15 contains the axial vector

$$w_{lm} = \frac{1}{2}(\nabla \times \mathbf{u})|_{lm}, \quad (2.19)$$

which is associated with pure rotation ($^3\Gamma^+_4$). Hence, it is not a deformation and cannot change any energy level. However, it can change the orbital momentum $\mathbf{L}$ leading to a spin-orbit Hamiltonian of the form

$$H_4 = \frac{\alpha}{3}(\nabla \times \mathbf{u}) \times \mathbf{L} \cdot \mathbf{S}^h = \frac{\alpha}{3}(\mathbf{L} \times \mathbf{S}^h) \cdot (\nabla \times \mathbf{u}), \quad (2.20)$$

where $\alpha = 131$ meV is the spin-orbit splitting energy and $\mathbf{S}^h$ the angular momentum operator of the hole spins [49].

To sum up the above, the uniform compression ($^1\Gamma^+_1$) is a dominant scattering channel (mobility, diffusion, and thermalization) whereas shear strain ($^2\Gamma^+_3$, $^3\Gamma^+_5$) mediates interconversion processes between orthoexciton sublevels [50]. However, all of the above mentioned deformations can not participate in any spin-flip process. Pure rotations, however, can flip the spin and were identified as the ortho-para down-conversion mechanism [49].

It should be noted that external strain, originating from the sample mounting, or intrinsic strain due to imperfections of the lattice structure, cutting and polishing during the sample preparation, or thermal stress can

be described by the same interaction matrices. It has been shown, that intrinsic strain is of the same order of magnitude as k^2-dependend exchange interaction [51, 15] that is discussed in the following section.

2.2.3 $\mathbf{k^2}$-dependent exchange interaction

In section 2.2 it has already been mentioned that wave vector independent exchange interaction splits off the orthoexciton from the paraexciton. High resolution spectroscopy experiments, however, show that the orthoexciton exhibits a wave vector dependent fine structure. This fine structure can be explained by taking into account higher order terms of the electron hole exchange interaction up to the order of k^2 [14, 15].

Due to the inversion symmetry of the lattice, terms linear in k vanish in the expansion of the exchange interaction. To the order of k^2 the short range exchange Hamiltonian of ${}^1\Gamma_1^+$ symmetry is proportional to the product of the electron and hole spin operators $({}^3\Gamma_4^+ \otimes {}^3\Gamma_4^+)$ and $\mathbf{k}\cdot\mathbf{k}$ $({}^3\Gamma_4^- \otimes {}^3\Gamma_4^-)$ and therefore decomposes into ${}^1\Gamma_1^+ \oplus {}^2\Gamma_3^+ \oplus {}^3\Gamma_4^+ \oplus {}^3\Gamma_5^+$ invariant representations. Algebraic calculation of the matrix elements yields three interaction matrices for the short range exchange in the basis of the Cartesian representation of the three orthoexciton states Γ_{5yz}^+, Γ_{5zx}^+ and Γ_{5xy}^+ while the ${}^3\Gamma_4^+$ electron hole exchange vanishes:

$$J_1 = \Delta_1 k^2 \cdot \mathbf{1}, \tag{2.21}$$

$$J_3 = \Delta_3 \begin{pmatrix} 3k_x^2 - k^2 & 0 & 0 \\ 0 & 3k_y^2 - k^2 & 0 \\ 0 & 0 & 3k_z^2 - k^2 \end{pmatrix}, \tag{2.22}$$

$$J_5 = \Delta_5 \cdot \begin{pmatrix} 0 & k_x k_y & k_y k_z \\ k_x k_y & 0 & k_y k_z \\ k_x k_z & k_y k_z & 0 \end{pmatrix} \tag{2.23}$$

with the exchange parameters Δ_1, Δ_3, Δ_5. Since J_1 scales with k^2, it alters the isotropic effective mass of the orthoexcitons.

The matrix representation of the long range exchange is given by

$$J_{ex}^Q = \Delta_Q \cdot \frac{1}{k^2} \begin{pmatrix} k_z^2 k_y^2 & k_z^2 k_x k_y & k_y^2 k_z k_x \\ k_z^2 k_x k_y & k_z^2 k_x^2 & k_x^2 k_y k_z \\ k_y^2 k_z k_x & k_x^2 k_y k_z & k_x^2 k_y^2 \end{pmatrix}. \tag{2.24}$$

with the constant long range quadrupole-quadrupole exchange parameter Δ_Q.

Apparently, the k^2 dependent exchange interaction lifts the degeneracy of the orthoexcitons and the new eigenstates are linear combinations of the three orthoexciton states of Γ^+_{5yz}, Γ^+_{5zx} and Γ^+_{5xy} symmetry.

The exchange parameters $\Delta_3 = -1.3$ μeV, $\Delta_5 = 2$ μeV and $\Delta_Q = 5$ μeV were determined by measuring the energies of the three orthoexciton states in absorption in dependence of the **k**-direction of the exciting laser relative to the crystal lattice [14, 15]. By this method, however, Δ_1 could not be determined since J_1 is independent of the **k**-direction.

2.2.4 Zeeman splitting

The degeneracy of the orthoexcitons can also be lifted by perturbation such as strain [47, 52, 53] or a magnetic field [54]. These perturbations do not only lift the degeneracy, but also mix the paraexciton with the orthoexcitons and thus, quadrupole oscillator strength is transfered from the orthoexcitons to the paraexciton.

The experiments presented in this thesis, make use of a magnetic field to optically excite and detect the paraexciton. The magnetic field interaction of the paraexciton and the three orthoexciton states can be expressed by the following matrix in the basis of the ${}^1\Gamma^+_2$ paraexciton and the Γ^+_{5x}, Γ^+_{5y} and Γ^+_{5z} orthoexciton states:

$$H_B = \begin{pmatrix} -\varepsilon & i\alpha B_x & i\alpha B_y & i\alpha B_z \\ -i\alpha B_x & 0 & -i\beta B_z & i\beta B_y \\ -i\alpha B_y & i\beta B_z & 0 & -i\beta B_x \\ -i\alpha B_z & -i\beta B_y & i\beta B_x & 0 \end{pmatrix}. \qquad (2.25)$$

Here B_x, B_y and B_z denote the Cartesian components of the magnetic field and ε represents the k independent short range exchange interaction. The magnetic field dependent coupling of para- and orthoexciton is described by the Zeeman parameter $\alpha = 92.5$ μeV/T while the interaction of the orthoexciton components is described by the Zeeman parameter $\beta = 47.7$ μeV/T [55]. Diagonalization of the above matrix for the three orthoexciton states yields three new eigenstates, which are denoted as M$\pm$1 and M=0.

The ${}^1\Gamma^+_2$ paraexciton state mixes only with the M=0 component of the orthoexciton. The admixture can be described by the field induced admixture coefficient [21]

$$a_O = \frac{\alpha B}{\sqrt{(\alpha B)^2 + \varepsilon^2}} \approx \frac{\alpha B}{\varepsilon}. \qquad (2.26)$$

Due to this admixture the paraexciton gains oscillator strength from the quadrupole allowed orthoexciton:

$$f_P = \left(\frac{\alpha B}{\epsilon}\right)^2 f_O = 5.8 \cdot 10^{-5}/\mathrm{T}\, f_O\, B^2, \qquad (2.27)$$

where f_P is the paraexciton and f_O the oscillator strength of the orthoexciton. Equation 2.27 shows that even at $B = 10$ T, the paraexciton oscillator strength is only 6 ‰ of the orthoexciton oscillator strength.

3
Experimental technique

A resolution of several μeV is usually sufficient for spectroscopy of excitons since lines are homogeneously and inhomogeneously broadened. In the case of Cu_2O, however, high resolution spectroscopy opened up new aspects. This method e.g. allowed the investigation of the k^2-dependent exchange interaction [14] or revealed in high purity samples paraexciton resonances with spectral widths of 80 neV [21]. In this chapter the main aspects of a high resolution setup are presented, followed by an overview of the samples used and their properties.

3.1 Experimental setup

The crucial element of the setup is the single frequency dye laser (*Coherent 899-29*). The dye (*Rhodamin 6G*) is pumped by a 10 W frequency doubled Nd:YVO_4 laser (*Coherent Verdi V-10*) at $\lambda_{pump} = 532$ nm. The emission wavelength of the laser (550 to 630 nm with *Rhodamin 6G*) is roughly selected by means of a birefringent filter. The bandwidth of the emission is lowered down to about 40 neV by an intra-cavity etalon assembly. A fraction of the beam is coupled into an external reference cavity, connected to an electronic servo loop, which stabilizes the emission bandwidth down to 5 neV. The frequency control allows to scan the laser over a frequency range of 30 MHz and to change the frequency in steps of 10 MHz $\approx$ 41 neV.

About 10% of the laser light is coupled into a 300 MHz scanning Fabry-Perot spectrum analyzer (*Coherent Model 216*, FP) and a fiber into a wavemeter with an absolute accuracy of 30 MHz (*HighFinesse WSU-30*, FC). Spectrum analyzer, wavemeter and a beam profile analyzer (*Vision 1024 digital imaging camera Laser 2000*, BA) form a diagnostic setup that ensures stable excitation at the resonance wave vector $k = k_0$ of ortho- or paraexciton with a TEM_{00} Gaussian mode. While the spectrum analyzer with a finesse of more than 200 (line width less than 1.5 MHz) allows to align the laser

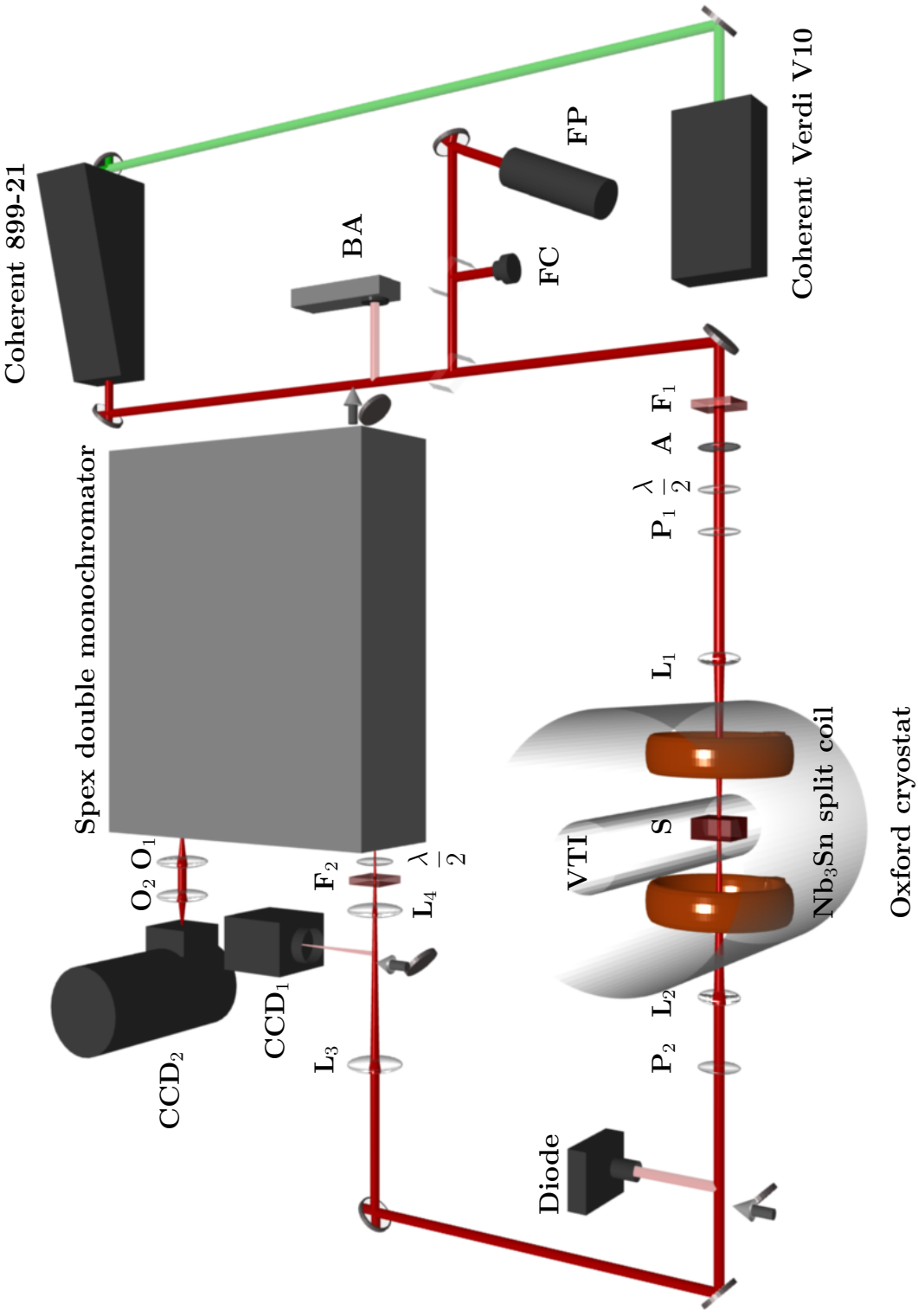
Coherent 899-21
Coherent Verdi V10
BA
FC
FP
Spex double monochromator
O_2 O_1
F_2
L_4 $\frac{\lambda}{2}$
CCD_2
CCD_1
L_3
P_1 $\frac{\lambda}{2}$ A F_1
L_1
VTI
S
Nb_3Sn split coil
Oxford cryostat
P_2 L_2
Diode

for best wave length stability, any jump in laser wavelength is immediately recognized by the wavemeter (resolution 30 MHz), which is extremely useful in excitation spectroscopy measurements.

The light beam passes a bandpass filter (F_1) to suppress amplified spontaneous emission (ASE) from the laser and an attenuation filter (A) to set the desired excitation intensity. Suppression of ASE is crucial since in the spectral region of the measured phonon-assisted luminescence the intensity of the observed luminescence is in the same order of magnitude as the intensity of the ASE. The appropriate excitation polarization is set via a half wave plate ($\frac{\lambda}{2}$) and a polarizer (P_1). The laser beam is focused by the lens L_1 (19 cm) to a spot of 30 μm on the sample (S).

The samples are immersed in liquid ^{4}He inside a variable temperature insert (VTI) of a split coil cryostat (*Oxford Spectromag*). All measurements presented in this thesis were performed in superfluid Helium at about 1.5 K. The low temperature is achieved by pumping on the VTI with an oil-pump (50 m^3/h) and a Roots pump (150 m^3/h). The temperature is monitored with a *Cernox* sensor mounted on the sample holder.

The split-pair superconducting coils of the cryostat are made out of Ni_3Sn and allow magnetic fields up to 11 T in Faraday $\mathbf{k} \parallel \mathbf{B}$ and Voigt $\mathbf{k} \perp \mathbf{B}$ configuration.

The emission or the transmitted beam is collimated by the lens L_2 (19 cm). With a movable mirror the light can be directed on a photodiode (*New Focus 2031*) for transmission/absorption measurements. The photodiode is connected to an 1.5 GHz oscilloscope (*LeCroy 9362*). By scanning the laser through the exciton resonance the transmission was always monitored *prior* to the luminescence measurement for two reasons: i) selection of a strain-free part of the sample with narrow resonance; ii) tuning into resonance for maximum absorption.

By the lens L_4 the emitted light is focused on the entrance slit of a double monochromator (*Spex*) with a focal length of 0.85 m or on a camera (*SVX-H9*, pixel size 6 μm, CCD_1). The camera allows to take spatially resolved images of the sample. In order to illuminate the sample a diverging lens is put temporarily in front of the cryostat.

The ratio of the selected focal lengths of L_2 and L_3 leads to two times enlarged images of the sample on the entrance slit of the double monochromator. A cylindrical lens (L_4) in front of the entrance slit corrects for the astigmatism of the monochromator. An half wave plate ($\frac{\lambda}{2}$) in front of the entrance slit allows to rotate the polarized luminescence into the preferred

polarization plane of the monochromator[1]. A low frequency pass filter (F_2) is used to suppress scattered laser light.

The gratings used in the Cerny-Turner type monochromator have a size of 110 mm × 110 mm and a grating constant of $g = 1200/mm$. To increase the resolution and because of the a grating blaze wavelength of 1 μm the monochromator is operated in second order. The theoretical resolution $E/\Delta E$ of the monochromator is calculated from the product of the number of grating lines times the operation order. Therefore at $E = 2$ eV one obtains $\Delta E = 3.8$ μeV.

Two objectives (O_1, O_2) behind the exit slit of the monochromator yield a four times magnified image of the plane of the exit slit on the nitrogen cooled camera (*Roper Scientific*, pixel size 25 μm, CCD_2). With an entance slit width of 40 μm a resolution of about 10 μeV in second order was achieved.

3.2 Samples

All samples used in this thesis were cut from one natural piece of Cu_2O from the Tsumeb mine in Namibia, which is renowned for a wealth of rare and unusual minerals. It had turned out that natural crystals of Cu_2O are clearly superior compared to artificial ones. With the aid of X-ray orientation the samples were cut along major crystaline axes and the surfaces were polished. All samples used are mounted strain free in specially designed holders. In these holders the samples are surrounded by a spacer and sandwiched between two brass plates. The spacers are a little bigger than the samples and allow the samples to move slightly.

The orientations and the thicknesses of the four samples examined in this thesis are listed in Tab. 3.1. For a mounted crystal holder e_z is always

Sample	e_z	e_x	e_y	$w[\,\mu\mathrm{m}]$
H12	$[1\bar{1}0]$	[001]	[110]	514
H13	$[1\bar{1}0]$	[001]	[110]	252
H15	[111]	$[1\bar{1}0]$	$[11\bar{2}]$	474
H35	[001]	[110]	$[1\bar{1}0]$	502

Table 3.1: Samples used: e_z, e_x, e_y, orientation; w, thickness.

perpendicular to the sample and along **k** of the incoming laser light. In

[1]Horizontal linear polarization yield a factor of 8 more transmission through the double monochromator than vertical linear polarization

Faraday and Voigt configuration the magnetic field is oriented along e_z and e_x, respectively.

In order to characterize the samples spatially resolved images of the crystal can be taken with the camera CCD_1. Fig. 3.1 shows such images of the H12 sample in a magnetic field of 10 T for different excitation energies around the paraexciton resonance. From one image to the another the laser energy is increased from 2.0205958 eV to 2.0205974 eV in steps of 10 MHz (41 neV). The absorption of the paraexciton moves from the lower right corner to the upper left corner. Apparently, already in this small energy reange of only 1.64 μeV the paraexciton absorption depends strongly on the excitation position on the sample. It is therefore important to find a uniform spot on the sample and a compulsory task prior to each measurement.

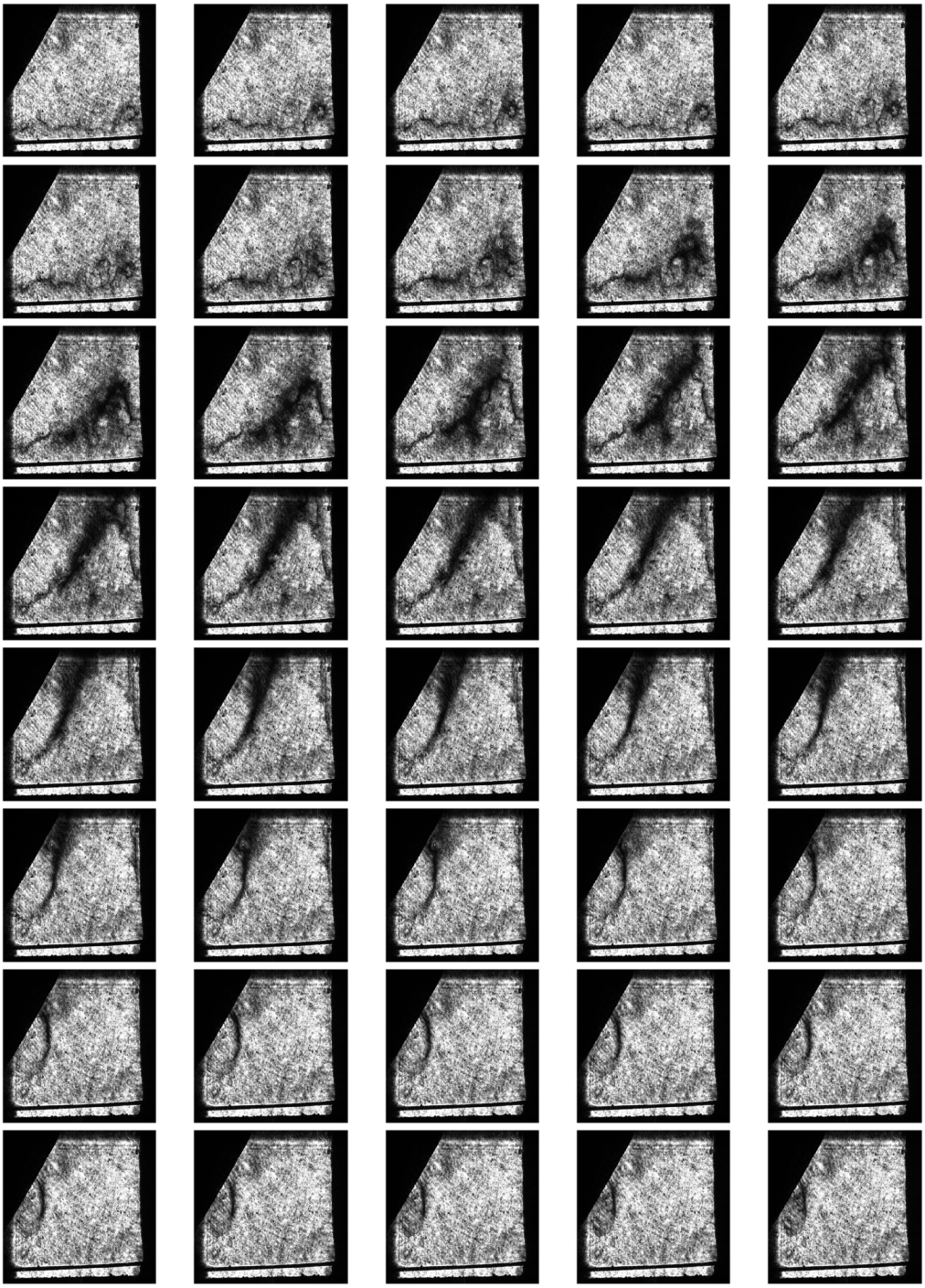

Figure 3.1: Spatially resolved transmission images of the H12 sample in a magnetic field of $B = 10$ T while tuning the laser energy through the paraexciton resonance from 2.0205958 eV to 2.0205974 eV in steps of 10 MHz (41 neV).

4

Resonant optical phonon scattering

Resonant optical phonon (LO and TO) scattering from orthoexcitons in Cu_2O was extensively studied in the past [56, 57]. Acoustic and optical phonon scattering in high magnetic fields were reported [55]. It was shown that longitudinal acoustic (LA) as well as transverse acoustic (TA) phonon scattering have to be considered to analyze the rich spectrum of inter- and intraband processes. Recently, LO phonon scattering to the paraexciton in very high magnetic fields up to 32 T was observed [58].

These LO phonon scattering processes are of special interest because the almost dispersionless optical phonons allow to study the thermal distribution directly in the search for Bose-Einstein condensation (BEC) of excitons [16]. A macroscopic occupation of the ground state $k = 0$ of the excitons is anticipated to manifest as a peak at lowest energies of the thermal distribution. Furthermore, temperature and chemical potential can be deduced from the phonon assisted luminescence.

Since the paraexciton, as the most promising candidate for Bose-Einstein condensation of excitons, is optically forbidden to all orders, it was, up to now, populated through relaxation from higher lying states. Hence, only non-resonant optical phonon scattering of the paraexcitons has been observed. In this chapter it will be demonstrated that direct resonant optical injection of ultra-cold excitons can be obtained through a magnetic field induced symmetry breaking. Due to this symmetry breaking not only the ${}^3\Gamma_5^-$ phonon but also other optical phonons (${}^1\Gamma_2^-$, ${}^2\Gamma_3^-$, $2 \times {}^3\Gamma_4^-$) become allowed. The experiments presented in this chapter show phonon assisted luminescence to the paraexciton from all these phonons with pronounced Raman resonances for the first time. In connection with the observation of BEC of paraexcitons there is hope that the high resolution setup allows to distinguish between resonant Raman scattering from $k = k_0$ and a macroscopic occupation due to a BEC at $k = 0$.

4.1 Scattering mechanism

Raman scattering denotes inelastic scattering of a photon and an optical phonon. The energy of the scattered photon $\hbar\omega_{out}$ differs from the energy of the incident photon $\hbar\omega_{in}$ by the energy of the involved optical phonon $\hbar\omega_{Ph}$. In case of an absorption of a phonon, the process is called anti-Stokes scattering ($\hbar\omega_{out} = \hbar\omega_{in} + \hbar\omega_{Ph}$), while Stokes scattering is considered as emission of a phonon ($\hbar\omega_{out} = \hbar\omega_{in} - \hbar\omega_{Ph}$). When the energy of the ingoing ($\hbar\omega_{in}$) or of the outgoing photon ($\hbar\omega_{out}$) is resonant with an electronic transition the scattering cross section is expected to be enhanced and the phenomenon is called resonant Raman scattering. In case of an ingoing resonance the width of the Raman cross section is expected to be proportional to the width of the electronic state γ_X for $\gamma_X < \omega_{in}$. For an outgoing resonance the Raman cross section should reflect the phonon width γ_{Ph} *and* the width of the electronic state γ_X [59].

Figure 4.1 illustrates the mechanism of ingoing resonant optical phonon scattering in case of the paraexciton and a ${}^3\Gamma_5^-$ phonon. Resonant excitation at k_0 creates ultra-cold paraexcitons with the kinetic energy $E_0 = 13.2\ \mu$eV above the band minimum which corresponds in thermal equilibrium to a temperature of 0.15 K. Stokes scattering from (k_0,E_0) with an optical phonon leads to a pronounced Raman peak in the phonon assisted luminescence (red curve on the right hand side in Figure 4.1) one phonon energy (10.58 meV for the ${}^3\Gamma_5^-$ phonon) below the excitation energy.

Unlike quadrupole emission, which is only allowed at the intersection of the light line and the exciton dispersion at k_0, optical phonon scattering is allowed from any k. As the dispersion of the ${}^1\Gamma_2^-$, ${}^2\Gamma_3^-$, ${}^3\Gamma_5^-$ optical phonons and the longitudinal component of the ${}^3\Gamma_4^-$ phonon can be neglected close to the zone center, the optical phonon luminescence exhibits directly the thermal distribution of paraexcitons $N_P(E)$. For the transversal components of the dipole allowed ${}^3\Gamma_4^-$ phonon, however, the dispersion (phonon polariton branches) has to be taken into account. In the simplest case of thermal equilibrium at low temperatures $N_P(E)$ should reflect a Bose distribution

$$N_P(E) \propto \frac{\sqrt{E}}{e^{(E_{\mathbf{p}}-\mu)/k_bT} - 1} \tag{4.1}$$

with the chemical potential μ, the exciton temperature T and the Boltzmann constant k_b. Both Raman peak and Bose distribution are shown exemplarily in red in Figure 4.1.

Due to their symmetry the phonons involved in the scattering process obey distinct polarization selection rules. As it has been shown in section

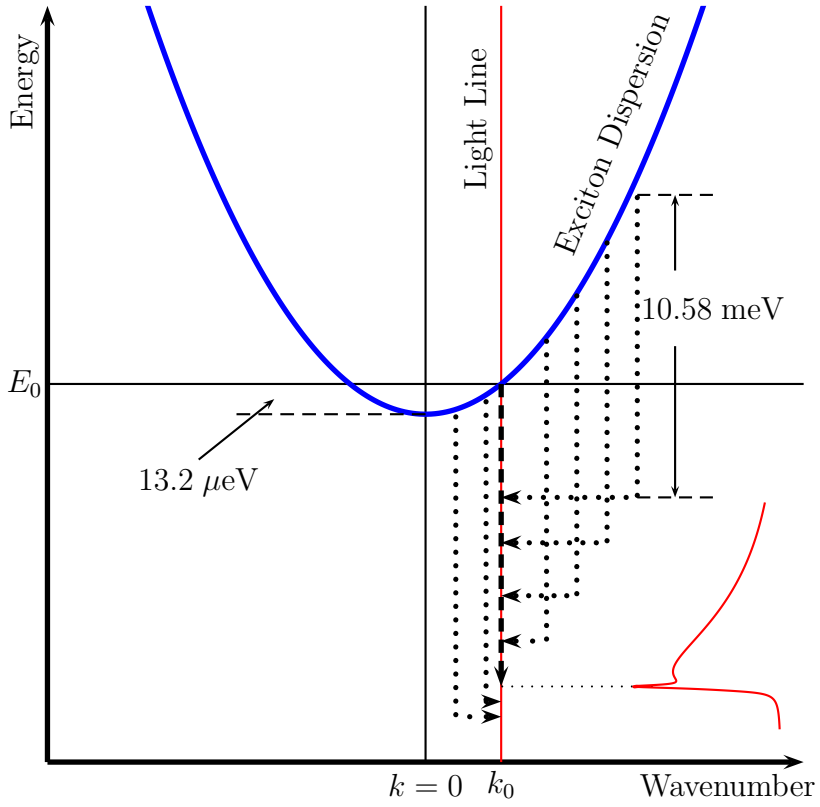

Figure 4.1: Scheme of resonant optical phonon scattering. Blue parabola, exciton dispersion; red solid line, light line; dotted arrows, optical phonon scatterin process; red curve, exciton population replica.

2.2.3, the k^2-dependent exchange interaction leads to a splitting of the threefold degenerate orthoexciton. In high magnetic fields, however, the perturbation due to this interaction can be neglected since it is only 5 μeV compared to the splitting $\Delta E_{\pm 1} = 954$ μeV of M=$\pm$1 at 10 T. The diagonalization of the matrix (equation 2.25) yields the new eigenstates $\mathbf{\Psi}(\mathbf{B})$.

For a given polarization $\mathbf{e}$ of the light $\hbar\omega_{out}$ the relative intensity $\chi^{(j)}$ for optical phonon emission is given by:

$$\chi^{(j)} = \sum_{i=1}^{g_j} |\mathbf{e}^{\mathrm{T}}\, \hat{\sigma}_i^{(j)}\, \mathbf{\Psi}(\mathbf{B})|^2. \qquad (4.2)$$

g_j denotes the degeneracy of the optical phonon j ($j = 2, 3, 4, 5$) and $\hat{\sigma}_i^{(j)}$ the coupling matrix of the phonon. The component of the paraexciton wave function $\mathbf{\Psi}(\mathbf{B})$ with ${}^1\Gamma_2^+$ symmetry can only couple to a ${}^3\Gamma_5^-$ phonon, whereas the orthoexciton admixture of ${}^3\Gamma_5^+$ symmetry (M=0 component) can couple

also to the other phonons ($^1\Gamma_2^-$, $^2\Gamma_3^-$ and $^3\Gamma_4^-$). The polarization selection rules for $^2\Gamma_3^-$, $^3\Gamma_4^-$ and $^3\Gamma_5^-$ phonon emission for the orthoexciton (M=0 component) are given in Ref. [55]. Since the coupling matrix between the $^3\Gamma_5^+$ states (M=0 component of the orthoexciton) and the dipole operator ($^3\Gamma_4^-$) via the $^1\Gamma_2^-$ phonon is diagonal [60], the polarization selection rules of the $^1\Gamma_2^-$ phonon replica are the same as for the Γ_{5i}^+ ($i = x, y, z$) components of the quadrupole excited M=0 state.

The matrix element for non-polar optical phonon emission is given by:

$$|M_{op}^{(j)}|^2 = \frac{\hbar D_j^2}{2\rho E_{op}^{(j)} V}\, \chi^{(j)}\, (1 + f_{ex})(1 + f_{op}) \qquad (4.3)$$

with the exciton (f_{ex}) and optical phonon (f_{op}) occupation number, the volume V, the energy of the optical phonon $E_{op}^{(j)}$ and the optical phonon deformation potential D_j in units of eV/cm. For an allowed phonon emission process and constant phonon dispersion no phonon wave vector ($\mathbf{q}$) dependence of equation 4.3 is expected. For forbidden processes, however, equation 4.3 is proportional to $\mathbf{q}^2$. By observing the exciton cooling rate due to optical phonon emission to the orthoexciton D_5 $\chi^{(5)} = 0.17 \pm 0.02$ eV/Å was determined [61]. Since the emission rate of optical phonons is proportional to the square of the deformation potential (equation 4.3) divided by the phonon energy, the deformation potentials of the $^2\Gamma_3^-$ and $^3\Gamma_4^-$ are about 0.7 times the deformation potential of the $^3\Gamma_5^-$ phonon as it can be deduced from relative intensities of resonant Raman spectroscopy [56]. The optical phonon emission to the paraexciton is expected to be much weaker.

4.2 $^2\Gamma_3^-/^3\Gamma_5^-$ optical phonon assisted luminescence

4.2.1 Magnetic field induced symmetry breaking

Without external perturbation only the $^3\Gamma_5^-$ phonon couples with a photon ($^3\Gamma_4^-$ dipole) to the paraexciton ($^1\Gamma_2^+ \otimes {}^3\Gamma_5^- = {}^3\Gamma_4^-$). In this process a nearby green P exciton state of $^3\Gamma_4^-$ symmetry serves as an intermediate state. The $^1\Gamma_2^-, ^2\Gamma_3^-, ^3\Gamma_4^-$ phonon emission is forbidden ($^1\Gamma_2^+ \otimes (^1\Gamma_2^-, ^2\Gamma_3^-, ^3\Gamma_4^-) \neq {}^3\Gamma_4^-$). In a magnetic field, however, they become allowed by the admixture (coefficient a_O equation 2.26) of the M=0 component of the $^3\Gamma_5^+$ orthoexciton into the paraexciton ($^3\Gamma_4^-$ is contained in $^3\Gamma_5^+ \otimes (^1\Gamma_2^-, ^2\Gamma_3^-, ^3\Gamma_4^-)$). In order to study the B-field dependence of the $^2\Gamma_3^-$ phonon emission of the paraexciton, the laser was set to the orthoexciton resonance (M=0 component), since orthoexcitons convert to paraexcitons [49] and the orthoexciton absorption is expected to

be independent of the magnetic field. The inset in Figure 4.2 shows the dependence of the ratio of the integrated luminescence intensity of the $^2\Gamma_3^-$ and $^3\Gamma_5^-$ phonon replica on the magnetic field. The experimental data follow

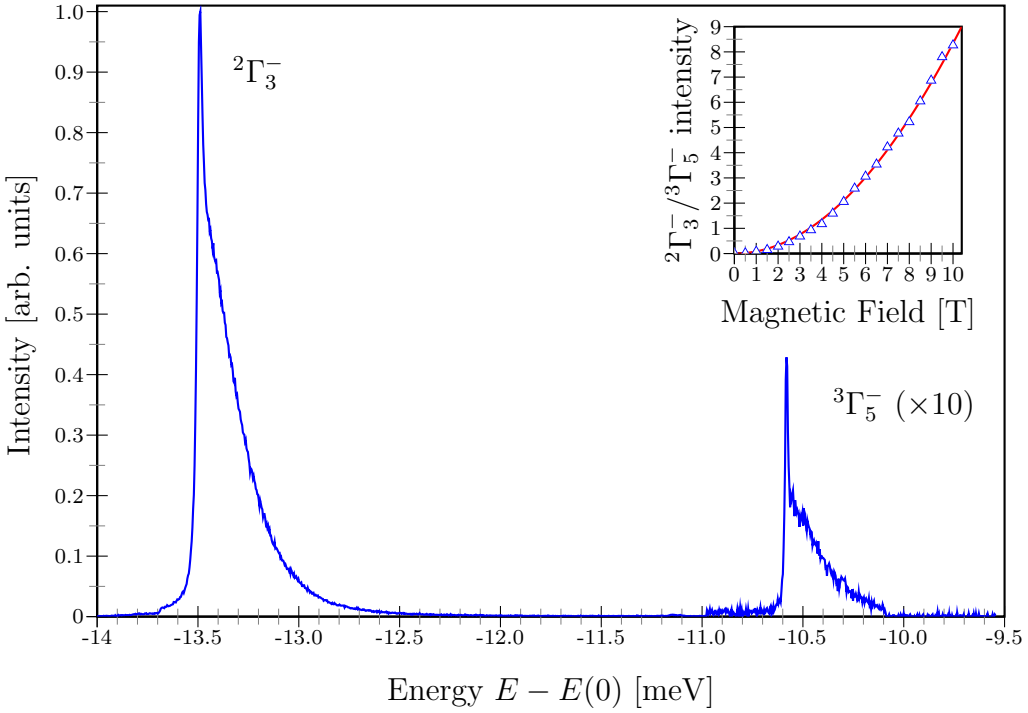

Figure 4.2: $^2\Gamma_3^-$ and $^3\Gamma_5^-$ phonon replica of paraexciton for resonant excitation of paraexciton at 10 T in Faraday configuration ($\mathbf{k} \parallel [1\bar{1}0]$) and 1.2 K measured on the H12 sample; Note: factor 10 enlargement of $^3\Gamma_5^-$ replica. Inset: ratio $^2\Gamma_3^-/^3\Gamma_5^-$ of integrated luminescence of phonon replica $^2\Gamma_3^-$, $^3\Gamma_5^-$; solid line: B^2-dependence.

a B^2-dependence, as expected from equation 2.26. The ratio

$$^2\Gamma_3^-/^3\Gamma_5^- = A\frac{\chi^{(3)}}{\chi^{(5)}} \tag{4.4}$$

deduced from equation 4.2 yields a factor of $A = 5.8 \cdot 10^3$ higher emission rate for the coupling of the $^2\Gamma_3^-$ phonon to the $^3\Gamma_5^+$ component of the paraexciton than the coupling of the $^3\Gamma_5^-$ to the $^3\Gamma_5^+$ and the $^1\Gamma_2^+$ component of the paraexciton where the latter coupling process is independent of the magnetic field. An explanation for the greater strength of the emission of a $^2\Gamma_3^-$ needs a consideration of the individual electronic steps involved in the transitions [62]. The probability for the scattering of an electron from a valence band

state $|V\rangle$ to a conduction band state $|C\rangle$ via an intermediate state $|\alpha\rangle$ under emission or absorption of an optical phonon of the energy $E_{op}^{(i)}$ is proportional to [63]:

$$\sum_{\alpha}\left[\frac{\langle C|\mathbf{e}\cdot\mathbf{p}|\alpha\rangle\langle\alpha|H_{e-ph}|V\rangle}{E_V - E_\alpha \pm E_{op}^{(i)}} + \frac{\langle C|H_{e-ph}|\alpha'\rangle\langle\alpha'|\mathbf{e}\cdot\mathbf{p}|V\rangle}{E_C - E_\alpha \mp E_{op}^{(i)}}\right], \qquad (4.5)$$

where H_{e-ph} refers to the electron-phonon interaction and E_V and E_C to the energy of the valence band and conduction band, respectively. Disregarding the spin ($^2\Gamma_6^+$) in the following consideration, the nearest conduction band has $^1\Gamma_1^+$ symmetry. Therefore the first term in equation 4.5 is only non zero, if the intermediate state $|\alpha\rangle$ is a $^3\Gamma_4^-$ state. A deep valence band of this symmetry is found 5.6 eV below the highest valence band [64], but since the state is so far off in energy, the denominator of the first term is large and hence the transition probability is low. With the same argument, the electron-phonon interaction Hamiltonian H_{e-ph} in the second term has to have the same symmetry as the intermediate state $|\alpha'\rangle$ in order to obtain a non-zero matrix element. While neglecting the spin again, the next higher conduction band has $^2\Gamma_3^-$ symmetry. The next band with $^3\Gamma_5^-$ symmetry is a very high lying conduction band [64]. This explains the greater emission strength of the $^2\Gamma_3^-$ compared to the $^3\Gamma_5^-$ phonon.

4.2.2 Raman cross section

The $^2\Gamma_3^-$ and $^3\Gamma_5^-$ phonon replica of the paraexciton for excitation in the paraexciton resonance at 10 T are shown in Figure 4.2. Subtracting the thermal distribution from the spectrum yields resonances (Figure 4.3), which are interpreted as a resonance Raman effect (ingoing resonance at $k = k_0$). $E = 0$ corresponds to $E(0) - E_{op}^{(i)},\ i = 3, 5$ with an uncertainty of $\pm 5\mu eV$ showing that the resonances are not at $k = 0$ but at $k = k_0$. The resonances can be fitted by Lorentzians of width γ_i, $(i = 3, 5)$ of the corresponding phonon emission convolved with a slit function to account for the finite spectral resolution of $10\,\mu$eV. As shown in Figure 4.3, the width $\gamma_3 \approx 21\,\mu$eV of the $^2\Gamma_3^-$ phonon emission is a factor 2.5 larger than the width $\gamma_5 \approx 8\,\mu$eV of the $^3\Gamma_5^-$ phonon emission. The energies of the two phonons are determined to $E_{op}^{(3)} = 13.49$ meV and $E_{op}^{(5)} = 10.58$ meV.

Initially one may think that the width of the phonon emission peak corresponds to the width of the resonance since it is an ingoing resonance Raman scattering process (see section 4.1). In the following paragraphs, however, it will be shown that the width of the resonance is $< 1\,\mu$eV. Nor the emission width represents the width of the optical phonon since the data obtained by

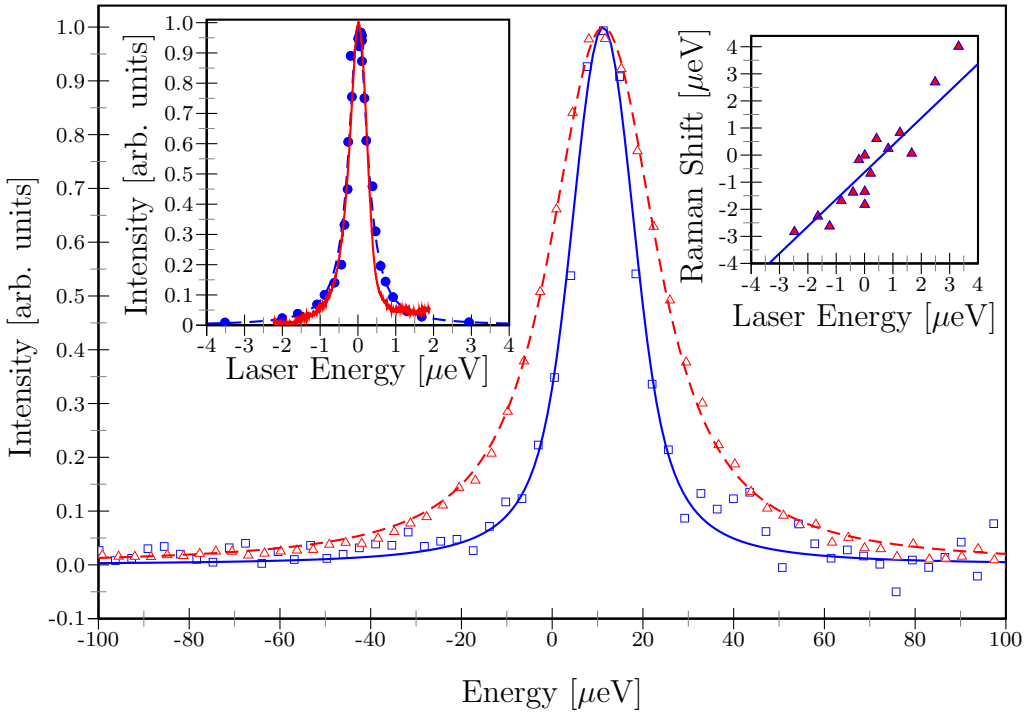

Figure 4.3: Resonance Raman lines from Figure 4.2 after subtraction of thermal distribution: Full line and squares, $^3\Gamma_5^-$ phonon; dashed line and triangles, $^2\Gamma_3^-$ phonon. $E = 0$ corresponds to $E(0) - E_{op}^{(i)}$, $i = 3, 5$; solid ($i = 5$) and dashed ($i = 3$) line: fit to data by Lorentzians of width γ_i and corrected for finite spectral resolution (10 μeV). Left inset: Dependence of $^2\Gamma_3^-$ Raman peak on laser energy. Full dots: experimental results; dashed line: fit to data by a Lorentzian; full line: absorption spectrum measured on the same sample. Right inset: Dependence of the $^2\Gamma_3^-$ Raman peak on laser energy; solid line: fit to data by a line with slope 1.

excitation spectroscopy presented in the next chapter reveal that the actual width of the $^3\Gamma_5^-$ phonon is at least a factor of two smaller[1]. The measured width of the phonon may be explained by a high occupation of states around k_0 due to the quasi-equilibrium created by the cw-excitation (hot luminescence).

Nevertheless, since the width of the $^3\Gamma_5^-$ peak is still small and the kinetic energy $E(k_0)$ is 13.2 μeV [21] above $E(0)$, it should allow to identify an extra peak due to a phonon emission from a BEC at $k = 0$. Up to now, however,

[1]The observed emission width of the $^3\Gamma_5^-$ phonon is not determined by the finite spectral resolution of the detection system since the laser line still shows a smaller width on the camera.

there is no evidence for such a scenario.

The left inset in Figure 4.3 shows the intensity dependence of the ${}^2\Gamma_3^-$ Raman peak on laser energy. The solid line represents an absorption spectrum measured on the same sample. Apparently, the absorption profile is reproduced by the ingoing resonance of the Raman effect.There are deviations between the absorption and emission data mainly in the tails which might be due to different spots on the sample in the absorption and emission experiments. Tuning the energy of the exciting laser shows a linear dependence of the energetic position of the ${}^2\Gamma_3^-$ Raman peak on the laser energy as it is expected for a Raman transition (right inset in Figure 4.3). Both, the intensity depence of the peak and the linear dependence of the peak energy on laser energy confirm the interpretation of the peak as a resonance Raman effect.

4.3 ${}^1\Gamma_2^-/{}^3\Gamma_4^-$ optical phonon assisted luminescence

Besides the ${}^2\Gamma_3^-$ and ${}^3\Gamma_5^-$ phonon replica it was possible to measure the ${}^1\Gamma_2^-$ (Figure 4.4) and the ${}^3\Gamma_4^-$ (Figure 4.5) phonon emission. The narrow line L_I at $-42.72\,\mathrm{meV}$ (Figure 4.4) is probably due to a bound exciton emission. From the data one obtains for the energy of the ${}^1\Gamma_2^-$ phonon $E_{op}^{(2)} = 43.31$ meV, which agrees well with Ref. [46]. The width of the ${}^1\Gamma_2^-$ phonon emission was determined to $\gamma_2 \approx 26\ \mu$eV.

The ${}^3\Gamma_4^-$ phonon has to be considered as a polariton because it is dipole allowed. Thus, one expects a splitting into a single longitudinal ($E_{LO}^{(4)} = 18.90$ meV) and doubly degenerate transversal components ($E_{TO}^{(4)} = 18.59$ meV). The data confirms the splitting of $0.31\,\mathrm{meV}$ [56]. The width of the low energy component of the ${}^3\Gamma_4^-$ phonon emission was determined to $\gamma_4 \approx 37\ \mu$eV.

The inset in Figure 4.4 shows phonon-assisted luminescence from the high energy ${}^3\Gamma_4^-$ to the orthoexciton. For this measurement the entrance slit of the monochromator had to be opened because the signal was to weak to be measured with fully closed slit. Due to the resulting reduction of resolution no Raman peak is visible. However, the energetic positions of $E_{LO,2}^{(4)} = 82.5$ meV and $E_{TO,2}^{(4)} = 78$ meV and the splitting of 4.5 meV [46, 56] can be confirmed. This phonon assisted process could not be observed as a Raman process to the paraexciton since this low energy emission is superimposed by vacancy emission in the same spectral region [29].

No ${}^3\Gamma_5^+$ ($E_{op}^{(5+)} = 63.9$ meV [46]) phonon assisted luminescence to the 1S excitons can be observed. Due to its positive parity the phonon transition is

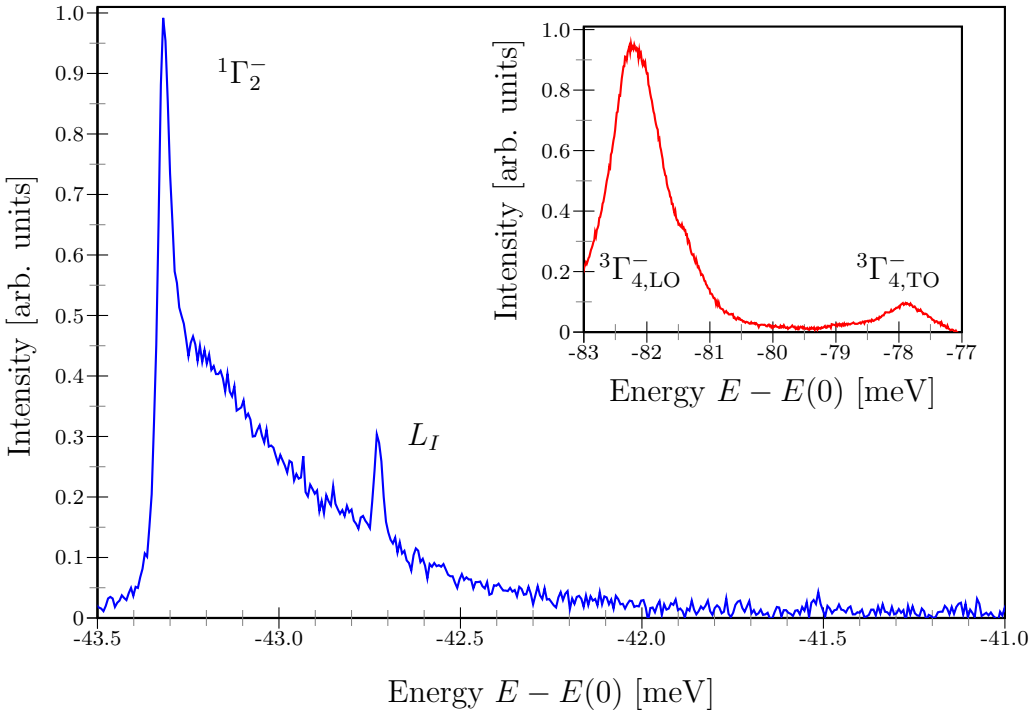

Figure 4.4: $^1\Gamma_2^-$ phonon-assisted luminescence of paraexciton for resonant excitation of the paraexciton at 10 T in Voigt configuration, $\mathbf{k} \parallel [001]$, and 1.3 K (H35 sample). Inset: High energy $^3\Gamma_4^-$ phonon-assisted luminescence to the orthoexciton for resonant excitation of the orthoexciton measured with increased monochromator slit width (H35 sample).

not dipole allowed for resonant excitation (quadrupol) and the next higher order emission, the quadrupole emission is too weak.

4.4 Two optical phonon assisted luminescence

With the method of resonant excitation of paraexcitons it is even possible to detect two-phonon processes. Figure 4.6 shows two-phonon sidebands of the paraexciton at 10 T. From the energy shift of 24.2 meV and 27.2 meV these resonances can be assigned to $(^2\Gamma_3^- + {}^3\Gamma_5^-)$ and $2 \times {}^2\Gamma_3^-$ processes, respectively. Although a two-phonon Raman process is forbidden due to parity, one observes a luminescence signal. The scattering becomes allowed with increasing k since the distance to the zone center increases and parity is no longer conserved (see section 4.1).

As discussed previously, for a forbidden process the matrix element (equa-

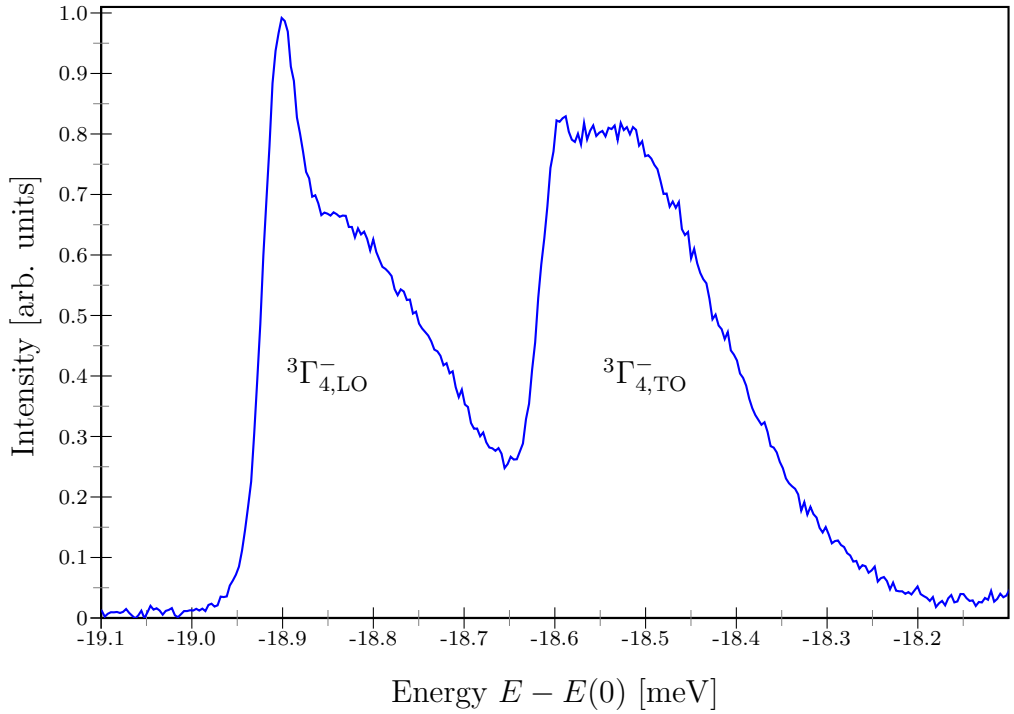

Figure 4.5: Low energy $^3\Gamma_4^-$ phonon-assisted luminescence of paraexciton for resonant excitation of paraexciton at 10 T ($\mathbf{k} \parallel [111]$) and 1.3 K (H15 sample).

tion 4.3) is proportional to the square of the phonon wave vector $\mathbf{q}$. The phonon wave vector q is the difference of the exciton wavevector and the wave vector of the final scattering state on the light line. Hence scattering from large exciton wave numbers k is favored compared to scattering from $k = k_0$ and one does not observe a Raman resonance.

The two phonon lines can be distinguished from excitons bound to impurities by variation of the excitation intensity. For high excitation intensities $I = 3$ kW/cm^2 impurity lines are saturated (solid line in Figure 4.6) whereas for low excitation intensities $I = 1$ W/cm^2 (dotted line in Figure 4.6) the phonon replica are much weaker compared to the impurity lines.

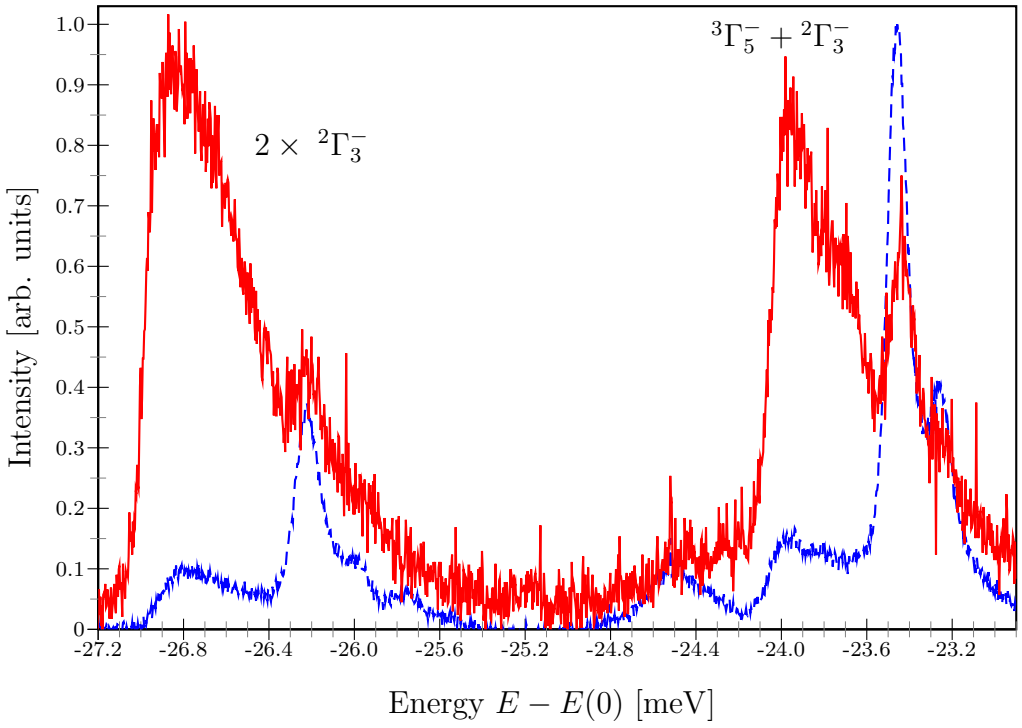

Figure 4.6: Two-phonon assisted paraexciton luminescence at 10 T and 1.2 K for two different excitation intensities; $I = 3$ kW/cm^2, solid line; $I = 1$ W/cm^2, dashed line.

4.5 Summary

It has been shown that exciting the orthoexciton the ratio of the integrated intensity of the paraexciton $^2\Gamma_3^-$ and $^3\Gamma_5^-$ phonon replica depends quadratically on the magnetic field. The emission rate of the $^2\Gamma_3^-$ phonon assisted luminescence to the paraexciton was found to be a factor of $A = 5.8 \cdot 10^3$ higher than the emission rate of the $^3\Gamma_5^-$ phonon assisted luminescence to the paraexciton.

By excitation in the orthoexciton or at even higher energy (phonon sideband of the orthoexciton or band to band transitions), the thermal distribution of paraexcitons was observed in former experiments only via the emission of $^3\Gamma_5^-$ phonons [65, 52]. Resonant excitation yields in addition a Raman peak, which can be clearly resolved by high resolution spectroscopy for the $^1\Gamma_2^-$, $^2\Gamma_3^-$, $^3\Gamma_4^-$ and $^3\Gamma_5^-$ optical phonons. As expected, the $^3\Gamma_4^-$ phonon replica shows a splitting of 0.31 meV into a longitudinal and transversal components. All phonons exhibit a different emission width of the resonance Raman peaks

which is summarized in Tab. 4.1. For the narrow ${}^3\Gamma_5^-$ emission ($\gamma_5 = 11\,\mu$eV)

Phonon	$E_{op}^{(i)}$ [meV]	γ_i [μeV]
${}^3\Gamma_5^-$	10.58	8
${}^2\Gamma_3^-$	13.49	21
${}^3\Gamma_{4,TO}^-$	18.59	–
${}^3\Gamma_{4,LO}^-$	18.90	37
${}^1\Gamma_2^-$	43.32	26
${}^3\Gamma_{4,TO/2}^-$	78	–
${}^3\Gamma_{4,LO/2}^-$	82.5	–

Table 4.1: Measured phonon energies $E_{op}^{(i)}$ and phonon emission widths γ_i for different optical phonons.

the resolution of about 10 μeV should allow to detect a population of paraexcitons at $k = 0$ caused by BEC. Up to now, however, there is no evidence for such a scenario.

The results of this chapter have been published in Ref. [66].

5

Two-phonon excitation spectroscopy

For a weakly interacting Bose gas of excitons, the critical density n_c depends only on the product of exciton mass M_x and critical temperature T_c:

$$n_c = g\,\zeta(3/2)\left(\frac{M_x\,k_b\,T_c}{2\pi\hbar^2}\right)^{3/2}, \tag{5.1}$$

where g denotes the degeneracy and $\zeta(3/2)$ the Riemann ζ function. The exciton mass is therefore an important parameter to calculate a BEC phase diagram.

In the literature, however, there is a long lasting debate about the mass of the 1S excitons. Since the extend of the exciton wave function in momentum space leads to a contribution of non-zone center areas of the Brillouin zone (compare section 2.2), the effective mass of the excitons is increased compared to the yellow P excitons series, which is given by the sum of the electron $m_e = 0.99\,m_0$ and hole $m_h = 0.69\,m_0$ masses [67]. Experimentally, for the orthoexciton masses between $2.7\,m_0$ [68] and $3.0\,m_0$ [69, 61] were found, and for the paraexciton values of $2.2\,m_0$ [70] and $2.7\,m_0$ [71] were claimed.

The high resolution in excitation of the setup and the possibility to excite the paraexciton directly offers the unique possibility to clarify this issue unambiguously as shown in the following paragraphs. The merit of the high resolution setup is the narrow laser band width of only a few neV that is particularly interesting in an excitation spectroscopy experiment since it determines the resolution of the measurement. The idea of the following experiment is to use this high resolution in order to analyze the optical phonon assisted absorption to the para- and orthoexciton with respect to additional second order acoustic phonon scattering.

By taking advantage of energy and momentum conservation of LA scattering processes with paraexcitons, simple formulas can be derived that allow the determination of the paraexciton mass M_P, refractive index n, and the

kinetic energy E_0 with the LA sound velocity as the only input parameter. As demonstrated in the last part of this chapter, the situation for the orthoexciton is far more complex due the k^2-dependent exchange interaction induced splitting and anisotropic selection rules of acoustic and optical phonon scattering processes.

5.1 Determination of the paraexciton mass

In order to determine the paraexciton mass M_P the laser was tuned one optical ${}^3\Gamma_5^-$ phonon above the paraexciton resonance. The H13 sample ($\mathbf{k} \parallel [1\bar{1}0]$) was cooled in superfluid helium to the temperature $T = 1.2$ K in a magnetic field of 10 T in Faraday configuration. The monochromator wavelength was centered around the paraexciton resonance and the paraexction quadrupole emission intensity was monitored in dependence of increasing laser energy $E_L = E_P + E_{op}^{(5)} + E$, where E_P and $E_{op}^{(5)}$ are the paraexciton and ${}^3\Gamma_5^-$ optical phonon energy, respectively. Here the wavemeter serves as a reliable reference for the exact laser energy. Figure 5.1 shows the resulting two-phonon excitation spectrum.

The Stokes Raman transition to paraexcitons with kinetic energy (k_0,E_0) is centered around $E = 0$ and, for reference, normalized to 1. For $0 < E < E_1$ excitons are excited by the a ${}^3\Gamma_5^-$ phonon emission and are monitored after relaxation by quadrupole emission of the paraexciton. Since it is a dipole excitation process, the phonon couples not only to the admixed ${}^3\Gamma_5^+$ component but also to the ${}^1\Gamma_2^+$ component (${}^3\Gamma_4^- \otimes {}^3\Gamma_5^- = {}^1\Gamma_2^+ \oplus {}^2\Gamma_3^+ \oplus {}^3\Gamma_4^+ \oplus {}^3\Gamma_5^+$). The polarization of the exciting laser light is chosen perpendicular to the polarization of the quadrupole emission, which is actually favored by selection rules and easily allows a good suppression of scattered laser light with an analyzer in front of the monochromator set to the quadrupole emission polarization.

The optical phonon assisted absorption is expected to follow $\sqrt{E + E_0}$ due to the density of states of the paraexciton [62]. As shown in the inset, at $E = E_1$ the emission of an additional longitudinal acoustic phonon sets in, stays up to $E = E_2$ and thus leads to the enhanced quadrupole emission.

The whole spectrum can be fitted with the function

$$\begin{aligned} f(x,\gamma) &= A_1 \int_{-E_0}^{\infty} \sqrt{\xi + E_0} \cdot \tfrac{(\gamma/2)^2}{(\gamma/2)^2+(\xi-x)^2} d\xi \\ &\quad + A_2 \tfrac{(\gamma/2)^2}{(\gamma/2)^2+x^2} \\ &\quad + A_3 \int_{E_1}^{E_2} \tfrac{(\gamma/2)^2}{(\gamma/2)^2+(x-\xi)^2} d\xi. \end{aligned} \qquad (5.2)$$

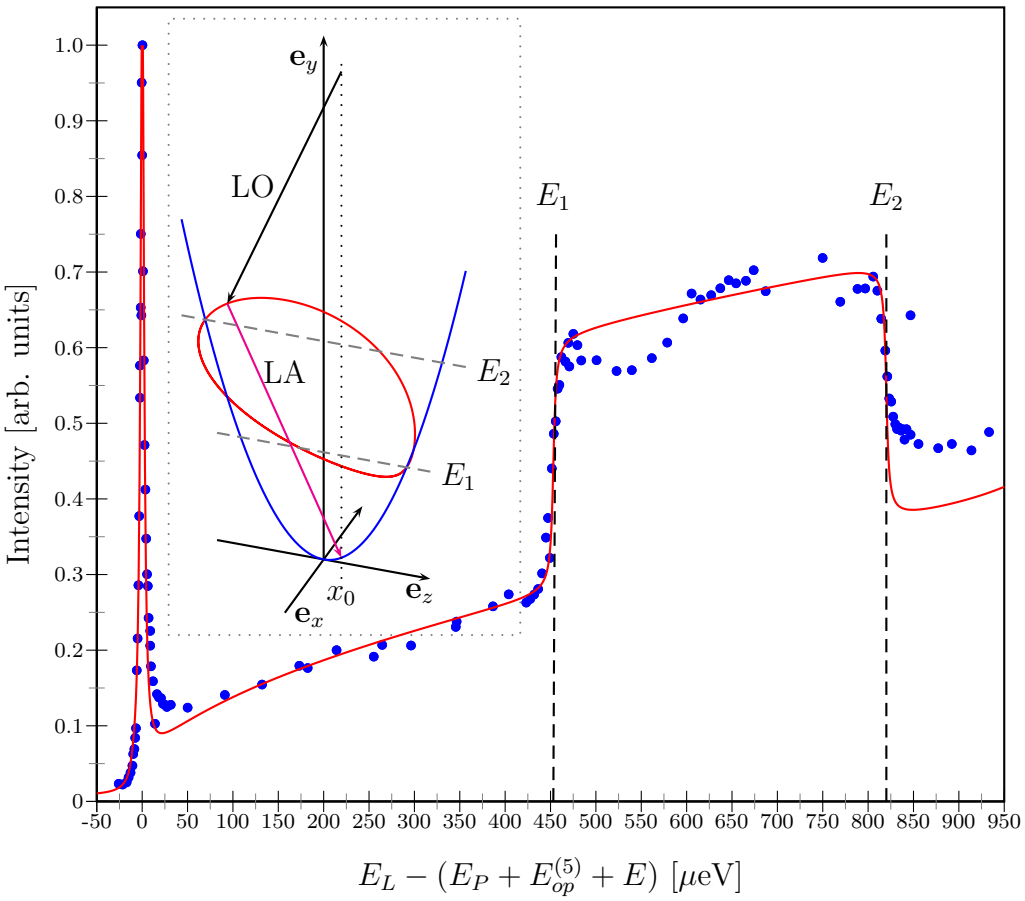

Figure 5.1: Two-phonon excitation spectrum at 1.2 K monitored as quadrupole emission of paraexciton at $E_P = 2.020598$ eV. $E = 0$ corresponds to a laser energy $E_L = E_P + E_{op}^{(5)} = 2.031178$ eV. Full dots, experimental points; solid line is a fit to a Lorentzian (FWHM= 4.5 μeV) for the LO-phonon resonant process, a square-root dependent background and a plateau for the region of LO and LA phonon processes. Inset: schematics of the LO- and LA-phonon scattering; blue parabola exciton dispersion; red curve, possible energy and momentum hypersurface for LA scattering to k_0 (magenta arrow); black arrow, LO phonon scattering; dotted line, light dispersion.

In the first term, the density of states of the paraexciton is convoluted with a Lorentzian with the width γ of the ${}^3\Gamma_5^+$ phonon to consider the optical phonon assisted absorption. The second term is caused by the Stokes Raman transition, which is described by a Lorentzian of width γ. The third term, a simple plateau, expressed by an integral over a Lorentzian of width γ, takes

into account the additional LA phonon scattering. All terms are weighted with an appropriate scaling factor A_i.

For the optical and as well for the acoustic phonon scattering no selection rule dependence on the scattering wave vector and hence on the scattering energy is expected. The paraexciton is fully isotropic and the anisotropy of the admixed M=0 orthoexciton component can be neglected since the k^2-dependent exchange interaction is of no relevance at high magnetic fields. Nevertheless, a slight deviation is observed for the LA scattering process that seems to depend on the scattering energy. Moreover $f(x, \gamma)$ underestimates the data on the high energy side of the spectrum. One has to keep in mind that it was important to keep the experimental conditions like laser energy, laser power, and in particular the temperature in the VTI, as stable as possible. The experiments are time consuming and when the helium level in the VTI runs low the temperature drops slightly. Thus, the intensity of the quadrupole emission deviates from its former value. In order to compensate for this effect the measurement was performed several times.

Due to the high quality of the data the rise and fall of the LA scattering plateau are determined with errors of only a few μeV to $E_1 = (453 \pm 3)\,\mu$eV and $E_2 = (820 \pm 3)\,\mu$eV. The analysis of the kinematics yields simple expressions[1] for the paraexciton mass M_P, the kinetic energy E_0 and the refractive index n:

$$\begin{aligned} M_P &= \frac{1}{4m_0c^2}\left(\frac{c}{v_{LA}}\right)^2 (E_2 + E_1), \\ n &= \frac{1}{4E_P}\left(\frac{c}{v_{LA}}\right)(E_2 - E_1), \\ E_0 &= \frac{1}{8}\frac{(E_2 - E_1)^2}{(E_2 + E_1)}. \end{aligned} \qquad (5.3)$$

The equation of the kinetic energy is particularly interesting since it solely depends on the sum and on the difference of the energy readings. The determination of the exciton mass apparently needs no additional input parameter but the sound velocity. For the velocity of sound $v_{LA} = 4.63 \cdot 10^3$ ms^{-1} was used. This value[2] is calculated from the room temperature measurements ($v_{LA} = 4.56 \cdot 10^3$ ms^{-1}) from Ref. [24]) taking into account the temperature dependence of the elastic constants [25]. From equation 5.3 one derives the following values: $M_P = 2.61 \pm 0.04$, $n = 2.94 \pm 0.05$ and $E_0 = (13.2 \pm 0.2)\,\mu$eV.

[1] The derivation of the formulas can be found in the appendix A.

[2] This value of the sound velocity was used in Ref. [21]. The small corrrections that arise due to the Brillouin scattering experiments presented in the next chapter are within the stated errors.

The errors are calculated from the errors of E_1, E_2 and a 1% error of v_{LA}. It should be noted that this method allows to determine E_0 and thus n^2/M_P solely from E_1 and E_2. With an independent measurement of n one can thus determine M_P without knowledge of v_{LA} and therefore even measure v_{LA}.

Additionally to the determination of the paraexciton mass, the measurement allows statements about the optical phonon. The resonance at $E = 0$ is broadened because of the finite lifetime of the phonon. The width obtained by the fit with a Lorentzian is determined to a full width at half maximum of 4.5 μeV. In contrast to the Raman process discussed in section 4.2.2 this resonant Raman process has an outgoing resonance and therefore its width represents the width of the optical phonon and the electronic state which can be neglected (80 neV for the paraexciton).

Furthermore, from the reading of the high precision wavemeter of the paraexciton resonance E_P and the laser reading at the phonon-assisted resonance ($E_P + E_{op}^{(5)}$), one gets a very accurate value for the phonon energy $E_{op}^{(5)} = (10.58 \pm 0.01)$ meV.

5.2 Two-phonon excitation of the orthoexciton

The results of the last section motivate to perform an analog experiment on the orthoexciton. As k^2-dependent exchange interaction lifts the degeneracy and leads two different anisotropic masses of the orthoexciton states, the spectrum is expected to be far more rich and complicated.

Figure 5.2 shows such a spectrum obtained by tuning the laser one ${}^3\Gamma_5^-$ optical phonon above the orthoexciton resonance with the photon wave vector $\mathbf{k} \parallel [1\bar{1}0]$. Like in the case of the paraexciton, the sharp peak at $E = 0$ corresponds to the Raman transition with the ${}^3\Gamma_5^-$ phonon to k_0.

Contrary to the paraexciton, a fit with a Lorentzian yields a peak width $\gamma_z \approx 10$ μeV that is by about a factor of two larger than the width of the optical ${}^3\Gamma_5^-$ phonon. For explanation one has to take into account that there are three final states $\mathbf{\Psi}_{\mathrm{O}}^{(1)}$, $\mathbf{\Psi}_{\mathrm{O}}^{(2)}$ and $\mathbf{\Psi}_{\mathrm{O}}^{(3)}$ with distinct kinetic energies $E_{\mathrm{O}}^{(1)}$, $E_{\mathrm{O}}^{(2)}$ and $E_{\mathrm{O}}^{(3)}$ (see energy level diagram in the right hand inset of Figure 5.2), the second of which ($\mathbf{\Psi}_{\mathrm{O}}^{(2)}$) is the only one that is quadrupole allowed in emission whereas the others ($\mathbf{\Psi}_{\mathrm{O}}^{(1)}$, $\mathbf{\Psi}_{\mathrm{O}}^{(3)}$) have no oscillator strength. Besides the emission selection rules, the dipole excitation selection rules have to be taken into account, too. They are calculated in the same way as the optical phonon emission selection rules $\chi^{(j)}$ (equation 4.2). Both, quadrupole oscillator strength and ${}^3\Gamma_5^-$ optical phonon selection rules, are shown in the lower left and middle panel of Figure 5.3, respectively. For the calculation a

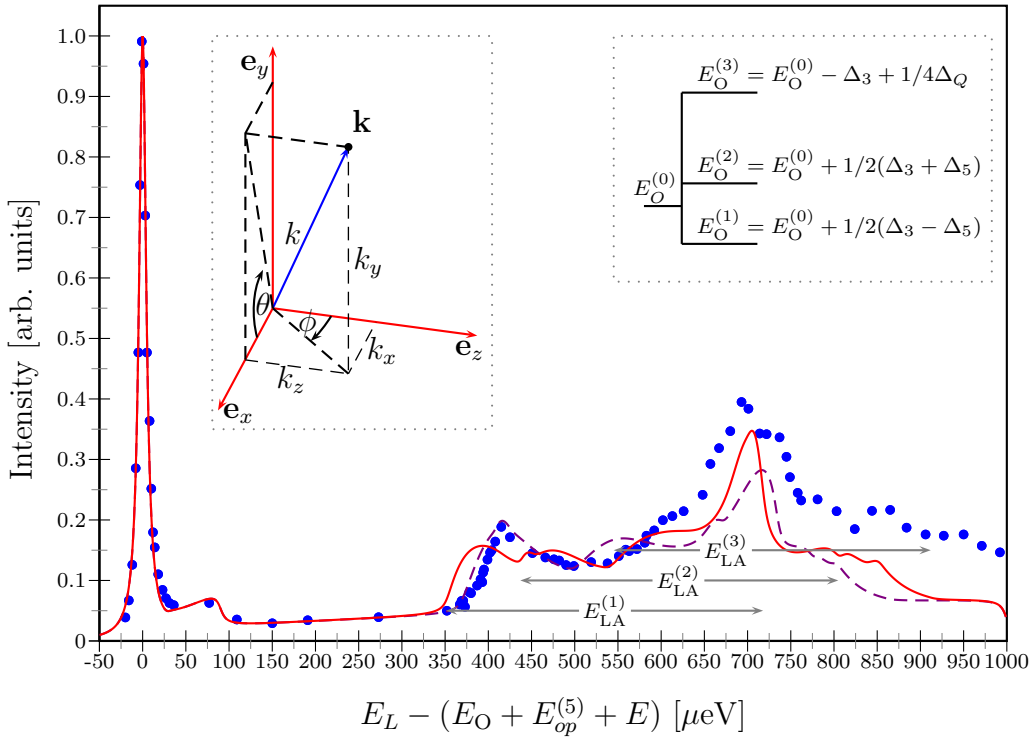

Figure 5.2: Two-phonon excitation spectrum at 1.2 K monitored as quadrupole emission of orthoexciton at $E_O = 2.032786$ eV. $E = 0$ corresponds to a laser energy $E_L = E_O + E_{op}^{(5)} = 2.043366$ eV. Full dots, experimental points; red solid line / violet dashed line, theoretical curve as explained in the text; gray arrows, energy range for LA scattering from $\mathbf{\Psi}_O^{(j)}$; left hand inset, used coordinate system; right hand inset, energy level diagram for $\mathbf{k} \parallel [1\bar{1}0]$.

spherical coordinate system (angles ϕ and θ) is introduced. As shown in the left hand inset of Figure 5.2, the angle ϕ marks rotations around $\mathbf{e}_y$ while the angle ψ marks rotations around the optical axis $\mathbf{e}_z$. For $\phi = 0$ the angle θ is equivalent to the orientation ψ of the linear polarization ($\mathbf{e}$) of the exciting laser.

The ${}^3\Gamma_5^-$ selection rules for excitation $\mathbf{k} \parallel [1\bar{1}0]$ are calculated for $\psi = 90^0$ since this was the linear polarization orientation during the experiment. In contrast to the oscillator strength, for $\phi = 0$, which is fixed by momentum conservation, the two states $\mathbf{\Psi}_O^{(1)}$ and $\mathbf{\Psi}_O^{(3)}$ are dipole allowed while $\mathbf{\Psi}_O^{(2)}$ can not be excited via an optical ${}^3\Gamma_5^-$ phonon. Hence, excitons that are detected via quadrupole emission must have undergone inelastic scattering processes from $E_O^{(1)}$, $E_O^{(3)}$ to $E_O^{(2)}$. The probability for such scattering is rather high

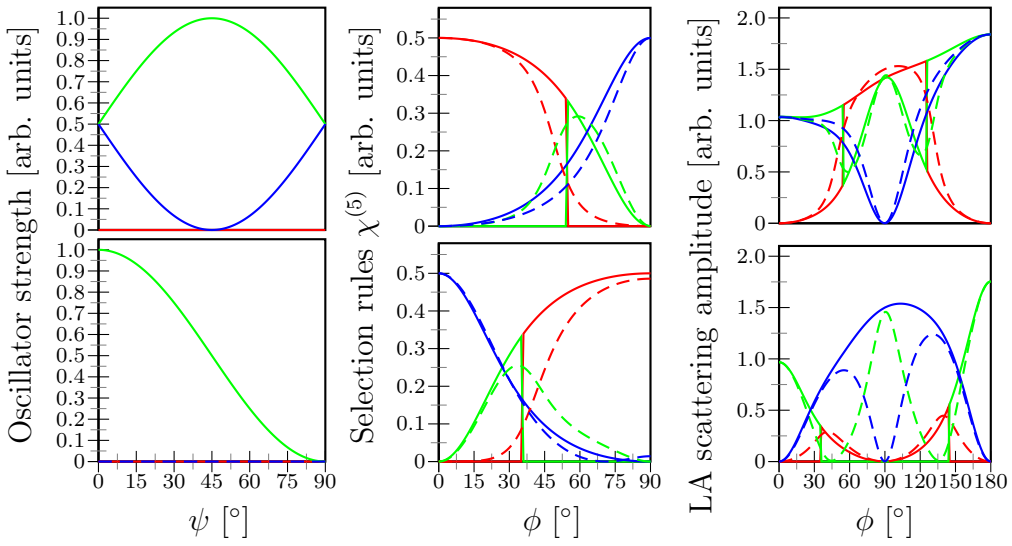

Figure 5.3: Left panels, quadrupole oscillator strength; middle panels, ${}^3\Gamma_5^-$ optical phonon selection rules, right panels, LA scattering matrix element; upper panels, $\mathbf{k} \parallel [001]$; lower panels, $\mathbf{k} \parallel [1\bar{1}0]$; blue line, $\mathbf{\Psi}_{\mathrm{O}}^{(1)}$ state; green line, $\mathbf{\Psi}_{\mathrm{O}}^{(2)}$ state, red line, $\mathbf{\Psi}_{\mathrm{O}}^{(3)}$ state; solid lines, $\theta = 0°$; dashed lines, $\theta = 20°$.

since the energy difference is less than two μeV. This superposition of two resonances, separated by the difference in energy of $E_{\mathrm{O}}^{(3)} - E_{\mathrm{O}}^{(1)} \approx 4.2$ μeV, therefore leads to a broadened resonance peak with a width of about 10 μeV.

The small subsequent plateau, which is absent in the paraexciton experiment, can be attributed to TA phonon scattering. TA scattering is allowed from $E_{TA} \approx 30$ μeV up to $E_{TA} \approx 90$ μeV and is fitted with a convolution of Lorentzians. The signal, however, is weak and will not be further investigated here. The following rise of the signal is due to the density of states of the orthoexcitons like in the paraexciton experiment and again can be fitted by a convolution of a square root dependence and a Lorentzian with a width of γ_z. The onset of the LA scattering process around $E \approx 351$ μeV is not as steep as in the paraexciton experiment, but still significant. Apparently, the energy dependency of the LA scattering process deviates from a simple plateau. Therefore, in the following a model including selection rules, kinematics and LA scattering probability is derived trying to explain the observed features.

5.2.1 Kinematical analysis

The anisotropic masses of the orthoexciton states lead to a pronounced energy dependence of the LA phonon scattering energy on the direction in

k-space.

Although the excitation with a ${}^3\Gamma_5^-$ optical phonon is along $\mathbf{k} \parallel [1\bar{1}0]$, i.e. $\theta_k = 0$, $\phi_k = 0$, due to its flat dispersion the optical phonon can contribute with any $\mathbf{k}$, and hence the initial orthoexciton state $E_{\mathrm{O}}^{(j)}(\theta_k, \phi_k)$ is characterized by the angles θ_k, ϕ_k. The final scattering state, however, is fixed at $E_{\mathrm{O}}^{(i)}(0,0)$. Contributions from $\theta_k \neq 0$ and $\phi_k \neq 0$ can be neglected since the numerical aperture $NA \approx 0.1$. Energy and momentum conservation lead to

$$E_{\mathrm{O}}^{(j)}(\theta_k, \phi_k) - E_{\mathrm{O}}^{(i)}(0,0) = \hbar v_{LA}(\theta_q, \phi_q) q, \qquad i, j = 1, 2, 3 \tag{5.4}$$

with $\theta_{k,q}$ in $[0°, 90°]$ and $\phi_{k,q}$ in $[0°, 180°]$. q denotes the absolute value of the phonon wave vector and θ_q, ϕ_q its orientation. The final states are close in energy, and therefore the dependence of scattering between to different final states ($j \neq i$) is negligible and hence omitted ($i = j$) in the calculation of the phonon scattering energy (but not in the calculation of the LA scattering probability).

Since without a magnetic field the Hamiltonian is quadratic in k, the slopes $f_j(\theta_k, \phi_k)$ of the exciton parabolas are given by

$$f_j(\theta_k, \phi_k) = E_{\mathrm{O}}^{(j)}(\theta_k, \phi_k)/k_0^2.$$

Inserting these relations and $q = \sqrt{k^2 - 2\,k_0 \cos\phi_k + k_0^2}$ into equation 5.4 and squaring the resulting expression leads to the quartic equation

$$\begin{aligned} &f_j(\theta_k, \phi_k)k^4 - [\hbar v_{LA}(\theta_q, \phi_q)^2 + 2 f_j(\theta_k, \phi_k) f_j(0,0) k_0^2]\, k^2 \\ &+2\hbar v_{LA}(\theta_q, \phi_q) k_0 k \cos\phi + f_j(0,0)^2 k_0^4 - \hbar v_{LA}(\theta_q, \phi_q)^2 k_0^2 \quad = 0 \end{aligned}$$

that is solved analytically for k with $v_{LA}(\theta_k, \phi_k)$. Only a few iterations with $v_{LA}(\theta_q, \phi_q)$ along the new obtained (θ_q, ϕ_q) direction leads to stable solutions shown in Figure 5.2.1 as function of $\phi = \phi_k$ for different $\theta = \theta_k$ and crystal orientiations (H13 and H35, see Tab. 3.1). As it has been mentioned in section 2.2.2, the shifts of the orthoexciton energy levels due to intrinsic strain are in the same order of magnitude as the k^2-dependent exchange interaction. However, the shifts can be discriminated from the exchange interaction since they do not depend on $\mathbf{k}$ but are fixed to the lattice. Therefore this perturbation only gives a small offset to the orthoexciton parabolas and can be neglected.

5.2.2 Acoustic phonon scattering probability

Compared to the Raman transition, the inclusion of an acoustic phonon in the scattering process loosens momentum conservation and the phonons can

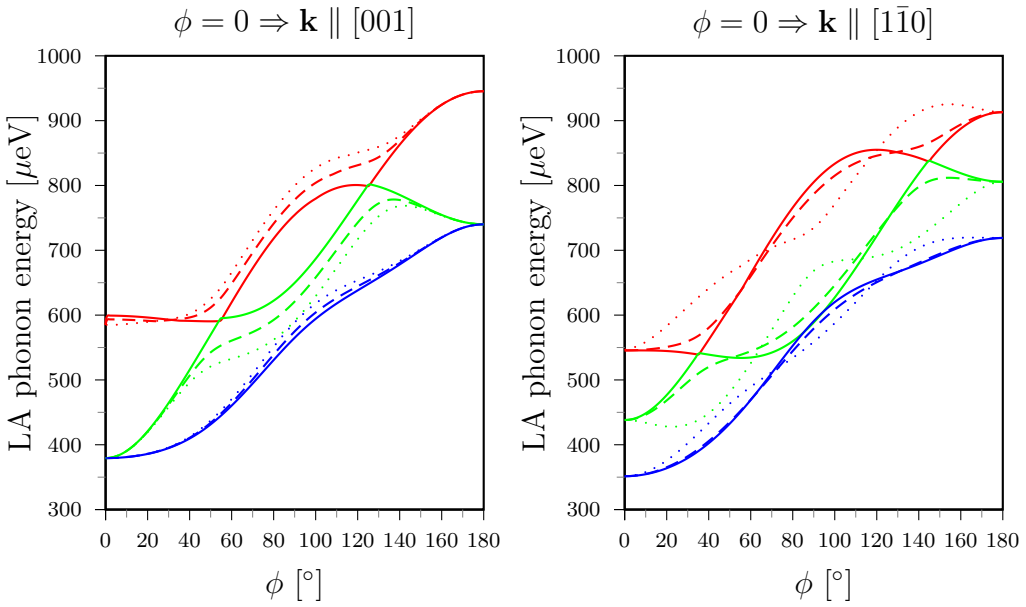

Figure 5.4: Calculated phonon scattering energies for two different crystal orientations (left figure H13, right figure H35). Blue lines, $\mathbf{\Psi}_{\mathrm{O}}^{(1)}$ state; green lines, $\mathbf{\Psi}_{\mathrm{O}}^{(2)}$ state, red lines, $\mathbf{\Psi}_{\mathrm{O}}^{(3)}$ state; solid lines, $\theta = 0°$; dashed lines, $\theta = 20°$; dashed lines, $\theta = 50°$ in the left hand figure, $\theta = 70°$ in the right hand figure.

have any $\mathbf{q}$ direction. Therefore any state in k-space can be excited via the optical phonon, and the optical selection rules depend on ϕ and θ as shown in the middle panels of Figure 5.3 for two different crystal orientations $\mathbf{k} \parallel [1\bar{1}0]$ and $\mathbf{k} \parallel [001]$. Direct excitation of the allowed emitting orthoexciton states ($\mathbf{\Psi}_{\mathrm{O}}^{(2)}$ for $\mathbf{k} \parallel [1\bar{1}0]$ and $\mathbf{\Psi}_{\mathrm{O}}^{(1)}$, $\mathbf{\Psi}_{\mathrm{O}}^{(2)}$ for $\mathbf{k} \parallel [001]$) becomes allowed for finite ϕ or θ. This direct process is mediated by hydrostatic compression via the LA phonon. But also for fixed ϕ or θ scattering between different orthoexciton sublevels can take place due to shear strain. The probability for LA scattering is therefore a function of ϕ and θ, which can be calculated using the matrices H_1, H_3, H_4 and H_5 that have been introduced in section 2.2.2. The squared matrix element for acoustic phonon scattering [72] from $\mathbf{\Psi}_{\mathrm{O}}^{(i)}$ to $\mathbf{\Psi}_{\mathrm{O}}^{(j)}$ via deformation potential interaction is given by

$$|\langle \mathbf{\Psi}_{\mathrm{O}}^{(j)} | H_k | \mathbf{\Psi}_{\mathrm{O}}^{(i)} \rangle|^2 \simeq \frac{\hbar q}{2\rho V v_l} \chi_{i\to j}^{(k)} \, \Xi_k^2 (1 + 2 f_{q,l}) \qquad (5.5)$$

with $k = 1, 2, 3$, the sound velocity v_l of the phonon $l = \mathrm{LA}, \mathrm{STA}, \mathrm{FTA}$ and $f_{q,l}$ the q-dependent occupation number of the phonon. The dimensionless factor $\chi_{i\to j}^{(k)}$ depends on the direction of the phonon wave vector, on the

polarization and the states i, j. For the H_4 interaction the deformation potential Ξ_k has to be substituted by the spin-orbit splitting energy $\alpha/3$. Since the phonon occupation number $f_{q,l} \ll 1$, it can be omitted and the LA phonon scattering probability from $\mathbf{\Psi}_{\mathrm{O}}^{(i)}$ to $\mathbf{\Psi}_{\mathrm{O}}^{(j)}$ becomes

$$W_{i\to j} \sim \frac{q}{v_{LA}} \sum_k \chi_{i\to j}^{(k)}\, \Xi_k^2. \tag{5.6}$$

Assuming that coherent scattering is favored compared to e.g. exciton-exciton scattering, equation 5.5 is multiplied by the relative oscillator strength $f_r^{(j)}$ of the final scattering state $\mathbf{\Psi}_{\mathrm{O}}^{(j)}$. Summation over all final states j yields the scattering-emission probability

$$W_i \sim \frac{q}{v_{LA}} \sum_{j=1}^{3} \sum_k f_r^{(j)} \chi_{i\to j}^{(k)}\, \Xi_k^2 \tag{5.7}$$

from the dipole excited state $\mathbf{\Psi}_{\mathrm{O}}^{(i)}$. The calculated scattering-emission probability is shown in the right panels of Figure 5.3 in dependence of ϕ for the two different crystal orientations and two different θ.

5.2.3 Sampling of the scattering spectrum

Including the optical phonon and scattering-emission selection rules in dependence of the scattering direction (θ, ϕ), a scattering probability can be assigned to each phonon energy $E_{LA}^{(i)}(\theta, \phi)$ from the kinematical analysis. In order to obtain a scattering spectrum, $E_{LA}^{(i)}(\theta, \phi)$ is sampled with a resolution of 1° in ϕ and assigned to energy bins of a width of 0.1 μeV. The corresponding bin is weighted with the optical phonon excitation selection rule $\chi^{(i)}$ multiplied by the scattering-emission probability W_i.

Since $E_{LA}(\theta, \phi)$ is a function of varying slope, the bins are not equally occupied. Therefore unoccupied bins are filled with the mean value of adjacent non-zero bins. The bins are summed up over the three excited orthoexciton states (i) and the angle θ in steps of 1°. Finally the spectrum is convoluted with a Lorentz with the width γ_z and added to the sum of a Raman Lorentz and a square root dependence like in the preceeding section 5.1 for the paraexciton two-phonon excitation spectrum.

5.2.4 Discussion

The red line in Figure 5.2 shows the calculated two-phonon scattering for the H13 crystal configuration according to the model described above with

the k^2-dependent exchange parameters from Ref. [14] and $\Delta_1 = 0$. The gray arrows mark the possible energetic scattering range from the state $\mathbf{\Psi}_{\mathrm{O}}^{(j)}$ (compare Figure 5.2.1). At first glance the curve is in qualitative agreement, and, in particular, the striking peak around 700 μeV is reproduced. A closer look shows that the model deviates in certain aspects from the measured data. Especially the rise of the scattering signal around 351 μeV is steeper in the model and shows a double structure due to the two states $\mathbf{\Psi}_{\mathrm{O}}^{(1)}$ and $\mathbf{\Psi}_{\mathrm{O}}^{(2)}$.

The experiments presented in Ref. [14] lead to values for Δ_3, Δ_5 and Δ_Q. A value for Δ_1, however, was not accessible. But here it certainly can have an impact on the spectrum. To fit the rise of the scattering signal the energetic separation of $E_{LA}^{(2)}(\theta,\phi) - E_{LA}^{(1)}(\theta,\phi)$ at $\phi = 0$, $\theta = 0$ has to be decreased. This can be done by shifting both energies with $\Delta_1 = 0.19$ μeV to lower energies and decreasing Δ_Q (compare energy level separation in the right hand inset of Figure 5.2). To get rid of the steep rise, Δ_Q has to be omitted, which is not in agreement with the experiments of Ref. [14]. The resulting spectra with $\Delta_1 = 0.19$ μeV, $\Delta_3 = -1.3$ μeV, $\Delta_5 = 1.8$ μeV and $\Delta_Q = 0$ is shown as violet dashed curve. At this point one can conclude that the exchange parameters given in Ref. [14] are reasonable and certainly 0 μeV $< \Delta_1 < 0.5$ μeV.

The interpretation becomes even more complicated looking at a two-phonon excitation spectrum for the H35 crystal configuration ($\mathbf{k} \parallel [001]$), as shown in Figure 5.5. The experiment was performed in the same way as the above experiment but with excitation and detection polarizations rotated by 90°. Actually a quick look on the quadrupole and excitation selection rules (Figure 5.3) reveals that both excitation polarizations work since k_x and k_y are interchangeable.

Firstly, it has to be noted that the width of the Raman peak is wider than in the $\mathbf{k} \parallel [1\bar{1}0]$ experiment, namely $\gamma_{z'} \approx 16$ μeV. Following the above arguments, the width of the Raman peak should be comparable to the superposition of two Lorentzians separated by the energetic difference δE of the quadrupole allowed states. For $\mathbf{k} \parallel [110]$ this corresponds to $\delta E = 3\Delta_3 \approx 4$ μeV (inset in Figure 5.5). Apparently, this is too small to explain a width of 16 μeV. Additional intrinsic strain of only a few μeV explains such a broadening since it can split the orthoexciton parabolas further apart.

The spectrum shown by the red curve is calculated again with the k^2-dependent exchange parameters from Ref. [14] and $\Delta_1 = 0$. The agreement with the data is obviously less satisfying than in the $\mathbf{k} \parallel [1\bar{1}0]$ experiment. Again the obvious peak with the step like rise at 600 μeV is reproduced quite

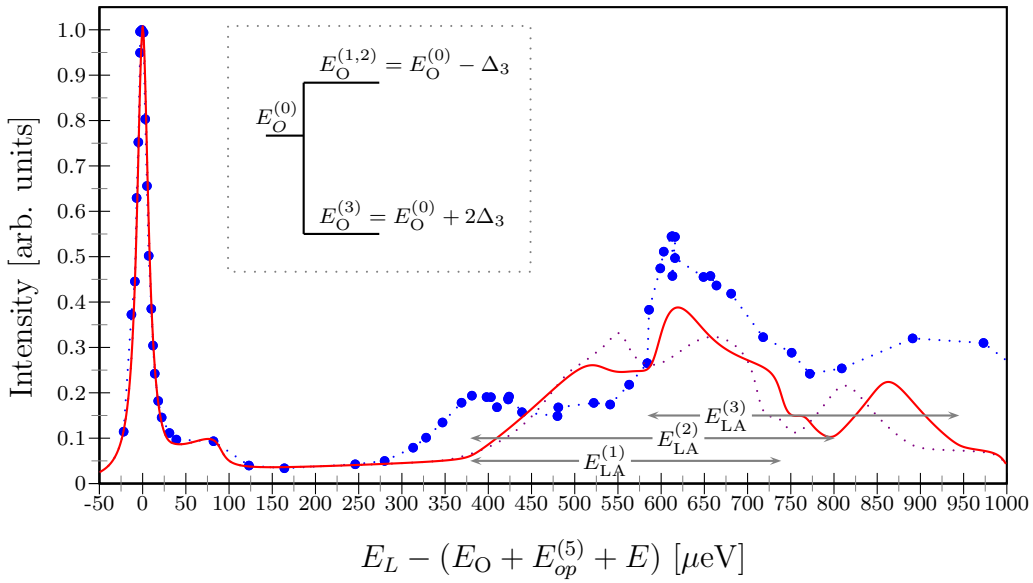

Figure 5.5: Two-phonon excitation spectrum at 1.2 K monitored as quadrupole emission of orthoexciton at $E_O = 2.032785$ eV. $E = 0$ corresponds to a laser energy $E_L = E_O + E_{op}^{(5)} = 2.043369$ eV. Full dots, experimental points; red solid line / violet dotted line, theoretical curve as explained in the text; gray arrows, energy range for LA scattering from $\mathbf{\Psi}_{\mathrm{O}}^{(j)}$; inset, energy level diagram for $\mathbf{k} \parallel [001]$.

well. The step like flank arises from the fact that even though $\mathbf{\Psi}_{\mathrm{O}}^{(3)}$ initially is not or only weakly allowed by selection for small angles, the LA phonon scattering energy stays almost constant around 600 μeV up to $\phi \approx 50°$. In contrast to the obvious peak, the slow rise of the scattering signal at about 300 μeV is not reproduced but starts at higher energies (380 μeV). From the kinematical point of view with the above given exchange and mass parameters no signal below 380 μeV should be observable and it can not be reproduced with a reasonable set of exchange parameters. Again, small possible offsets of the orthoexciton parabolas due to intrinsic strain can not explain this large shift of the rise to lower energy. One should note tuning the laser to higher energies leads to different output intensities. Before each measurement the intensity was checked with great care. Nevertheless, there can be a difference in intensity of 5% that has an impact on the spectra. It is therefore important to achieve more stable experimental conditions. As shown by the dotted line, with the preliminary fit parameters from the $\mathbf{k} \parallel [1\bar{1}0]$ measurement the model deviates even more from the measured spectrum. Apparently, there are still several obstacles to overcome on the

way to a convincing fit of the two-phonon orthoexciton spectra.

5.3 Summary

The novel method of two-phonon excitation spectroscopy provides reliable value of the paraexciton mass and solves a long lasting discussion [70]. The importance of central-cell corrections as discussed in Ref. [37] is thus confirmed. The higher background refractive index of 2.94 as compared to 2.55 [14, 20, 40] leads to detail corrections of the polariton dispersion and the anisotropic orthoexciton mass values [14, 73]. The main advantage of the method lies in the fact that reliable values of the exciton mass are obtained by a merely kinematical analysis, the accuracy of which is determined by the accuracy of the laser energy and the sound velocity.

In first experiments the method was applied to the orthoexciton, which yielded rich and complex spectra. In order to fit the spectra, a model was derived that is based on a kinematical analysis and selection rules of optical and acoustic phonons and quadrupole emission. For one crystal configuration qualitative agreement could be achieved with the exchange parameter from Ref. [14]. For the Δ_1 parameter, which was previously not accessible, a range of $0\ \mu\text{eV} < \Delta_1 < 0.5\ \mu\text{eV}$ is derived.

The results of the first part of this chapter have been published in Ref. [21].

6

Resonant Brillouin scattering

In chapter 4 inelastic scattering of optical phonons (Raman scattering) and the optical phonon assisted luminescence of the paraexciton have been examined. The possibilty of orthoexciton excitation with an optical and an additional longitudinal acoustic phonon has been studied in the preceding chapter with respect to the exciton mass and the k^2-dependent exchange parameters. This chapter deals with orthoexcitons excited *resonantly* in a magnetic field, where a fine-structure in the ${}^2\Gamma_3^-$ and ${}^3\Gamma_5^-$ optical phonon assisted emission of orthoexcitons shows up that can be attributed to intra- and interband resonant Brillouin scattering (RBS) within the orthoexciton subbands with longitudinal acoustic (LA) and transverse acoustic (TA) phonons [55].

As shown first for GaAs [74], Brillouin scattering between exciton polaritons can be observed directly. Later Brillouin scattering was observed in CdS via the additional emission of an optical phonon [75]. The observation of acoustic phonons scattered by 2-phonon processes (LA/TA and LO) has at least two advantages: First, the additional energy shift by emission of an optical phonon makes it easy to suppress scattered laser light. Second, the dispersionless LO-phonon allows the observation of final k-states, whose probability for emission of photons tends to zero because the photon contribution of the final polariton state tends to zero. In Cu_2O Brillouin scattering from the 1S excitons can only be observed by a two-phonon process because the final state has even parity and thus can only be detected by the additional emission of an optical phonon of odd parity [55]. These Brillouin scattering processes can be stimulated for sufficiently high light intensities. The processes are connected with a pronounced line narrowing compared to the spontaneous scattering.

Yet the reader knows that the yellow 1S excitons in Cu_2O consist of the threefold quadrupole allowed orthoexcitons of ${}^3\Gamma_5^+$ symmetry split off by 12.12 meV to higher energy from the optically forbidden paraexciton of ${}^1\Gamma_2^+$ symmetry by isotropic exchange. As shown in the introduction (sec-

tion 2.2.4) in a magnetic field, the orthoexciton splits into the three states M=0, M=±1 whose energetic separation is determined by the magnetic field strength. k^2-dependent exchange interaction yields anisotropic masses for the three orthoexciton states. Exciting the highest state M=+1 resonantly at $\mathbf{k}_0$ leads to intra- and interband scattering with LA and TA phonons to the lower lying M=0 and M=-1 orthoexcitons. A small occupation created by spontaneous scattering occupation is the source for stimulated Brillouin scattering between the orthoexciton states. A detailed analysis of the kinematics is presented in this chapter showing that these scattering processes strongly depend on the applied magnetic field. Besides the prerequisite of energy and momentum conservation, the possibility for stimulated Brillouin scattering is additionally governed by selection rules and deformation potentials leading to a pronounced **k**-dependence. The analysis reveals the possibility to excite a state in the lowest orthoexciton subband with arbitrary k and in particular with $k = 0$ for three distinct field strengths. A pronounced asymmetric resonance dependence within a few μeV increases the relevant parameter space even more.

6.1 Scattering mechanism

Sound velocities in Cu_2O depend strongly on **k**-direction, i.e. the TA phonon is degenerate along $\mathbf{k} \parallel [001]$ and splits into a slow TA (STA) phonon and a fast TA (FTA) phonon along $[1\bar{1}0]$ (see Figure 2.2). Possible inter- and intraband scattering along $\mathbf{k} \parallel [1\bar{1}0]$ with STA and LA phonons within the orthoexciton subbands for excitation of the M=+1 orthoexciton is illustrated in Figure 6.1 for a field strength of 4 T in Voigt configuration. The red solid lines (TA phonon sound velocity $v_{STA} = 1.14 \cdot 10^3$ ms^{-1}) represent forward and backward scattering of the STA phonon, the blue solid lines (LA phonon sound velocity $v_{LA} = 4.60 \cdot 10^3$ ms^{-1}) forward and backward scattering of the LA phonon along $\mathbf{k} \parallel [1\bar{1}0]$.

The selection rules for these intra- and interband scattering processes can be derived from the exciton-acoustic phonon interaction Hamiltonian, which contains four terms H_1, H_3, H_4 and H_5 of ${}^1\Gamma_1^+$, ${}^3\Gamma_3^+$, ${}^3\Gamma_4^+$ and ${}^3\Gamma_5^+$ symmetry, respectively (section 2.2.2).

For STA phonons along $\mathbf{k} \parallel [1\bar{1}0]$, only $H_3 \neq 0$ and $H_4 \neq 0$, whereas for fast TA phonons (FTA), only $H_4 \neq 0$ and $H_5 \neq 0$. Calculation of the matrix elements $|\langle \mathbf{\Psi}_{\mathrm{O}}^{(M')} | H_i | \mathbf{\Psi}_{\mathrm{O}}^{(M)} \rangle|^2$ leads to selection rules for the acoustic phonons with the excited orthoexciton state $|\mathbf{\Psi}_{\mathrm{O}}^{(M)}\rangle$ (here M=+1) and the final orthoexciton state $|\mathbf{\Psi}_{\mathrm{O}}^{(M')}\rangle$ (M'=0,-1). They show that for STA phonons scattering is allowed only from M=+1 to the M=-1, whereas for the FTA

phonons only scattering to the M=0 state is possible. Comparing the scattering probabilities calculated from H_3 and H_5 shows that the probability for TA-phonons with ${}^2\Gamma_3^+$ symmetry is by an order of magnitude higher than for TA-phonons with ${}^3\Gamma_5^+$ symmetry. The spin-orbit interaction described by H_4 is much weaker and thus omitted. Therefore only STA phonon scattering from M=+1 to M=-1 is considered as sketched in Figure 6.1. In contrast the

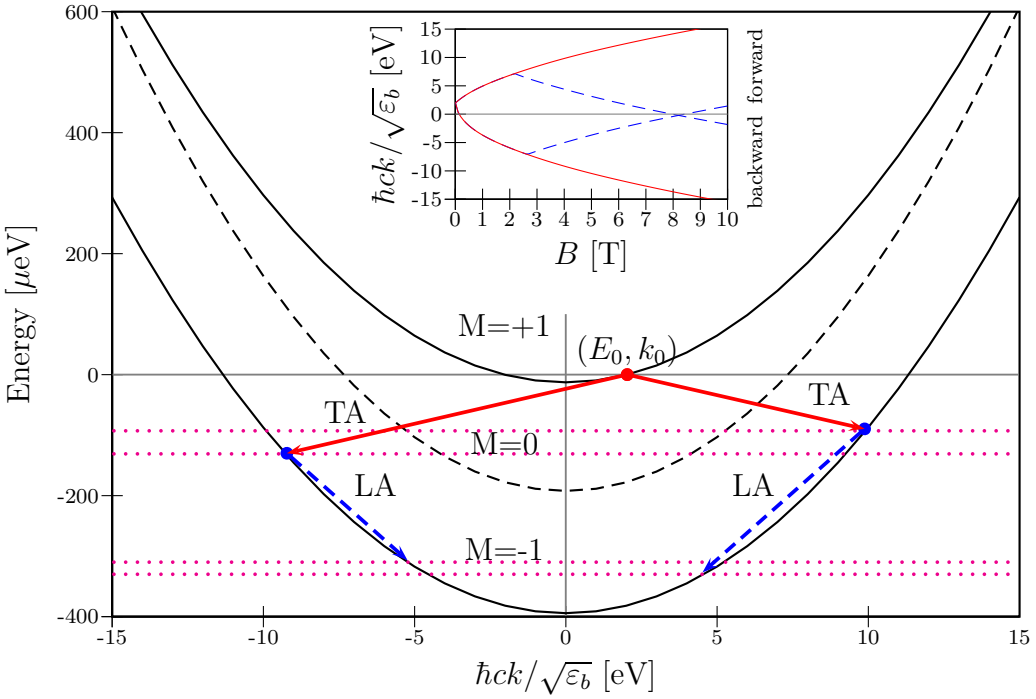

Figure 6.1: Inter- and intraband Brillouin-scattering within the orthoexciton parabolas for $\mathbf{k} \parallel [1\bar{1}0]$ and $B = 4$ T in Voigt configuration: upper parabola, M=+1 dispersion; dashed parabola, M=0 dispersion; lower parabola, M=-1 dispersion; solid red arrows, interband scattering of STA-phonons; dashed blue arrows, intraband scattering of LA phonons; $E = 0$ μeV corresponds to the resonance of the M=+1 orthoexciton at k_0. For the wavenumber $x = \hbar ck/\sqrt{\varepsilon_b}$ with $\varepsilon_b = 8.64$ is used. The magenta dotted lines indicate the measured energy of the Brillouin scattering lines. Inset: calculated wavenumber dependence of the scattering on the magnetic field; red solid lines, STA phonon interband scattering (M=+1 to M=-1); blue dashed lines, LA intraband scattering within M=-1.

interband scattering by TA phonons, LA phonon scattering is the dominating scattering process for intraband scattering due to a large ${}^1\Gamma_1^+$ contribution to the scattering probability. Intraband scattering of LA-phonons within the M=-1 orthoexciton starting from a state to which the TA-phonon scatters

from M=+1, is shown in Figure 6.1. For the different scattering processes the dependence of the final wave vector on the magnetic field strength is shown as an inset.

An overview of the selection rules for $\mathbf{k} \parallel [1\bar{1}0]$ in Voigt and Faraday configuration is shown in Tab. 6.1. The relevant symmetry contributions of the Hamiltonian and the corresponding matrix elements $|\langle \mathbf{\Psi}_{\mathrm{O}}^{(M')} | H_i | \mathbf{\Psi}_{\mathrm{O}}^{(M)} \rangle|^2$ are listed for LA, STA and FTA Brillouin scattering. Note that the selection rules depend also on the wavevector $\mathbf{k}$, which is not shown here. Additionally any dependence on the absolute value of the phonon wave vector q has been neglected since it's contribution is considered to be small.

6.2 Scattering along $\mathbf{k} \parallel [1\bar{1}0]$

With $\mathbf{k} \parallel [1\bar{1}0]$ and the magnetic field in Voigt configuration the M=±1 quadrupole oscillator strength is 1/2, whereas the M=0 can not be excited. Only the two excitable states have a non-zero matrix element for optical phonon emission. In the experiment a spot on the sample was selected that showed a narrow absorption line and the laser was tuned to the M=+1 resonance. The phonon assisted emission via ${}^3\Gamma_5^-$ and ${}^2\Gamma_3^-$ optical phonons was monitored by the CCD camera behind the double monochromator. The additional shift of the Brillouin resonances due to the optical phonons (10.58 meV for ${}^3\Gamma_5^-$ phonons, 13.45 meV for ${}^2\Gamma_3^-$ phonons) and the use of optical low pass filters (613 nm) allows an excellent suppression of scattered laser light. A tilted bandpass (611 nm) was used to suppress amplified spontaneous emission (ASE) of the laser.

Figure 6.2 and Figure 6.3 show the ${}^2\Gamma_3^-$ and ${}^3\Gamma_5^-$ phonon assisted emission of the orthoexciton, respectively. The zero-point of the energy scale is shifted to the Stokes-Raman-transition of the corresponding optical phonon.

Additionally to the Raman peak at $E = 0$ μeV, one observes Stokes and anti-Stokes lines due to inter- and intraband Brillouin scattering. The anti-Stokes lines around 150 μeV and 510 μeV (marked by arrows in Figure 6.2) can be attributed to TA phonon interband scattering and LA phonon intraband scattering, respectively. These lines show a very weak dependence on excitation intensity. On the Stokes-side of the spectrum one observes for low excitation intensities two Brillouin lines besides the Raman line. With increasing excitation intensity the emission intensity of these lines increases with respect to the Raman line. For high excitation intensities there is a strong nonlinear intensity increase of these Brillouin lines, and each of them splits into two narrow lines.

Due to the smaller width of the ${}^3\Gamma_5^-$ optical phonon emission ($\gamma_5 = 8$ μeV)

	Faraday			Voigt		
	M=-1	M=0	M=+1	M=-1	M=0	M=+1
M=-1	LA ($\Gamma_1^+;\Gamma_3^+;\Gamma_5^+$)	LA	LA ($\Gamma_3^+;\Gamma_5^+$)	LA ($\Gamma_1^+;\Gamma_3^+$)	LA	LA (Γ_5^+)
	(1.68; 0.07; 0.08)	(-)	(0.22; 0.08)	(1.68; 0.15)	(-)	(0.16)
	STA	STA ($\Gamma_3^+;\Gamma_4^+$)	STA	STA (Γ_4^+)	STA	STA (Γ_3^+)
	(-)	(0.31; 0.01)	(-)	(0.02)	(-)	(0.44)
	FTA	FTA ($\Gamma_4^+;\Gamma_5^+$)	FTA	FTA	FTA ($\Gamma_4^+;\Gamma_5^+$)	FTA
	(-)	(0.01; 0.11)	(-)	(-)	(0.01; 0.11)	(-)
M=0	LA	LA ($\Gamma_1^+;\Gamma_3^+;\Gamma_5^+$)	LA	LA	LA ($\Gamma_1^+;\Gamma_3^+$)	LA
	(-)	(1.68; 0.15; 0.16)	(-)	(-)	(1.68; 0.29)	(-)
	STA ($\Gamma_3^+\Gamma_4^+$)	STA	STA ($\Gamma_3^+;\Gamma_4^+$)	STA	STA	STA
	(0.31; 0.01)	(-)	(0.31; 0.01)	(-)	(-)	(-)
	FTA ($\Gamma_4^+;\Gamma_5^+$)	FTA	FTA ($\Gamma_4^+;\Gamma_5^+$)	FTA ($\Gamma_4^+;\Gamma_5^+$)	FTA	FTA ($\Gamma_4^+;\Gamma_5^+$)
	(0.01; 0.11)	(-)	(0.01; 0.11)	(0.01; 0.11)	(-)	(0.01; 0.11)
M=+1	LA ($\Gamma_3^+;\Gamma_3^+$)	LA	LA ($\Gamma_1^+;\Gamma_3^+;\Gamma_5^+$)	LA (Γ_5^+)	LA	LA ($\Gamma_1^+;\Gamma_3^+$)
	(0.22; 0.08)	(-)	(1.68; 0.07; 0.08)	(0.16)	(-)	(1.68; 0.15)
	STA	STA ($\Gamma_3^+;\Gamma_4^+$)	STA	STA (Γ_3^+)	STA	STA (Γ_4^+)
	(-)	(0.31; 0.01)	(-)	(0.44)	(-)	(0.02)
	FTA	FTA ($\Gamma_4^+;\Gamma_5^+$)	FTA	FTA	FTA ($\Gamma_4^+;\Gamma_5^+$)	FTA
	(-)	(0.01; 0.11)	(-)	(-)	(0.01; 0.11)	(-)

Table 6.1: Selection rules for Brillouin scattering within $M = 0, \pm 1$ orthoexciton for $\mathbf{k} \parallel [1\bar{1}0]$ in Faraday- ($B \parallel [1\bar{1}0]$) and Voigt-Configuration ($B \parallel [001]$). The relevant symmetry contributions of the Hamiltonian and the relative contribution of the corresponding matrix elements $|\langle \mathbf{\Psi}_{\mathrm{O}}^{(M')} | H_i | \mathbf{\Psi}_{\mathrm{O}}^{(M)} \rangle|^2$ are listed for LA, STA and FTA Brillouin scattering as numbers in parenthesis; (-) means not allowed, zero matrix element.

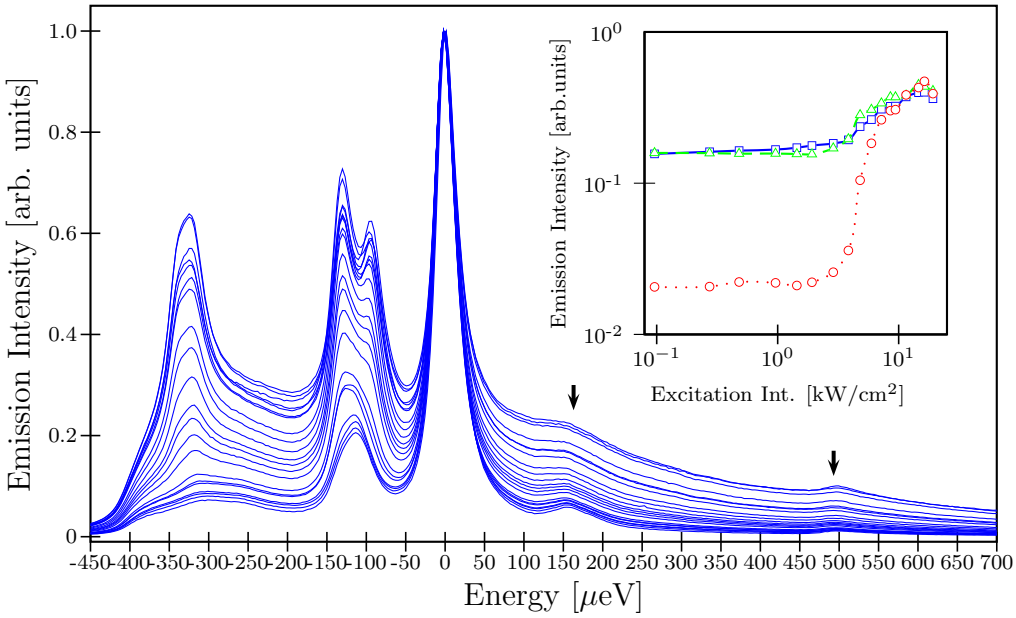

Figure 6.2: ${}^2\Gamma_3^-$ phonon assisted emission of orthoexcitons for different excitation intensities ($B = 4$ T in Voigt configuration). $E = 0$ μeV corresponds to the resonance of the M=+1 orthoexciton shifted to lower energy by the energy of the ${}^2\Gamma_3^-$ LO-phonon (13.45 meV). Inset: dependence of emission intensity on laser intensity; blue squares, TA forward scattering; green triangles, TA backward scattering; red empty dots, TA+LA scattering. Arrows mark anti-Stokes Brillouin scattering of LA phonons.

as compared to the width of the ${}^2\Gamma_3^-$ optical phonon emission ($\gamma_3 = 21$ meV, see section 4.2.2) these scattering processes and, in particular, the splitting of the energetically lower lying scattering lines, are resolved more clearly in the ${}^2\Gamma_5^-$ phonon assisted emission (note the different energy scales of Figure 6.2 and Figure 6.3).

A kinematical analysis shows that the first line at $E_{STA}^{+} = -92.9$ μeV (Figure 6.3) corresponds to forward, the second one at $E_{STA}^{-} = -131$ μeV to backward interband scattering along $\mathbf{k} \parallel [1\bar{1}0]$ with STA phonons between M=+1 and M=-1 orthoexcitons. The third and the fourth line at $E_{LA}^{-} = -310$ μeV and $E_{LA}^{+} = -330$ μeV can be identified as backward and forward intraband scattering of LA phonons within the M=-1 subband. The ${}^2\Gamma_3^-$data (Figure 6.2) show the same results, as far as the fine-structure can be resolved. The derivation of the formulas from energy and momentum conservation are given in Appendix B.

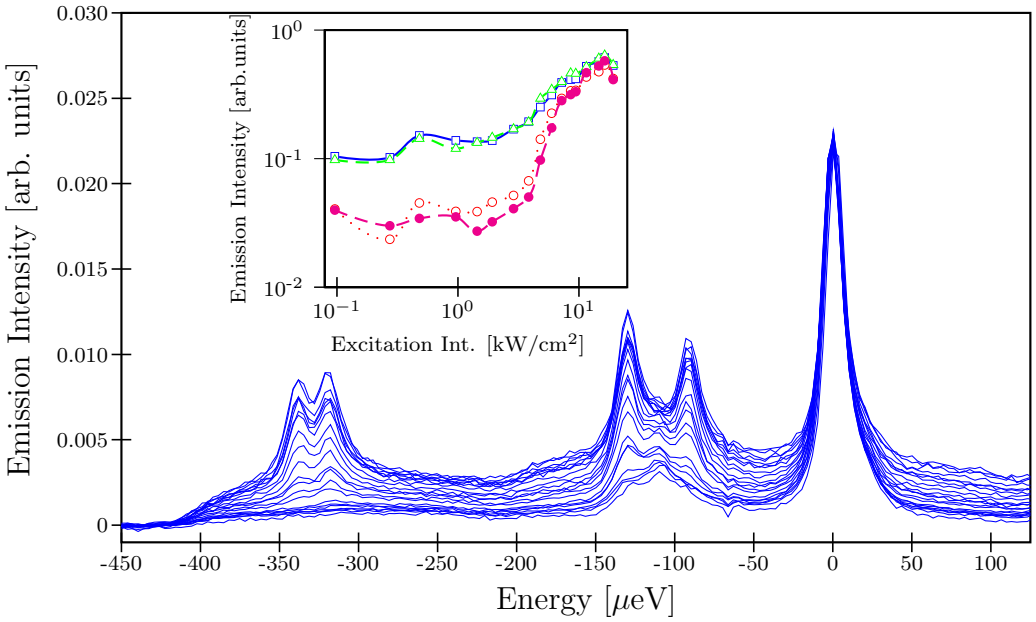

Figure 6.3: $^3\Gamma_5^-$ phonon assisted emission of orthoexcitons for different excitation intensities ($B = 4$ T in Voigt configuration). $E = 0$ μeV corresponds to the resonance of the M=+1 orthoexciton shifted to lower energy by the energy of the $^3\Gamma_5^-$ LO-phonon (10.58 meV). Note: The range of the energy scale is reduced by a factor of two in comparison to the one in Figure 6.2. Inset: dependence of emission intensity on laser intensity; blue squares, TA forward scattering; green triangles, TA backward scattering; red empty dots, TA+LA forward scattering; magenta solid dots, TA+LA backward scattering.

6.2.1 Intensity dependence

The intensity dependence of the Brillouin scattering as shown in the insets of Figure 6.2 and 6.3 shows a nonlinear increase of the Brillouin scattering peaks with excitation intensity indicating a stimulated character of the scattering processes. The stimulation starts at a threshold of about 2 kW/cm^2 and saturates above 16 kW/cm^2. This threshold-like behavior and the saturation for high excitation intensities are typical for stimulated Brillouin scattering [76].

For low excitation intensities Brillouin scattering takes place in **k**-directions determined by energy and momentum conservation leading to a "plateau" from $E^+_{TA/LA}$ up to $E^-_{TA/LA}$ in the phonon assisted emission. As soon as the stimulation threshold is reached the "plateau" splits into two peaks that can be attributed to forward and backward scattering. This can

be understood easily considering two waves: one for the phonon and one for the exciton. As the interference of two waves is maximized for parallel or antiparallel propagating waves, there is a preference for forward/backward stimulated scattering [77]. Since the LA phonon scattering processes do not simply copy the occupation generated by stimulated TA scattering but set in at higher excitation intensities, it is conclusive that the LA scattering process itself is stimulated with a slightly higher threshold. As the temperature of the exciton gas obtained from a fit of the spectra in Figure 6.2 is approximately the bath temperature (< 2 K), a possible increased occupation of acoustic phonons due to heating can be excluded. Though an increased occupation of acoustic phonons leads to a higher intensity of the Brillouin scattering lines, it does not give rise to a preferential scattering into forward and backward direction as stimulated Brillouin scattering does.

6.2.2 Magnetic field dependence

The dotted lines in Figure 6.1 represent the energetic positions $E_{STA}^{+/-}$ and $E_{LA}^{+/-}$ of the measured peaks that quantitatively match the inter- and intraband scattering processes discussed before. The positions of the lines depend strongly on the magnetic field as shown in Figure 6.4, since the splitting of the orthoexciton subbands increases linearly with the magnetic field. The solid lines represent the calculated kinematics for STA-interband scattering from M=+1 to M=-1, the dashed lines represent LA intraband scattering within the M=-1 orthoexciton. In Figure 6.4 one recognizes a threshold for LA intraband scattering at 2.25 T.

The sound velocities have been determined from the kinematical analysis (Figure 6.4) and agree well with data in the literature [21, 24, 25]. Especially the dependence of the TA scattering energies on the magnetic field is very sensitive to the TA sound velocity. This leads to small corrections to the elastic constants for low temperatures but is still consistent with the determination of the paraexciton mass in section 5.1 since it is within the stated errors. Moreover a slight change of the mass of approx. 1% does not have a noteable effect on the kinematical analysis.

With increasing field strength the stimulation gain decreases. The scattering processes at higher field strength involve acoustic phonons with higher energy since the splitting of the orthoexciton subbands increases with the magnetic field. These “high”-energy phonons, however, are only weakly occupied at low temperatures yielding a higher stimulation threshold.

As seen in the inset of Figure 6.1 the kinematics allows final scattering states in the lowest exciton subband with arbitrary wave vector k, which

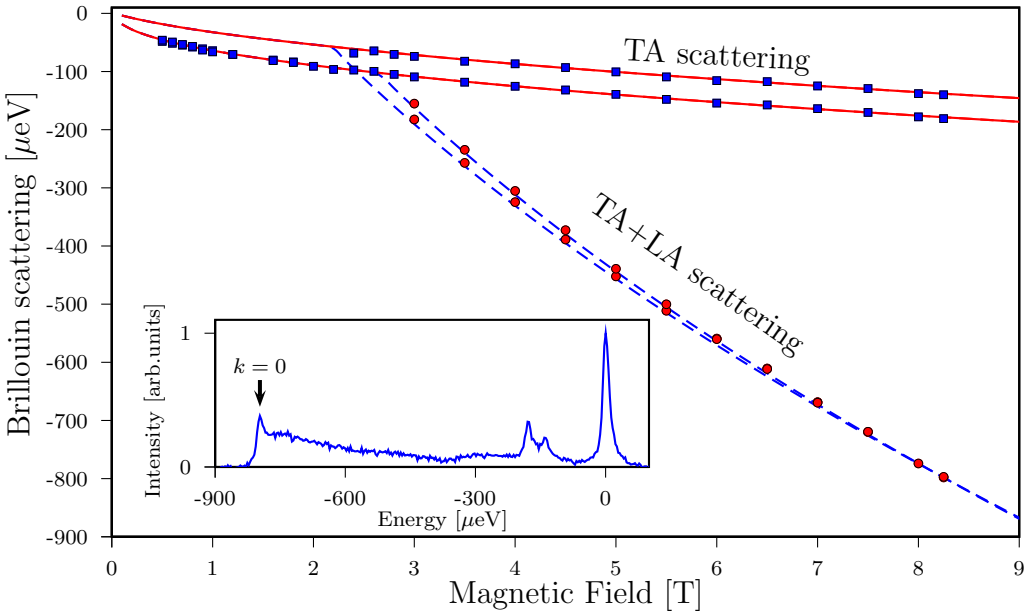

Figure 6.4: Energetic positions of Brillouin scattering lines. $E = 0$ μeV corresponds to the Raman transition; red solid lines, TA scattering; blue dashed lines, TA+LA scattering; blue squares, measured TA scattering; read dots, measured TA+LA scattering. Inset: ${}^3\Gamma_5^-$- phonon assisted emission at 8.25 T. Arrow marks TA+LA scattering to $k = 0$ within the M=-1 subband.

is achieved by simply tuning the magnetic field. For three distinct field strengths this final wave vector vanishes ($k = 0$): i) at $B \approx 8.25$ T and $B \approx 8.75$ T by two-phonon (STA/LA) forward and backward scattering, respectively (inset Figure 6.1, and ii) at ≈ 0.1 T by a one-phonon process (STA-backward scattering) The inset in Figure 6.4 shows an example of stimulated scattering at 8.25 T, where the wave vector of the final scattering state vanishes.

Figure 6.5 shows stimulated Brillouin scattering for $\mathbf{k} \parallel [1\bar{1}0]$ in Faraday configuration at $B = 6$ T. Although at first glance it looks similar to the previously shown scattering in Voigt configuration the underlying processes are different. The exciting laser was tuned to the M=0 resonance and Brillouin scattering was observed via STA phonons from the M=0 to the M=-1 orthoexciton. Considering exclusively STA interband scattering the same argument is valid as in case of Voigt configuration (see Tab. 6.1) thus justifying the use of the selection rules. Again, LA intraband scattering takes place within the M=-1 orthoexciton. The power dependence of the Brillouin scattering processes presented in the inset of Figure 6.5 shows a more pronounced rise and saturation than in the measurements in Voigt configuration

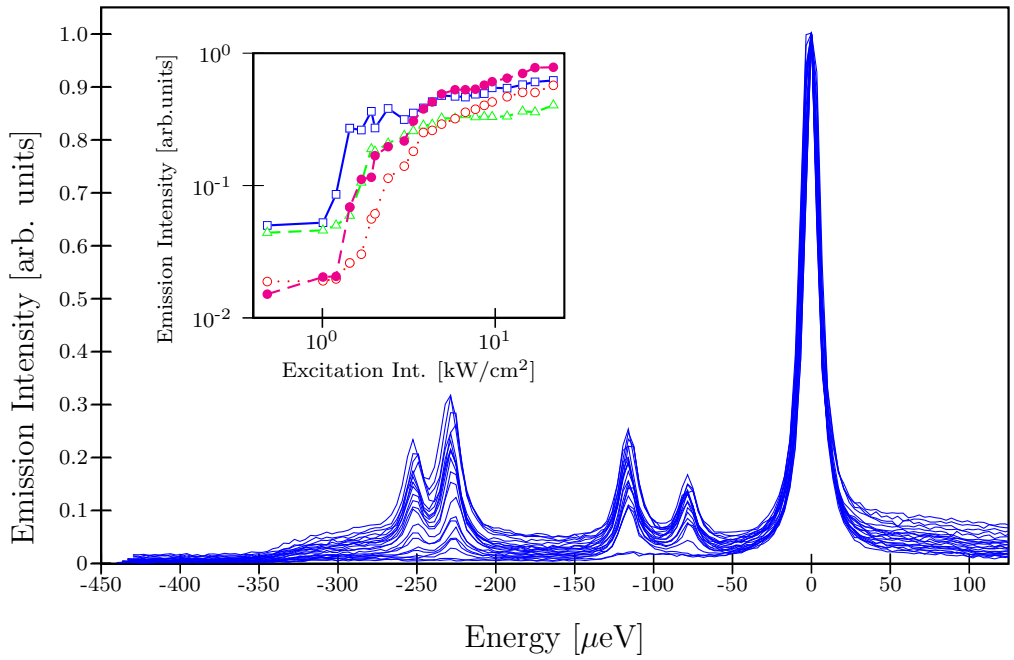

Figure 6.5: ${}^3\Gamma_5^-$ phonon assisted emission of orthoexcitons for different excitation intensities ($B = 6$ T in Faraday configuration). $E = 0$ μeV corresponds to the resonance of the M=0 orthoexciton shifted to lower energy by the energy of the ${}^3\Gamma_5^-$ LO-phonon (10.58 meV). Inset: dependence of emission intensity on laser intensity; blue squares, TA forward scattering; green triangles, TA backward scattering; red empty dots, TA+LA forward scattering; magenta solid dots, TA+LA backward scattering.

and spans over three orders of magnitude.

6.2.3 Resonance dependence

By tuning the laser through the orthoexciton resonance one observes a strong resonance dependence as presented in Figure 6.6 for $\mathbf{k} \parallel [1\bar{1}0]$ and $B = 4$ T in Voigt configuration. Shown are the stimulated Brillouin scattering intensities relative to the Raman transition, whose resonance dependence follows the absorption. While approaching the resonance from lower energies the stimulated Brillouin scattering intensity drops abruptly, particularly for the case of TA and subsequent LA scattering. Tuning the laser to higher energies the scattering intensities increase slowly again. Due to this strong asymmetric resonance dependence the highest Brillouin scattering intensities are observed by tuning the laser slightly off-resonant. A peculiarity can be observed, if the laser is tuned directly in resonance. In this case the stim-

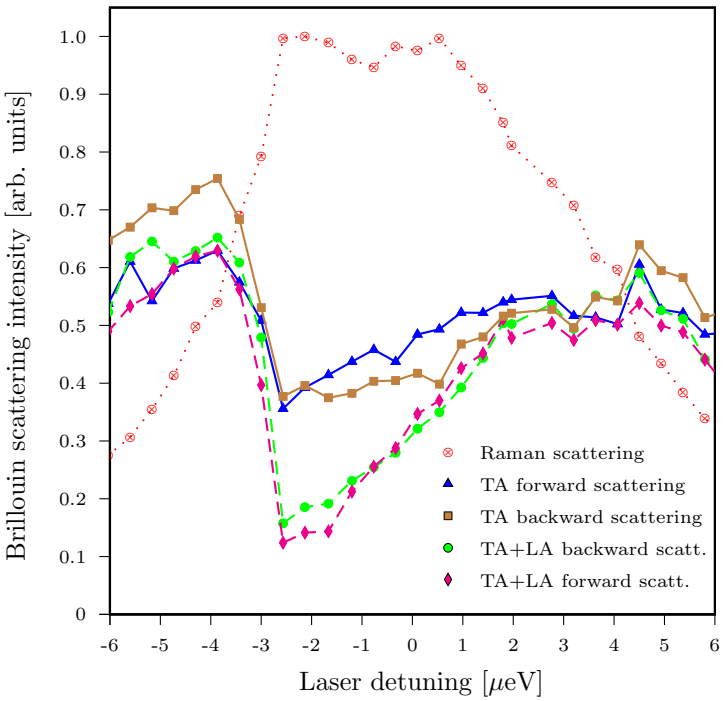

Figure 6.6: Resonance dependence of the Brillouin scattering lines as derived from the ${}^3\Gamma_5^-$ phonon assisted luminescence at $B = 4$ T in Voigt configuration.

ulation signal not just vanishes but decreases with increasing intensity with respect to the Raman. One could presume that the resonance dependence is connected to the polaritonic character of the orthoexciton. The wave vector dependence of the two polariton branches, however, is negligible and moreover fully symmetric around the resonance. Summarizing, one has to admit that the origin of this asymmetric resonance dependence is still unclear.

6.3 Scattering along other crystallographic directions

Stimulated Brillouin scattering was also observed in other crystallographic directions (e.g. $\mathbf{k} \parallel [112]$). The strength of the Brillouin scattering signal, however, varies from sample to sample, which does not allow to compare absolute scattering intensities.

For samples oriented along [001], however, it was not possible to observe any stimulated Brillouin scattering signal. Figure 6.7 presents two spectra measured on such a sample (H35) with $\mathbf{k} \parallel [001]$ for low and high excitation

intensity. The blue line shows the spectrum taken at low excitation inten-

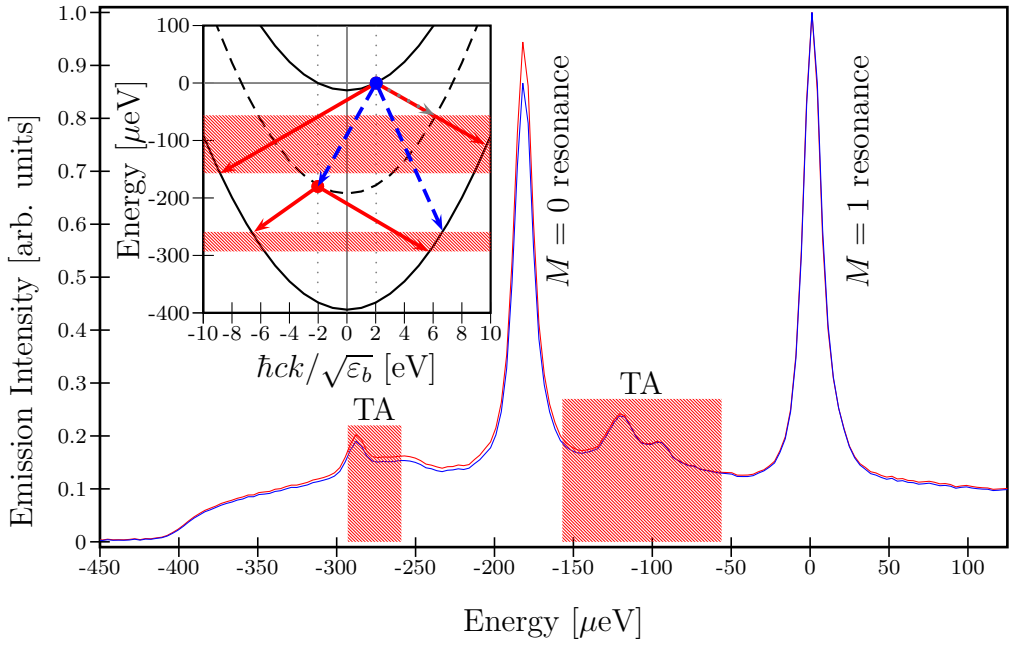

Figure 6.7: ${}^3\Gamma_5^-$ phonon assisted emission of orthoexcitons ($B = 4$ T in Voigt configuration, $\mathbf{k} \parallel [001]$) for two different excitation intensities (blue line, low intensity; red lines two orders of magnitude higher intensity). $E = 0$ μeV corresponds to the resonance of the M=+1 orthoexciton shifted to lower energy by the energy of the ${}^3\Gamma_5^-$ LO-phonon (10.58 meV). Inset: Intra- and interband Brillouin-scattering within the orthoexciton parabolas: upper parabola, M=+1 dispersion; dashed parabola, M=0 dispersion; lower parabola, M=-1 dispersion; solid red arrows, intraband scattering with STA-phonons; dashed blue arrows, interband scattering with LA phonons; $E = 0$ μeV corresponds to the resonance of the M=+1 orthoexciton. For the wavenumber $x = \hbar ck/\sqrt{\varepsilon_b}$ with $\varepsilon_b = 8.64$ is used.

sity while the red line shows the spectrum taken at two orders of magnitude higher excitation intensity. Apparently, at the expected scattering energies, indicated by the red hatchings, the signal remains constant with respect to the Raman peak. Nevertheless, at distinct scattering energies the signal is increased and certain scattering directions seem to be favored. However, these can not be assigned umambigiously to forward or backward scattering along [001]. As shown in the inset in Figure 6.7 the energy range marked by the red hatching from -56 μeV to 157 μeV is assigned to TA scattering (upper two red arrows) from the M=+1 to the two other orthoexciton states. The energy range marked by the red hatching from -259 μeV to 293 μeV can be

identified with TA scattering from the M=0 (lower red arrows). Exactly at the M=0 resonance a striking peak shows up, which is comparable in intensity with the intensity of the Raman peak[1]. An emission at this resonance becomes plausible if one considers interband LA scattering as indicated by the blue dashed lines in the inset in Figure 6.7. The underlying scattering process could be identified as LA phonon scattering from the M=1 resonance to the "backward" M=0 resonance. The process has to be mediated by off diagonal shear deformation ($^3\Gamma_5^-$) since the eigenstates are orthogonal and thus the contribution by compression ($^1\Gamma_1^-$) vanishes. In contrast to the experiments along $[1\bar{1}0]$, in [001] direction M±1 and M=0 quadrupole excitation and $^3\Gamma_5^-$ optical phonon emission from all three states are allowed. Due to the strong M=0 resonance enhancement, the LA scattering from M=+1 to M=0 becomes probable even though it is only mediated by shear strain.

6.4 The influence of phonon focusing

The occurrence of particularly favored scattering directions of acoustic phonons motivates the consideration of so called phonon focusing - the anisotropy in phonon flux[2].

In the general case the phonon wave vector $\mathbf{q}$ and the group velocity $\mathbf{v}_g$ are not collinear. The construction of the locus of the wave vector for a constant frequency leads to a "slowness surface" with the slowness vector $\mathbf{s} = \mathbf{q}/\omega$. The radial dimension of the slowness surface in a particular direction is inversely proportional to the phase velocity v in that direction:

$$s = |\mathbf{q}|/\omega = 1/v. \tag{6.1}$$

Since the group velocity $\mathbf{v}_g$ is the gradient of the constant frequency surface in $\mathbf{q}$-space, $\mathbf{v}_g = \nabla_k \omega(\mathbf{k})$, for a given wave vector $\mathbf{q}$, pointing from the origin to the surface, the group velocity $\mathbf{v}_g$ is always perpendicular to the surface at that point. This is indicated by the arrows in Figure 6.8 which shows cross sections of the slowness surfaces for Cu_2O in the (110) plane calculated with the phase velocities for LA, STA and FTA phonons (equation 2.4) . The phonon flux is parallel to the group velocity, and hence an isotropic distribution of $\mathbf{q}$ vectors is transformed into a distinctly anisotropic distribution of group velocities. Thus, phonon energy is focused or defocused depending on the sign of the curvature of the slowness surface. This is the basic idea

[1] Due to selection rules the M=0 resonance peak exceeds the Raman peak in the $^2\Gamma_3^-$ phonon assisted emission.

[2] A detailed review on phonon focusing and phonon imaging can be found in Ref. [78].

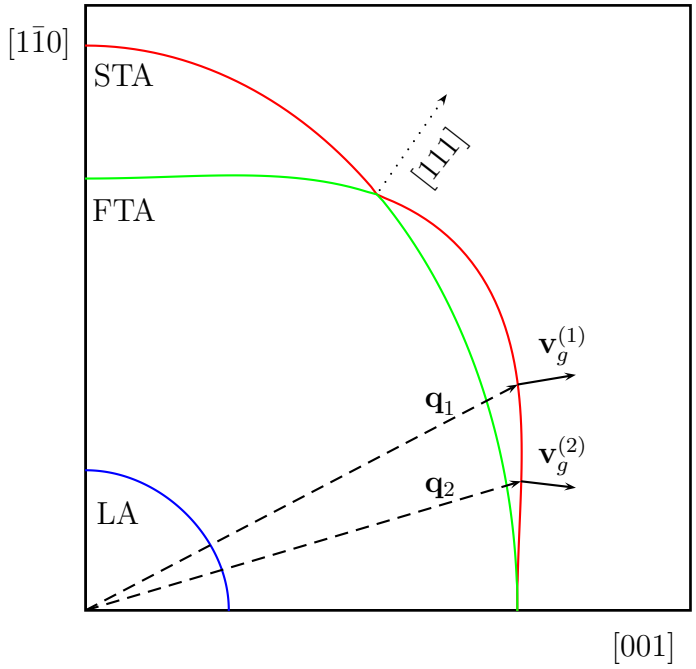

Figure 6.8: Intersections of slowness surfaces with the (001) plane for the three acoustic phonon modes in Cu_2O (blue line, LA phonon; green line, FTA phonon, red line, STA phonon). The dotted arrow marks the [111] direction with the conic contact of the FTA and STA slowness surface. Group velocities $\mathbf{v}_g$ are normal to the surface (solid arrows) and generally not collinear with $\mathbf{q}$ (dashed arrows).

of phonon focusing, which was first introduced in Ref. [79, 80] and further developed in Ref. [81].

Figure 6.8 shows that slowness surfaces for different modes may touch each other either tangentially or conically at a point. Along the [001] direction the STA and the FTA surface meet tangentially, along [111] (indicated by the dotted arrow) they meet conically in a point. Out of this point, in a cross section taken slightly out of the (110) plane, the two surfaces are separated. A striking peculiarity of this conical point is the cone centered around the [111] axis inside of which no FTA group velocities are present, an effect known as internal conical refraction [82, 83].

To quantify the angular variation of phonon flux, one can define an enhancement factor A, which is the variation of energy flux for a given propagation [81]

$$A = \left| \frac{\Delta\Omega_q}{\Delta\Omega_v} \right|,$$

where $\Delta\Omega_q$ is an infinitesimal solid angle of wave vector and $\Delta\Omega_v$ the corresponding solid angle of group velocities. The enhancement factor A relates the two dimensional q-space (θ_q, ϕ_q) to the two dimensional v_g-space (θ_v, ϕ_v) and the ratio of the elemental areas in these spaces corresponds to the Jacobian determinant[3] J of the functions f and g

$$d\Omega_v = d(\cos\theta_v)d\phi_v = Jd(\cos\theta_q)d\phi_q = J\Omega_q$$

with

$$J = \frac{\partial f}{\partial \cos\theta_q}\frac{\partial g}{\partial \phi_k} - \frac{\partial g}{\partial \cos\theta_q}\frac{\partial f}{\partial \phi_k}.$$

Hence the enhancement factor can be expressed by the inverse of the dimensionless Jacobian

$$A = \left|\frac{\Delta\Omega_q}{\Delta\Omega_v}\right| = \left|\frac{1}{J}\right|.$$

Three dimensional illustrations of the slowness surfaces and the enhancement factors for the three acoustic phonons are shown in Figure 6.9. The surfaces have been calculated in spherical coordinates, where the radius of the wave vector is given by the inverse of the phase velocity $1/v(\theta_q, \phi_q)$. The enhancement factors are shown as a false color representation and have been calculated according to Ref. [84] with the input parameters (θ_q, ϕ_q) and the elastic constants. The slowness surfaces can either have a convex, concave or saddle like Gaussian curvature. At the folds, where the sign of the curvature of the slowness surface changes from positive to negative (inflection points), sharp singularities in flux (caustics) occur, which can be observed for the STA and FTA phonons. Since the slowness surface of the LA phonon has a totally convex topology, no inflection points can be found. Note that there is almost no enhancement for the LA phonon ($A \approx 1$).

Tab 6.2 summarizes the calculated enhancement factors A and the phase velocity v for the three acoustic phonons in Cu_2O along [001] and [110].

	LA		**STA**		**FTA**	
	[001]	[110]	[001]	[110]	[001]	[110]
v [km/s]	4.50	4.60	1.49	1.14	1.49	1.49
A	0.70	1.10	62.6	0.16	62.6	3.75

Table 6.2: Calculated enhancement factors A_i and phase velocity v for the three acoustic phonons in Cu_2O along two major crystallographic directions.

[3]The Jacobian determinant is related to the Gaussian curvature K of the slowness surface by $J = K|q|^2\cos\xi$, where ξ is the angle between $\mathbf{q}$ and $\mathbf{v}_g$.

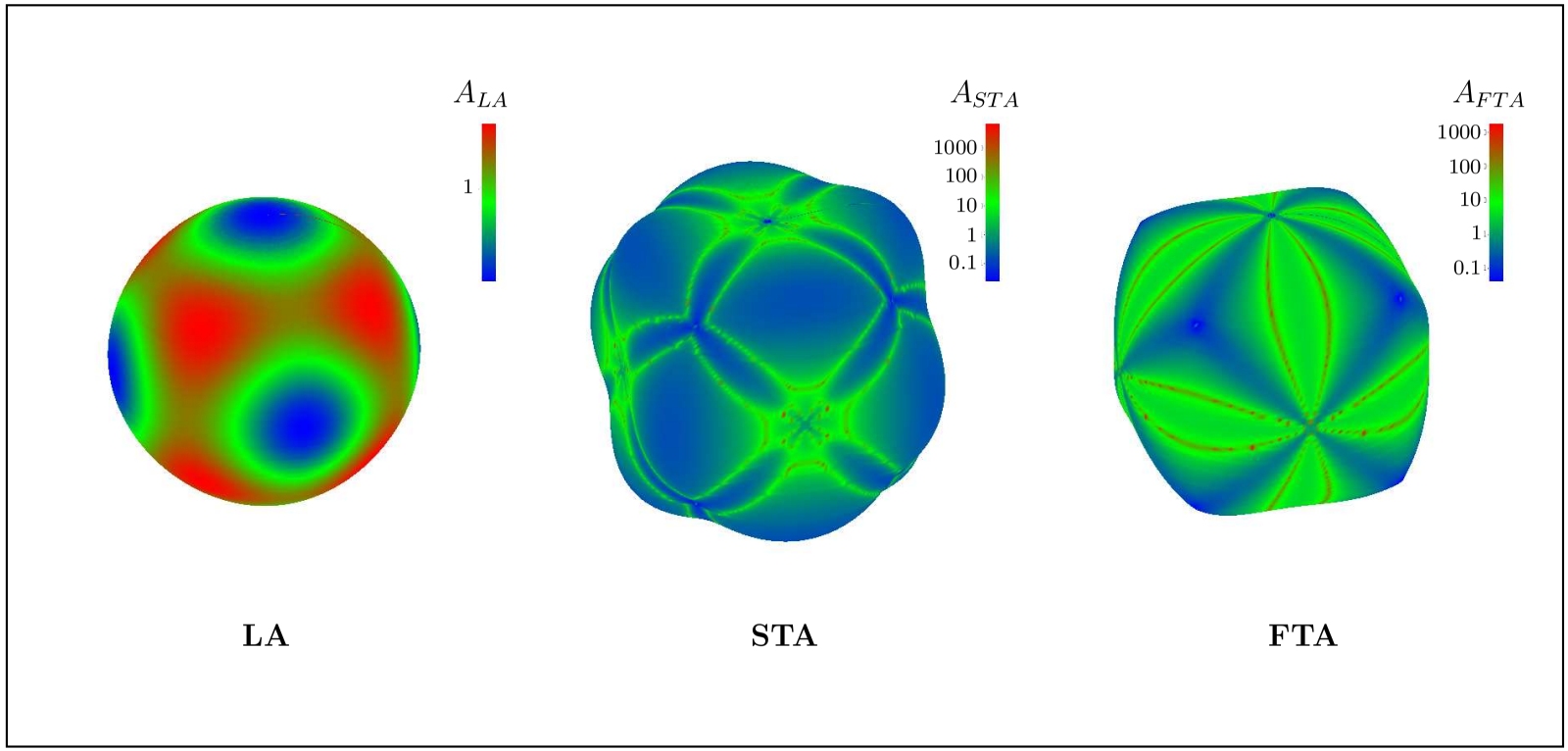

Figure 6.9: Slowness surfaces and phonon focusing enhancement of the LA, STA and FTA phonon. The surfaces are calculated in spherical coordinates, where the radius of the wave vector is $1/v(\theta_q, \phi_q)$. The false color represents the enhancement factor $A = 1/|J|$ as indicated by the corresponding legend. The reader should note that there is almost no enhancement for the LA phonon ($A \approx 1$).

In the context of transversal Brillouin scattering along [001] and [1$\bar{1}$0], Tab. 6.2 and especially the enhancement factor shown on the slowness surface in Figure 6.9 demonstrate that enhancement of the scattering lines along these directions due to phonon focusing can be considered as negligible. This is in particular the case for STA phonon scattering along [110], where the enhancement is actually < 1. For the STA phonon and for the FTA phonon the enhancement of phonon flux is increasing as soon as the direction $\mathbf{q}$ deviates slightly from [001] and approaches [110]. Yet, a correlation with the absence of a stimulation signal in the [001] measurments is not clear.

6.5 Summary

In conclusion, it has been shown that orthoexcitons in Cu_2O are ideal candidates to investigate stimulated Brillouin scattering within exciton subbands. It has been demonstrated that resonant excitation of 1S orthoexcitons in Cu_2O in a magnetic field leads to a fine-structure in the $^2\Gamma_3^-$ and $^3\Gamma_5^-$ optical phonon assisted emission which can be attributed to intra- and interband resonant Brillouin scattering (RBS). For increasing power a strong nonlinear enhancement of the intensity of this fine-structure can be observed. This intensity dependence of the Brillouin scattering lines exhibits a stimulation threshold for rather low excitation intensities. Beyond this threshold each line splits into two lines. The emission becomes highly directional parallel and antiparallel to the exciting laser. The energetic positions of the stimulated Brillouin scattering lines in Voigt- and Faraday configuration are confirmed by the use of a detailed kinematic model and an estimation of the relevant scattering probability with the help of deformation potential theory. A strong asymmetric resonance dependence is observed, although its origin is still unclear. Resonant Brillouin scattering with orthoexciton sublevels has been confirmed in different crystals and along different crystallographic directions. However, some samples do not show RBS scattering at all. It is tempting to speculate on "seeding" a state in the lowest orthoexciton with $k = 0$ and bypass the relaxation bottleneck [85]. However, condensation is unlikely since it is not feasible to create the critical density. The mayor obstacle is the short orthoexciton lifetime and the lifetime shortening effect with increasing exciton density [86].

The results presented in this chapter have been published in Ref. [66].

There are two possible outcomes: if the result confirms the hypothesis, then you've made a measurement. If the result is contrary to the hypothesis, then you've made a discovery.

Enrico Fermi (1901-1954)

7 Conclusions

The present studies contribute to the long search for a Bose-Einstein condensation of excitons in cuprous oxide with a deeper understanding of the 1S excitons in Cu_2O. It became apparent that only high resolution spectroscopy made the necessary detailed analysis of the 1S excitons possible.

Since optical phonon assisted emission to the 1S excitons is considered as a replica of the population of the corresponding exciton state, phonon assisted emission processes have been examined in detail considering their emission width, strength and feasibility to detect a Bose-Einstein condensation at $k = 0$. Except the ${}^3\Gamma_5^+$ phonon, all optical phonons in Cu_2O could be identified, and the ${}^3\Gamma_5^-$ phonon assisted luminescence turned out as most appropriate for this scenario due to its narrow emission width. Even though it has only a small emission intensity compared to the emission intensity of the wider ${}^2\Gamma_3^-$ optical phonon in a high magnetic field, the high resolution setup is by far sensitive enough to observe this phonon with an impressive statistics. Up to now, however, there is no evidence for a significant population at $k = 0$.

With the help of two phonon excitation spectroscopy the long lasting question about the paraexciton mass could be solved. A detailed, merely kinematical analysis yielded, besides an accurate value of the paraexciton mass, the refractive index and the kinetic paraexciton energy with only the longitudinal acoustic sound velocity as an input parameter. Furthermore it proved the importance of the central cell corrections.

The same technique allows the examination of the orthoexciton sublevels with the high resolution of the laser. Even though the spectra became rather complex due to k-space dependent scattering probabilities and selection rules, a limit for the previously unaccessible isotropic exchange parameter Δ_1 was derived.

Furthermore, this work shows that resonant Brillouin scattering within orthoexciton sublevels is highly directional, parallel and antiparallel to the exciting laser and exhibits a strong non-linear enhancement of the Brillouin

scattering intensity. A detailed kinematical analysis of the magnetic field depended scattering peaks allowed the precise determination of the STA sound velocity along [110]. A strong asymmetric resonance dependence is observed, but its origin is still unclear. Although the technique opens the possibility to stimulate orthoexcitons with arbitrary k values, seeding of $k = 0$ orthoexcitons to create a BEC is considered to be not feasible to reach the critical density.

The major obstacle on the way to condensation of the 1S excitons, and in particular the paraexcitons, seems to be the lifetime limiting two-body decay process that impedes the creation of a critical exciton density. Since the critical density is proportional to the temperature $T^{3/2}$, lowering the bath temperature may help. For this venture a ^{4}He cryostat is not suitable since even with powerfull pumps, the bath temperature won't drop below 1 K. A solution is offered by a ^{3}He cryostat or ^{3}He/^{4}He dilution cryostat with temperatures in the mK regime. First experiments with a ^{3}He insert for the cryostat, however, showed that the cooling power of ^{3}He is not sufficient at high excitation intensities to keep the exciton temperature below 1 K. Furthermore paraexciton beat experiments [44] revealed that the thermalization of the exciton gas with the phonon bath becomes inefficient at these low temperatures.

A promising attempt to reach the condensation of excitons seem to be a confinement of excitons in a potential trap since a confinement is anticipated to relax the conditions for a BEC significantly. In particular, a reduction of the critical density by several orders of magnitude and of the bimolecular exciton decay is expected. The confinement can be realized by a Hertzian contact [87], e.g. by the use of a lens with a small radius of curvature as a plunger that is pressed on the sample. The appearance of condensation of excitons in the trap can be proved either spatially, as proposed in [88], spectrally via phonon assisted emission, or by measuring the coherence of the relevant emission. An unambiguous proof of an excitonic BEC would include all three manifestations of a BEC. In this context it is tempting to resolve the discretized levels in the trap with the high resolution laser.

Despite the fact that numerous experiments and futile attempts to proof BEC of excitons in Cu_2O have been performed, Cu_2O is still a fascinating material. Though the Bose-Einstein condensation of excitons has not been proved unambiguously up to now, on the way to this objective interesting and surprising discoveries were made and are still expected.

Appendices

A Kinematical analysis I

The analysis of the kinematics of the paraexciton two-phonon excitation spectroscopy yields simple expressions for the paraexciton mass m_p, the kinetic energy E_0 at k_0 and the refractive index n as shown in the following paragraph. Starting from energy and momentum conservation

$$\begin{aligned} E_i = &\quad E_x(k_i) - E_x(k_0), &\quad i = 1,2 \\ k_i^2 = &\quad k_0^2 + q^2 + 2\,k_0\,q\cos\phi, &\quad \phi_1 = 0^\circ,\ \ \phi_2 = 180^\circ \end{aligned}$$

with the exciton dispersion $E_x(k) = \frac{\hbar^2 k^2}{2M_p m_0}$, the LA phonon wavevector q and the two states of the rise and the fall of the plateau (k_i, E_i) one obtains

$$\cancel{\frac{\hbar^2 k_0^2}{2M_p m_0}} + \frac{\hbar^2 q^2}{2M_p m_0} \pm \frac{\hbar^2 k_o q}{2M_p m_0} - \cancel{\frac{\hbar^2 k_0^2}{2M_p m_0}} = E_i, \qquad i = 1,2$$

where the (+)-sign corresponds to $i = 1$ and the (-)-sign to $i = 2$. The phonon wavevector can be expressed by $q = E_i/\hbar v_{LA}$ with the LA sound velocity $v_L A$, the wavevector of the kinetic energy is given by $k_0 = \sqrt{2M_p m_0 E_0}/\hbar$ and hence

$$\begin{aligned} \frac{E_i^2}{2M_p m_0 v_{LA}^2} \pm \frac{2\hbar^2(\sqrt{2M_p m_0 E_0}/\hbar)E_i}{2M_p m_0 v_{LA}} &= E_i \\ \Rightarrow \frac{E_i}{2M_p m_0 v_{LA}^2} \pm \frac{\hbar\sqrt{2M_p m_0 E_0}}{M_p m_0 v_{LA}} &= 1. \end{aligned} \qquad (1)$$

Adding up over i

$$\frac{1}{2M_p m_0 v_{LA}^2}(E_1 + E_2) = 2 \qquad (2)$$

and expanding with c^2 leads finally to the equation

$$\boxed{M_p = \frac{1}{4m_0 c^2}\left(\frac{c}{v_{LA}}\right)^2 (E_2 + E_1).}$$

From the difference of E_1 and E_2 in Eq. 1 one obtains

$$\begin{aligned} \frac{1}{2M_p m_0 v_{LA}^2}(E_1 - E_2) = &\quad -2\frac{\sqrt{2M_p m_0 E_0}}{M_p m_0 v_{LA}}, &(3)\\ \frac{1}{4v_{LA}^2}(E_2 - E_1)^2 = &\quad 4(2M_p m_0 E_0) &(4) \end{aligned}$$

and by dividing Eq. 4 by Eq. 2

$$\frac{2M_p m_0 v_{LA}^2}{4v_{LA}^2}\frac{(E_2-E_1)^2}{(E_2+E_1)^2} = \frac{4(2M_p m_0 E_0)}{2}$$

$$\boxed{E_0 = \frac{1}{8}\frac{(E_2-E_1)^2}{(E_2+E_1)}}$$

a simple expression for the kinetic energy E_0 of the paraexciton is derived depending only on the sum and the difference of the energy readings of E_1 and E_2.

From

$$\frac{\hbar^2 k_0^2}{2M_p m_0} = E_0 \text{ and } \frac{\hbar c k_0}{\sqrt{\varepsilon_b}} = E_P$$

with the paraexciton resonance energy E_p follows

$$\sqrt{2M_p m_0 E_0} = n\frac{E_p}{c}. \quad (5)$$

By inserting Eq. 5 into Eq. 4 one obtains for the refractive index

$$\boxed{n = \frac{1}{4E_P}\left(\frac{c}{v_{LA}}\right)(E_2-E_1).}$$

B Kinematical analysis II

This appendix shows the derivation of the Brillouin scattering energies for TA and subsequent LA scattering exemplarily from M=+1 to M=-1 and for the wavevector $\mathbf{k} \parallel [1\bar{1}0]$ and the magentic field $\mathbf{B} \parallel [001]$ (Voigt configuration).

Starting from the eigenvalue equation

$$H(\mathbf{k},\mathbf{B})|\Psi_{\mathrm{O}}\rangle = E_{\mathrm{O}}^{(M)}(\mathbf{k},\mathbf{B})|\Psi_{\mathrm{O}}\rangle$$

with the Hamiltonian H including the k^2-dependent exchange interaction J_1,J_3,J_5,J_Q, and Zeeman pertubation H_B yields the dispersion for the three orthoexciton states. From a parabolic fit of the dispersion one obtains the slope η_B in μeV/(eV)^2 of the M=-1 parabola (red line in Fig. 1) and the energetic separation δ_B of the M=+1 at $k = k_0$ and M=-1 at $k = 0$ orthoexcitons (blue line in Fig. 1). For convenience the the TA phonon energy $E_{TA} = \tilde{v}_{TA}(x - x_0)$ can be expressed with the dimensionless sound velocity $\tilde{v}_{TA} = \sqrt{\varepsilon_b}c^{-1}v_{TA} \cdot 10^6$ and the wavevector $x = \hbar ck/\sqrt{\varepsilon_B}$ in eV. The intersection of the phonon line with the exciton dispersion

$$\mp\tilde{v}_{TA}(x - x_0) = \eta_B x^2 + \delta_B$$

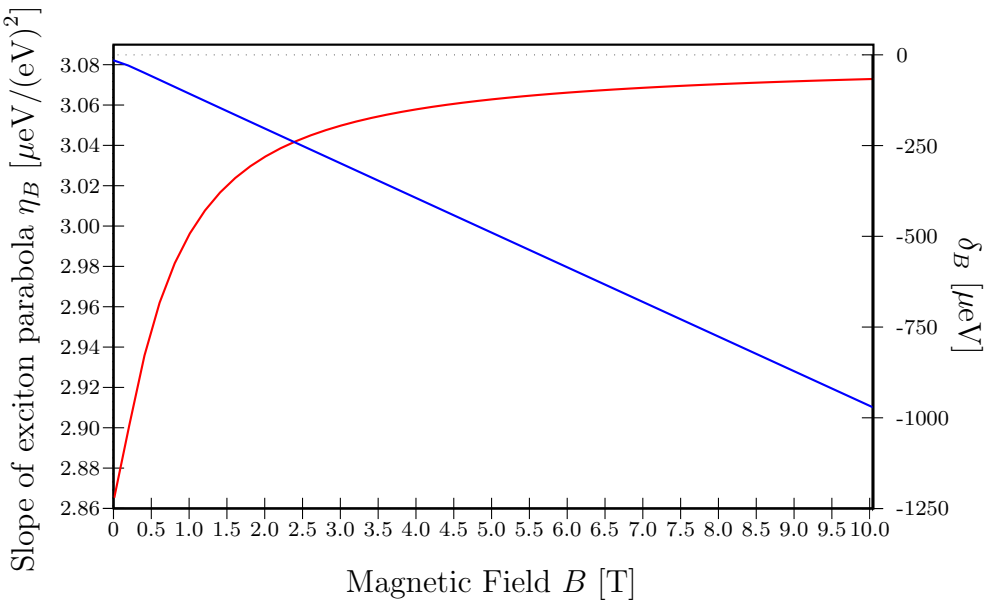

Figure 1: Magnetic field dependence of the slope of the exciton parabola η_B (M=-1) in μeV/(eV)^2 (red line) and the energy separation $\delta(B)$ of the M=+1 at $k = k_0$ and M=-1 at $k = 0$ orthoexciton states (blue line) for $\mathbf{k} \parallel [1\bar{1}0]$, $\mathbf{B} \parallel [001]$.

describes the TA phonon scattering for x_0 on the M=+1 state ($-$ sign corresponds to forward (fw), the $+$ sign backward (bw) scattering) to exciton wavevectors on the M=-1 parabola which are given by the solution of the quadratic equation

$$\boxed{x_{TA}^{(fw/bw)} = \mp\frac{\tilde{v}_{TA}}{2\eta_B} \pm \sqrt{\frac{\tilde{v}_{TA}^2}{4\eta_B^2} \pm \frac{1}{\eta_B}[\tilde{v}_{TA}x_0 \pm \delta_B]}.}$$

Analogous, the intersections of the LA phonon line starting from the derived TA scattering energy and wavevector within the $M = -1$ exciton parabola

$$\pm\tilde{v}_{TA}(x_{TA} - x_0) \mp \tilde{v}_{LA}(x_0) = \eta_B x^2 - \delta_B$$

yields the exciton wavevector in which the TA phonon scatters

$$\boxed{x_{LA}^{(fw/bw)} = \mp\frac{\tilde{v}_{LA}}{2\eta_B} \pm \sqrt{\frac{\tilde{v}_{LA}^2}{4\eta_B^2} \pm \frac{1}{\eta_B}[\tilde{v}_{TA}(x_{TA}^{bw/fw} - x_0) + \tilde{v}_{LA}x_{TA}^{bw/fw} \mp \delta_B]}.}$$

Finally the scattering energies are simply given by

$$\boxed{E_{TA/LA}^{fw/bw} = \eta_B x_{TA/LA}^{fw/bw}.}$$

Bibliography

[1] A. Einstein, *Quantentheorie des einatomigen idealen Gases*, Sitzungsber. Kgl. Preuss. Akad. Wiss. **1924**, 261 (1924).

[2] M. H. Anderson, J. R. Ensher, M. R. Matthews, C. E. Wieman, and E. A. Cornell, *Observation of Bose-Einstein condensation in a dilute atomic vapor*, Science **269**, 198 (1995).

[3] K. B. Davis, M. O. Mewes, M. R. Andrews, N. J. van Druten, D. S. Durfee, D. M. Kurn, and W. Ketterle, *Bose-Einstein condensation in a gas of sodium atoms*, Phys. Rev. Lett. **75**, 3969 (1995).

[4] T. Radu, H. Wilhelm, V. Yushankhai, D. Kovrizhin, R. Coldea, Z. Tylczynski, T. Lühmann, and F. Steglich, *Bose-Einstein condensation of magnons in* Cs_2CuCl_4, Phys. Rev. Lett. **95**, 127202 (2005).

[5] D. W. Snoke, *Spontaneous Bose coherence of excitons and polaritons*, Science **298**, 1368 (2002).

[6] J. Kasprzak, M. Richard, S. Kundermann, A. Baas, P. Jeambrun, J. M. J. Keeling, F. M. Marchetti, M. H. Szymanska, R. André, J. L. Staehli, V. Savona, P. B. Littlewood, B. Deveaud, and L. S. Dang, *Bose-Einstein condensation of exciton polaritons*, Nature **443**, 409 (2006).

[7] R. Balili, V. Hartwell, D. W. Snoke, L. Pfeiffer, and K. West, *Bose-Einstein condensation of microcavity polaritons in a trap*, Science **316**, 1007 (2007).

[8] M. H. Szymańska, J. Keeling, and P. B. Littlewood, *Nonequilibrium quantum condensation in an incoherently pumped dissipative system*, Phys. Rev. Lett. **96**, 230602 (2006).

[9] J. M. Blatt, K. W. Böer, and W. Brandt, *Bose-Einstein condensation of excitons*, Phys. Rev. **126**, 1691 (1962).

[10] F. Richter, D. Semkat, D. Kremp, and K. Henneberger, *Ionization equilibrium and Mott transition in an excited semiconductor, phase diagram*, phys. stat. sol. (c) **6**, 532 (2009).

[11] M. Hayashi and K. Katsuki, *Absorption spectrum of cuprous oxide*, J. Phys. Soc. Jpn. **5**, 381 (1950).

[12] M. Hayashi and K. Katsuki, *Hydrogen-like absorption spectrum of cuprous oxide*, J. Phys. Soc. Jpn. **7**, 599 (1952).

[13] E. F. Gross and A. Karryev, *Optical spectrum of excitons*, Dokl. Akad. Nauk. SSSR **84**, 471 (1952).

[14] G. Dasbach, D. Fröhlich, H. Stolz, R. Klieber, D. Suter, and M. Bayer, *Wave-vector-dependent exciton exchange interaction*, Phys. Rev. Lett. **91**, 107401 (2003).

[15] G. Dasbach, D. Fröhlich, R. Klieber, D. Suter, M. Bayer, and H. Stolz, *Wave-vector-dependent exchange interaction and its relevance for the effective exciton mass in Cu_2O*, Phys. Rev. B **70**, 045206 (2004).

[16] J. P. Wolfe, J. L. Lin, and D. W. Snoke, *Bose-Einstein condensation of a nearly ideal gas: excitons in Cu_2O*, chap. 13, p. 281, Cambridge University Press, Cambridge, UK (1995).

[17] T. Goto, M. Y. Shen, S. Koyama, and T. Yokouchi, *Bose-Einstein statistics of orthoexcitons generated by two-photon resonant absorption in cuprous oxide*, Phys. Rev. B **55**, 7609 (1997).

[18] M. Y. Shen, T. Yokouchi, S. Koyama, and T. Goto, *Dynamics associated with Bose-Einstein statistics of orthoexcitons generated by resonant excitations in cuprous oxide*, Phys. Rev. B **56**, 13066 (1997).

[19] J. I. Jang and J. P. Wolfe, *Auger recombination and biexcitons in Cu_2O: a case for dark excitonic matter*, Physical Review B **74**, 045211 (2006).

[20] D. Fröehlich, G. Dasbach, G. B. H. von Högersthal, M. Bayer, R. Klieber, D. Suter, and H. Stolz, *High resolution spectroscopy of yellow 1S excitons in Cu_2O*, Solid State Commun. **134**, 139 (2005).

[21] J. Brandt, D. Fröhlich, C. Sandfort, M. Bayer, H. Stolz, and N. Naka, *Ultranarrow optical absorption and two-phonon excitation spectroscopy of Cu_2O paraexcitons in a high magnetic field*, Phys. Rev. Lett. **99**, 217403 (2007).

[22] S. Mani, J. Jang, J. Ketterson, and H. Park, *High-quality Cu_2O crystals with various morphologies grown by thermal oxidation*, Journal of Crystal Growth **311**, 3549 (2009).

[23] A. Goltztené and C. Schwab, *Landolt-Börnstein*, vol. 17e, chap. Physics of non-tetrahedrally bonded elements and binary compounds I, p. 144, Springer, Berlin (1983).

[24] J. Berger, *Comportement thermoelastique de monocristaux de Cu_2O*, Solid State Commun. **26**, 403 (1978).

[25] J. Hallberg and R. C. Hanson, *The elastic constants of cuprous oxide*, phys. stat. sol. **42**, 305 (1970).

[26] G. K. White, *Thermal expansion of cuprous oxide at low temperatures*, J. Phys. C **11**, 2171 (1978).

[27] M. M. Beg and S. M. Shapiro, *Study of phonon dispersion relations in cuprous oxide by inelastic neutron scattering*, Phys. Rev. B **13**, 1728 (1976).

[28] S. Nikitine, J. B. Grund, and M. Sieskind, *Etude spectrophotométrique de la série jaune de Cu_2O aux basses températures*, J. Phys. Chem. Solids **17**, 292 (1961).

[29] H. Solache-Carranco, G. Juárez-Díaz, A. Esparza-García, M. Briseño-García, M. Galván-Arellano, J. Martínez-Juárez, G. Romero-Paredes, and R. Peña-Sierra, *Photoluminescence and X-ray diffraction studies on Cu_2O*, J. Luminescence **129**, 1483 (2009).

[30] J. B. Grun, M. Sieskind, and S. Nikitine, *Détermination de l'intensité d'oscillateur des raies de la série verte de Cu_2O aux basses températures*, J. Phys. Radium **22**, 176 (1961).

[31] A. Daunois, J. L. Deiss, and B. Meyer, *Étude spectrophotométrique de l'absorption bleue et violette de Cu_2O*, J. Phys. (Paris) **27**, 142 (1966).

[32] E. F. Gross, A. G. Zhilich, B. P. Zakharchenya, and A. V. Varfalomeew, *Magnetooptical investigation of quadrupole exciton transitions in a Cu_2O crystal*, Sov. Phys. Solid State **3**, 1048 (1961).

[33] S. Nikitine, J. B. Grun, and M. Certier, *Etude de l'intensité d'oscillateur de la raie d'absorption quadrupolaire $n = 1$ de la sèrie jaune de Cu_2O à 4,2°K*, Phys. Kondens. Mater. **1**, 214 (1963).

[34] D. Fröhlich, R. Kenklies, C. Uihlein, and C. Schwab, *Assignment of the even-parity excitons in Cu_2O*, Phys. Rev. Lett. **43**, 1260 (1979).

[35] C. Uihlein, D. Fröhlich, and R. Kenklies, *Investigation of exciton fine structure in Cu_2O*, Phys. Rev. B **23**, 2731 (1981).

[36] T. Tayagaki, A. Mysyrowicz, and M. Kuwata-Gonokami, *The yellow excitonic series of Cu_2O revisited by Lyman spectroscopy*, J. Phys. Soc. Jpn. **74**, 1423 (2005).

[37] G. M. Kavoulakis, Y. C. Chang, and G. Baym, *Fine structure of excitons in Cu_2O*, Phys. Rev. B **55**, 7593 (1997).

[38] V. T. Agekyan, *Spectroscopic properties of semiconductor crystals with direct forbidden energy-gap*, phys. stat. sol. (a) **43**, 11 (1977).

[39] G. Baldassarri Höger von Högersthal, G. Dasbach, D. Fröhlich, M. Kulka, H. Stolz, and M. Bayer, *Dynamic band gap shifts and magneto absorption in Cu_2O*, J. Luminescence **112**, 25 (2005).

[40] D. Fröhlich, J. Brandt, C. Sandfort, M. Bayer, and H. Stolz, *High resolution spetroscopy of excitons in Cu_2O*, phys. stat. sol. (b) **243**, 2367 (2006).

[41] D. Fröhlich, A. Kulik, B. Uebbing, A. Mysyrowicz, V. Langer, H. Stolz, and W. von der Osten, *Coherent propagation and quantum beats of quadrupole polaritons in Cu_2O*, Phys. Rev. Lett. **67**, 2343 (1991).

[42] D. Fröhlich, A. Kulik, B. Uebbing, V. Langer, H. Stolz, and W. von der Osten, *Propagation beats of quadrupole polaritons in Cu_2O*, phys. stat. sol. (b) **173**, 31 (1992).

[43] J. Brandt, D. Fröhlich, C. Sandfort, M. Bayer, and H. Stolz, *Paraexciton polariton propagation beats in cuprous oxide*, phys. stat. sol. (c) **6**, 556 (2009).

[44] J. Brandt, P. Felbier, D. Fröhlich, C. Sandfort, M. Bayer, and H. Stolz, *Temperature dependence of homogeneous broadening of the 1S-paraexciton in Cu_2O*, Phys. Rev. B **81**, 155214 (2009).

[45] G. E. Pikus and G. L. Bir, *Effect of deformation on the hole energy spectrum of germanium and silicon*, Sov. Phys. Solid State **1**, 1502 (1959).

[46] K. Reimann and K. Syassen, *Raman scattering and photoluminescence in Cu_2O under hydrostatic pressure*, Phys. Rev. B **39**, 11113 (1989).

[47] R. G. Waters, F. H. Pollak, R. H. Bruce, and H. Z. Cummins, *Effects of uniaxial stress on excitons in Cu_2O*, Phys. Rev. B **21**, 1665 (1980).

[48] H. R. Trebin, H. Z. Cummins, and J. L. Birman, *Excitons in cuprous oxide under uniaxial stress*, Phys. Rev. B **23**, 597 (1981).

[49] J. I. Jang, K. E. O'Hara, and J. P. W. And, *Spin-exchange kinetics of excitons in Cu_2O: transverse acoustic phonon mechanism*, Phys. Rev. B **70**, 195205 (2004).

[50] J. I. Jang and J. P. Wolfe, *Relaxation of stress-split orthoexcitons in Cu_2O*, Phys. Rev. B **73**, 075207 (2006).

[51] G. Dasbach, *Spectroscopy of polaritonic excitations in semiconductors*, Ph.D. thesis, Dortmund (2003).

[52] D. P. Trauernicht, J. P. Wolfe, and A. Mysyrowicz, *Thermodynamics of strain-confined paraexcitons in Cu_2O*, Phys. Rev. B **34**, 2561 (1986).

[53] N. Naka and N. Nagasawa, *Two-photon diagnostics of stress-induced exciton traps and loading of 1S-yellow excitons in Cu_2O*, Phys. Rev. B **65**, 075209 (2002).

[54] E. Hanamura and H. Haug, *Condensation effects of excitons*, Phys. Rep. **33**, 209 (1977).

[55] G. Baldassarri Höger von Högersthal, D. Fröhlich, M. Kulka, T. Auer, M. Bayer, and H. Stolz, *Acoustic and optical phonon scattering of the 1S yellow orthoexciton in Cu_2O*, Phys. Rev. B **73**, 035202 (2006).

[56] Y. Petroff, P. Y. Yu, and Y. R. Shen, *Study of photoluminescence in Cu_2O*, Phys. Rev. B **12**, 2488 (1975).

[57] A. Z. Genack, H. Z. Cummins, M. A. Washington, and A. Compaan, *Quadrupole-dipole Raman scattering at the 1S yellow exciton in Cu_2O*, Phys. Rev. B **12**, 2478 (1975).

[58] D. Fishman, C. Faugeras, M. Potemski, A. Revcolevschi, and P. H. M. van Loosdrecht, *Magneto-optical readout of dark exciton distribution in cuprous oxide*, Phys. Rev. B **80**, 045208 (2009).

[59] A. Z. Genack, H. Z. Cummins, M. A. Washington, and A. Compaan, *Quadrupole-dipole Raman scattering at the 1S yellow exciton in Cu_2O*, Phys. Rev. B **12**, 2478 (1975).

[60] G. F. Koster, J. O. Dimmock, R. G. Wheeler, and H. Statz, *Properties of the thirty-two point groups*, M.I.T. Press, Cambridge, Massachusetts (1963).

[61] D. W. Snoke, D. Braun, and M. Cardona, *Carrier thermaization in Cu_2O: phonon emission by excitons*, Phys. Rev. B **44**, 2991 (1991).

[62] P. D. Bloch and C. Schwab, *Direct evidence for phonon-assisted transitions to the 1S paraexciton level of the yellow exciton series in Cu_2O*, Phys. Rev. Lett. **41**, 514 (1978).

[63] R. J. Elliot, *Intensity of optical absorption by excitons*, Phys. Rev. **108**, 1384 (1957).

[64] J. P. Dahl and A. C. Switendick, *Energy bands in cuprous oxide*, J. Phys. Chem. Solids **27**, 931 (1966).

[65] D. Hulin, A. Mysyrowicz, and C. B. a la Guillaume a la Guillaume a la Guillaume a la Guillaume, *Evidence for Bose-Einstein statistics in an exciton gas*, Phys. Rev. Lett **45**, 1970 (1980).

[66] C. Sandfort, J. Brandt, D. Fröhlich, M. Bayer, and H. Stolz, *Resonant phonon scattering of paraexcitons in Cu_2O*, Phys. Rev. B **78**, 045201 (2008).

[67] J. W. Hodby, T. E. Jenkins, C. Schwab, H. Tamura, and D. Trivich, *Cyclotron resonance of electrons and of holes in cuprous oxide, Cu_2O*, J. Phys. C **9**, 1429 (1976).

[68] N. Caswell, J. S. Weiner, and P. Y. Yu, *A study of non-thermalized luminescence spectra: the case of Cu_2O*, Solid State Commun. **40**, 843 (1981).

[69] P. Y. Yu and Y. R. Shen, *Study of dispersive Raman modes in Cu_2O by resonant Raman scattering*, Phys. Rev. Lett. **32**, 939 (1974).

[70] M. Jörger, T. Fleck, C. Klingshirn, and R. von Baltz, *Midinfrared properties of cuprous oxide: high-order lattice vibrations and intraexcitonic transitions of the 1S paraexciton*, Phys. Rev. B **71**, 235210 (2005).

[71] M. Kuwata-Gonokami, M. Kubouchi, R. Shimano, and A. Mysyrowicz, *Time-resolved excitonic Lyman spectroscopy of Cu_2O*, J. Phys. Soc. Jpn. **73**, 1065 (2004).

[72] K. E. O'Hara, *Relaxation kinetics of excitons in cuprous oxide*, Ph.D. thesis, University of Illinois (1999).

[73] G. Dasbach, D. Fröhlich, H. Stolz, R. Klieber, D. Suter, and M. Bayer, *Anisotropic effective exciton mass in Cu_2O*, phys. stat. sol. (c) **2**, 886 (2005).

[74] R. G. Ulbrich and C. Weisbuch, *Resonant Brillouin scattering of excitonic polaritons in gallium arsenide*, Phys. Rev. Lett. **38**, 865 (1977).

[75] E. S. Koteles and G. Winterling, *Resonant scattering of exciton polaritons by LO and acoustic phonons*, Phys. Rev. B **20**, 628 (1979).

[76] M. Sparks, *Stimulated Raman and Brillouin scattering: parametric-instability explanation of anomalies*, Phys. Rev. Lett. **32**, 450 (1974).

[77] Y. R. Shen and N. Bloembergen, *Theory of stimulated Brillouin and Raman scattering*, Phys. Rev. **137**, A1787 (1965).

[78] J. P. Wolfe, *Imaging phonons*, Cambridge University Press, Cambridge, UK (1998).

[79] B. Taylor, H. J. Maris, and C. Elbaum, *Phonon focusing in solids*, Phys. Rev. Lett. **23**, 416 (1969).

[80] B. Taylor, H. J. Maris, and C. Elbaum, *Focusing of phonons in crystalline solids due to elastic anisotropy*, Phys. Rev. B **3**, 1462 (1971).

[81] H. J. Maris, *Enhancement of heat pulses in crystals due to elastic anisotropy*, J. Acoust. Soc. Am. **50**, 812 (1971).

[82] A. G. Every, *Ballistic phonons and the shape of the ray surface in cubic crystals*, Phys. Rev. B **24**, 3456 (1981).

[83] D. C. Hurley and J. P. Wolfe, *Phonon focusing in cubic crystals*, Phys. Rev. B **32**, 2568 (1985).

[84] G. A. Northrop, *Acoustic phonon anisotropy: phonon focusing*, Comp. Phys. Comm. **28**, 103 (1982).

[85] C. Ell, A. L. Ivanov, and H. Haug, *Relaxation kinetics of a low-density exciton gas in Cu_2O*, Phys. Rev. B **57**, 9663 (1998).

[86] K. E. O'Hara, J. R. Gullingsrud, and J. P. Wolfe, *Auger decay of excitons in Cu_2O*, Phys. Rev. B **60**, 10872 (1999).

[87] N. Naka and N. Nagasawa, *Two-photon tomography of strain-induced potential wells of excitons in Cu_2O*, Phys. Rev. B **70**, 155205 (2004).

[88] H. Stolz and D. Semkat, *Unique signatures for Bose-Einstein condensation in the decay luminescence lineshape of weakly interacting excitons in a potential trap*, Phys. Rev. B **81**, 081302 (2010).

List of publications

1. J. Brandt, P. Felbier, D. Fröhlich, C. Sandfort, M. Bayer, and H. Stolz
Temperature dependence of homogeneous broadening of the 1S-para-exciton in Cu_2O
Physical Review B **81**, 155214 (2010)

2. S. A. Crooker, J. Brandt, C. Sandfort, A. Greilich, D. R. Yakovlev, D. Reuter, A. D. Wieck and M. Bayer
Spin noise of electrons and holes in self-assembled quantum dots
Physical Review Letters **104**, 036601 (2010)

3. C. Sandfort, J. Brandt, D. Fröhlich, M. Bayer, H. Stolz, and G. Baldassarri Höger v. Högersthal
Resonant stimulated Brillouin scattering of orthoexcitons in Cu_2O
Physical Review B **80**, 245201 (2009)

4. J. Brandt, C. Sandfort, D. Fröhlich, M. Bayer, and H. Stolz
Paraexciton polariton propagation beats in cuprous oxide
physica status solidi (c) **6**, 556 (2009)

5. C. Sandfort, J. Brandt, D. Fröhlich, M. Bayer, and H. Stolz
Resonant phonon scattering of paraexcitons in Cu_2O
Physical Review B **78**, 045201 (2008)

6. J. Brandt, D. Fröhlich, C. Sandfort, M. Bayer, H. Stolz, and N. Naka
Ultranarrow optical absorption and two-phonon excitation spectroscopy of Cu_2O paraexcitons in a high magnetic field
Physical Review Letters **99**, 217403 (2007)

7. D. Fröhlich, J. Brandt, C. Sandfort, M. Bayer, and H. Stolz
High resolution spectroscopy of excitons in Cu_2O
physica status solidi (b) **243**, 2367 (2006)

Index

S

T

V

W

Z